

Computer Simulation of Steady State and Transient Performance for Permanent Magnet DC Motors

by
Mitchell Wing

Dissertation submitted to the Department of Electrical and Electronic Engineering, University of Cape Town, in fulfillment of the requirements for the degree of Master of Science in Engineering.

Cape Town, September 1992

The University of Cape Town
The right of Mitchell Wing to have his name printed on this dissertation is hereby acknowledged.
© Mitchell Wing 1992

The copyright of this thesis vests in the author. No quotation from it or information derived from it is to be published without full acknowledgement of the source. The thesis is to be used for private study or non-commercial research purposes only.

Published by the University of Cape Town (UCT) in terms of the non-exclusive license granted to UCT by the author.

Declaration

I declare that this dissertation is my own unaided work. It is being submitted for the degree of Master of Science in Engineering at the University of Cape Town. It has not been submitted before for any degree or examination at this or any other university.

M. Wing

Signed by candidate

24 September 1992.

Acknowledgments

My sincere thanks to my supervisor, Prof. Jacek F. Gieras, for his advice and guidance throughout the last two years and without whom this work would not have been possible.

My gratitude also to Philip Titus, Paul Daniels and Dave Kenyon for their practical assistance.

Many thanks to the Foundation of Research and Development (FRD) for their financial assistance to the project and the bursary.

Synopsis

Permanent magnet motors have outstanding performance for applications such as industrial robots, computer peripherals and automobiles. Since these motors are being used in a growing number of applications, the techniques used to model them are becoming more important in an attempt to obtain the best possible performance from any new design.

The objective of this thesis is to develop an understanding of the classical and the finite element theory in an attempt to obtain the full characteristics of small commutator permanent magnet direct current motors. A comparison of the two methods is done in an attempt to obtain the most effective method of designing new motors. The comparison is done by calculating the performance of two segmental magnet dc motors using the two methods. The methods are investigated separately to ensure that the best possible results are obtained from the simulations. The comparison of the steady state and transient characteristics of the motors are done separately.

The steady state results show that the classical simulation and the finite element simulations compare favourably with the experimental data. In the case of the 8 W motor the finite element method showed an improvement over the classical method since the motor has few rotor slots, 8 slots, and this affects the accuracy of the one dimensional classical simulation.

The optimization of the finite element model meant investigating all aspects of the model. The method of calculating torque was analyzed and it was found that the co-energy finite difference method was the worse method to use and that the Maxwell stress tensor area integral method the most efficient and easiest method to implement, and is as accurate as the co-energy exact derivative method. It was also found that the most efficient number of elements to use in a finite element model is around 1000 elements.

The thickness of the stator yoke has to be increased to take into account the effective stator yoke flux path area of the motor, which in a two dimensional finite element model is not taken into account. It was found that the stator thickness has a great effect on the performance of the motor and thus the effective stator yoke thickness chosen was crucial.

A calculation of the effective stator yoke flux path area was used in obtaining the increase in stator thickness and gave good results in the final models.

The transient simulation using the classical method was done using Laplace and state space solutions. The results show that the state space solution is more accurate since it takes into account the non-linearity of the differential transient equations. The state space solution also had the simpler computation algorithms although the full transient simulation had to be calculated, where as the Laplace simulation could calculate the transient response at any point in time without have to calculate the previous time steps of the transient.

The finite element method showed that it is a very time consuming method in calculating transient performance of motors. The induced eddy current losses in the rotor core, due to the transient armature currents, were ignored in an attempt to make the finite element transient simulation a quicker computational problem. The simplified finite element simulation used the state space approximation to calculate the transient characteristics.

The rotational losses are an important percentage of the total losses in small dc motors and thus effect both the classical and finite element simulations greatly. The simulations did however show a good correlation between the experimental data and the simulations.

The state space transient simulation using the classical method gave good results to both start-up and rheostatic braking simulations. It can thus be concluded that the state space method is a better technique to use than the Laplace simulation method. Due to the time constraints on the finite element transient simulation it is concluded that at present the finite element method is not the most appropriate method for doing transient simulations.

The recommendations from this thesis for future development on the subject of permanent magnet dc motor analysis are that the method of calculating the rotational losses should be improved and that the integration of the classical theory into the finite element simulation package to obtain a faster transient simulation results should be attempted.

The recommendations for South African industry are that the classical simulation program should be incorporated into an expert system for machine designers. The finite element method can then be used to check the magnetic circuit of the designed motor for high magnetic saturation areas.

Contents

Declaration	i
Acknowledgments	ii
Synopsis	iii
Table of Contents	v
List of Figures	ix
List of Tables	xiii
List of Symbols	xiv
1 Introduction	1
1.1 Permanent magnet motors	1
1.2 Purpose	2
1.3 Procedure	3
2 Classical Steady-State Approach	5
2.1 Torque	5
2.2 The Operating Point of a Permanent Magnet	6
2.3 Armature Reaction	9
2.3.1 Cross Armature Reaction	9
2.3.2 Direct-Axis Armature Reaction	10
2.3.3 Commutation Armature Reaction	10
2.4 Slot Leakage Inductance	11
2.4.1 The Slot Leakage Permeance	11
2.4.2 Leakage Permeance of End Connections	12

2.5	Losses	12
2.5.1	Copper Losses	13
2.5.2	Brush-Drop Losses	13
2.5.3	Rotational Losses	13
2.5.4	Armature Core Losses	14
3	Finite Element Steady-State Approach	15
3.1	Electromagnetic Field Equations	15
3.2	Energy Functional	16
3.3	Finite Element Analysis	18
3.4	Modelling of the Permanent Magnets	19
3.5	Torque Calculations	21
3.5.1	Maxwell Stress Tensor Method	21
3.5.2	Co-Energy Method	24
4	Transient Performance	27
4.1	Classical Approach	27
4.1.1	Laplace Solution	29
4.1.2	State Space Solution	31
4.2	Finite Element Approach	32
4.2.1	Simpler Finite Element Solution	35
5	Physical Models and Data Acquisition System	36
5.1	Description of Motors	36
5.2	Data Acquisition System	38
5.3	Calculating Performance on the basis of measurements	39
5.4	Experimental Data	41
6	Steady State Comparison	43
6.1	Classical Simulation	43
6.2	Finite Element Simulation	44
6.2.1	Finite Element Models	44
6.2.2	Torque Calculation	46
6.3	Comparison of Results	49
6.4	Optimization of the Finite element models	54
6.4.1	Accuracy of the torque calculation methods	55

6.4.2	Thickness of the Stator Yoke	58
6.4.3	Simulation of Permanent Magnet	60
6.4.4	The Final Models	61
6.5	Core Losses in the finite element simulation	64
7	Transient Results	66
7.1	Classical Simulation	66
7.1.1	Laplace Solution	66
7.1.2	State Space Solution	67
7.2	Finite Element Simulation	69
7.2.1	Transient finite element simulation	71
7.3	Results	71
8	Special Topics	81
8.1	Cogging Torque	81
8.2	Overlap angle of permanent magnet	81
8.3	Unsymmetrical permanent magnet positioning	85
8.3.1	Magnetomotive force	86
8.3.2	Asymmetry of magnetic circuit and performance characteristics	87
8.3.3	Force distribution	87
9	Conclusions	92
9.1	Steady State	92
9.1.1	Classical simulation	92
9.1.2	Finite element simulation	92
9.2	Transient	93
9.2.1	Classical simulation	93
9.2.2	Finite element simulation	94
9.3	Special topics	94
10	Recommendations	96
10.1	Future development in this field	96
10.2	The relevance to South African Industry	96
	Bibliography	101
A	Co-energy exact derivative derivation	102

CONTENTS

viii

A.1 Triangular Elements	104
A.2 Bilinear Quadratic Elements	106
B Magnetization curves used in simulations	108
C Schematic circuit diagram	111
D Fast Fourier analysis of torque measurement	113

University of Cape Town

List of Figures

2.1	Equivalent magnetic circuit per pole pair of a permanent magnet motor . . .	7
2.2	Operating point of permanent magnet on demagnetization curve	8
2.3	Graph of transient characteristics showing the cross armature reaction . . .	10
2.4	The general shape of a rotor slot	12
3.1	Geometric model of permanent magnet with current sheet attached	21
3.2	Line integration path	23
3.3	Virtual shift of elements: (a) Completely shifted (b) partially shifted . . .	25
5.1	Layout of Test rig with data acquisition system and link to computer . . .	38
5.2	Test Rig for 8 W motors steady state performance	40
5.3	Test Rig for 370 W motor used for steady state and transient performance tests	40
5.4	Un-scaled output from data acquisition system	42
6.1	Flow Chart showing the logical flow of the Steady State Computer Simulation	45
6.2	Cross sections of magnetic circuits of: (a) 370-W motor, (b) 8-W motor . .	46
6.3	Flow Chart showing the Logical calculation of the Airgap path	47
6.4	Meshed Area of finite element model showing Elements making up the Airgap area	48
6.5	Input armature current versus output rotor torque for 370 W motor	50
6.6	Rotor speed versus output rotor torque for 370 W motor	50
6.7	Output power versus output rotor torque for 370 W motor	51
6.8	Motor efficiency versus output rotor torque for 370 W motor	51
6.9	Input armature current versus output rotor torque for 8 W motor	52
6.10	Rotor speed versus output rotor torque for 8 W motor	52
6.11	Output power versus output rotor torque for 8 W motor	53
6.12	Motor efficiency versus output rotor torque for 8 W motor	53

6.13	Electromagnetic Torque versus the increase in the number of elements used in the model for the 370W motor with 3 A armature current	56
6.14	Electromagnetic Torque versus the increase in the number of elements used in the model for the 8W motor with 0.8 A armature current	57
6.15	Electromagnetic Torque versus the increase in the number of elements used in the model for the 8W motor with 1.6 A armature current	57
6.16	Torque versus increase in stator thickness for the 370W motor	59
6.17	Torque versus increase in stator thickness for the 8W motor	59
6.18	Side view through a motor to show the equivalent stator thickness used in the finite element simulation	60
6.19	Models of the two types of permanent magnet equivalents used in finite element simulations: (a) sheet current equivalent (b) material definition in program	61
6.20	Comparison of torque calculations for the two types of permanent magnet models over a full range of loads for the 370W motor	62
6.21	Element layout for 370 W motor. The model uses 1300 elements	63
6.22	Element layout for 8 W motor. The model uses 1150 elements	63
6.23	Flux plots used in the calculation of torque for 370 W motor. (a), (b) have armature current of 0.5 A, and (c) and (d) a armature current of 3 A. (a),(c) have $\theta = 0^\circ$ and (b),(d) have $\theta = 9^\circ$	64
6.24	Flux plots used in the calculation of torque for 8 W motor. (a), (b) have armature current of 0.1 A, and (c) and (d) a armature current of 0.8 A. (a),(c) have $\theta = 0^\circ$ and (b),(d) have $\theta = 20^\circ$	65
6.25	Core loss versus rotor position for 370 W motor	65
7.1	Start-up simulation using the extreme values for the machine constant k	67
7.2	Flow chart showing the logical flow of the Laplace transient simulation	68
7.3	Flow chart showing the logical flow of the state space transient simulation	70
7.4	Flux plots for start-up simulation in the 370 W motor with a load connected. (a) 0 time step after setting up the permanent magnet. (b) 0.5 milliseconds after begin of start-up simulation. (c) 3.5 milliseconds and (d) 0.6 seconds after start of simulation (steady state is reached)	72
7.5	Input armature current versus time in start-up characteristic with 90 V input voltage and no load torque	74

7.6	Rotor speed versus time in start-up characteristic with 90 V input voltage and no load torque	74
7.7	Input armature current versus time in start-up characteristic with 180 V input voltage and no load torque	75
7.8	Rotor speed versus time in start-up characteristic with 180 V input voltage and no load torque	75
7.9	Input armature current versus time in start-up characteristic with 180 V input voltage and 0.665 Nm of load torque	76
7.10	Rotor speed versus time in start-up characteristic with 180 V input voltage and 0.665 Nm of load torque	76
7.11	Input armature current versus time in start-up characteristic with 180 V input voltage and 1.164 Nm of load torque	77
7.12	Rotor speed versus time in start-up characteristic with 180 V input voltage and 1.164 Nm of load torque	77
7.13	Input armature current versus time in rheostatic braking characteristic with 90 V input voltage and no load torque	78
7.14	Rotor speed versus time in rheostatic braking characteristic with 90 V input voltage and no load torque	78
7.15	Input armature current versus time in rheostatic braking characteristic with 180 V input voltage and no load torque	79
7.16	Rotor speed versus time in rheostatic braking characteristic with 180 V input voltage and no load torque	79
7.17	Input armature current versus time in rheostatic braking characteristic with 180 V input voltage and 0.56 Nm of load torque	80
7.18	Rotor speed versus time in rheostatic braking characteristic with 180 V input voltage and 0.56 Nm of load torque	80
8.1	Cross section of a dc commutator motor showing the rotor angle θ and the overlap angle β	82
8.2	Cogging Torque versus rotor angle θ for different loads in the 370 W motor	82
8.3	Cogging Torque versus rotor angle θ for different loads in the 8 W motor	83
8.4	Cogging Torque versus rotor angle θ for four different overlap angles β , at a constant output torque of 2 Nm, in the 370 W motor	84
8.5	Cogging Torque versus rotor angle θ for four different overlap angles β , at a constant output torque of 0.027 Nm, in the 8 W motor	84

8.6	Rotor speed and Efficiency versus overlap angle β , at a constant output torque of 2 Nm, in the 370 W motor	85
8.7	Rotor speed and Efficiency versus overlap angle β , at a constant output torque of 0.027 Nm, in the 8 W motor	86
8.8	Cross section of a dc commutator motor showing overlap angle of the permanent magnet β and permanent magnet shift angle α	87
8.9	Flux plots and resultant MMF distributions for two different directions of rotor rotation with one magnet shifted 10.5°	88
8.10	Armature current and efficiency versus output torque for three different values of magnet shift α , when the rotor rotates in the opposite direction to the magnet shift.	89
8.11	Rotor speed and Output power versus Output torque for three different values of magnet shift, when the rotor rotates in the opposite direction to the magnet shift α	90
8.12	Normal force between the rotor and the magnets versus rotor angle for a symmetrical magnetic circuit and for a magnet shift of 10.5°	91
B.1	Flux density versus field intensity curve for the rotor core	108
B.2	Flux density versus field intensity curve for the stator yoke	109
B.3	Specific rotational losses per unit mass W/kg at 50 Hz versus flux density .	109
B.4	Demagnetization curve of Barium ferrite used in calculating magnets operating point	110
C.1	Printed circuit board of current sensing	111
C.2	Schematic circuit diagram of current sensing with protective voltage isolation for the computer	112
D.1	Unscaled torque signal logged by computer	113
D.2	Fast fourier transform of torque signal	114
D.3	Fourier analysis of harmonics from the 8th to the 21st	114
D.4	Smoothed out torque signal with the low frequency vibrations removed . .	114

List of Tables

5.1	Design data of tested motors	37
6.1	Comparison of Rotational Losses measured and calculated for the 370 W and 8 W dc motors	54
6.2	Processing times for different torque calculation methods	58
6.3	Increase in stator thickness used in models	61
7.1	Armature winding inductance results for 370 W motor	71
8.1	Attraction force of asymmetrical magnetic circuit in 370 W motor with 3 A of load current	90
A.1	Shape functions	102

List of Symbols

Symbols		\vec{E}	Electric field intensity
a	Number of current path pairs on the armature	E_r	Electromotive force of motor (EMF)
A	Armature electric loading in armature reaction	F	Magnetomotive force (MMF)
\vec{A}	Magnetic vector potential	F	Energy functional in finite element method
A_i	Magnetic vector potential at i th node	F_a	Armature magnetizing force
\vec{B}	Magnetic flux density	F_{aq}	Cross armature reaction magnetizing force
B_m	Magnetic flux density of the permanent magnet	F_{ad}	Direct-axis armature reaction
B_r	Remanent magnetic flux density of permanent magnet	F_{ak}	Commutation armature reaction
B_u	Useful magnetic flux density in air-gap	\vec{H}	Magnetic field intensity
$C1, C2$	Constants used in Laplace simulation	H_a	Magnetic field intensity of armature reaction
D	Jacobian matrix in finite element method	H_c	Coercive force of permanent magnet
$ D $	Determinate Jacobian matrix D in finite element method	H_m	Magnetic field intensity of permanent magnet
D_{2out}	Outer diameter of armature core	h_m	Height of permanent magnet
D_{2in}	Inner diameter of armature core	I_a	Armature current
D_{1out}	Outer diameter of stator yoke	$I_{a(i)}$	State of armature current in transient simulation
D_{1in}	Inner diameter of stator	J	Moment of inertia of rotor and load inertia
DK	Stator yoke thickness	\vec{J}	Current density

k	Machine constant including Φ_g	λ_g	Airgap permeance in magnetic circuit of motor
L	Inductance of the armature windings	λ_l	Leakage permeance in magnetic circuit of motor
L_s	Slot leakage inductance	λ_t	Total permeance in magnetic circuit of motor
LA	Length of rotor core	λ_x	Leakage permeance in slots, $x = \text{slot} + \text{end connections}$
LM	Length of permanent magnet	μ	Magnetic permeability
\vec{M}	Remanent magnetization of permanent magnets	σ	Conductivity
N	Number of armature conductors	ω_r	Rotor rotational speed
N_c	Number of conductors per slot	$\omega_{r(i)}$	State of rotor speed in transient simulation
p	Number of pole pairs		
P_{com}	Brush drop losses		
P_{cu}	Copper losses		
P_{fe}	Armature core losses		
P_{rot}	Rotational losses		
R_a	Armature winding resistance		
S_m	Cross sectional area of permanent magnet		
\vec{T}	Torque		
\vec{T}_e	Electromagnetic torque		
V_{br}	Voltage drop of brushes in commutation		
W'	Magnetic co-energy		
Φ_g	Airgap magnetic flux per pole		
Φ_l	Leakage magnetic flux per pole		
Φ_t	Total magnetic flux per pole		
ϵ	Electric permittivity		

Abbreviations

DC,dc	Direct current
EMF	Electromotive force
FE	Finite element
MMF	Magnetomotive force
PM	Permanent magnet
SUB	Sealed universal block loadcell

Chapter 1

Introduction

The number of applications for permanent magnet motors has grown constantly since the early 1970's. The improvements made in the production of permanent magnets and the invention of rare-earth permanent magnets have made permanent magnet motors a highly efficient and popular type of motor. Permanent magnet motors have outstanding performance for applications such as industrial robots, computer peripherals, such as computer printers, in automobiles and even household appliances. Since these machines are manufactured in many different shapes and in large quantities, the techniques used to model these motors is becoming more important in an attempt to obtain the best possible performance and design new permanent magnet motors. Powerful computer software is thus needed in designing a large variety of motor sizes and shapes without compromising performance.

1.1 Permanent magnet motors

The many different types of permanent magnet dc motors can be classified according to their field systems, armature structure and arrangement of brushes and commutators.

The permanent magnet dc commutator motors can be divided up into slotted, slotless and moving coil motors. The slotted dc commutator motor is the most conventional motor, and its high efficiency and performance characteristics make it suitable as a servomotor. The commutator brushes are their only drawback which are subject to wear and maintenance. Brushless motors have thus become popular, with the improvements made in solid-state switches over the past few years and their maintenance free operation.

All of these motors use three types of permanent magnets, two motors of the same

type can thus have different permanent magnets. The three main magnet types are Alnico magnets, Ferrite magnets and Rare earth magnets. The three types of magnets differ in their magnetic properties and thus are used, generally, in different applications. The Alnico magnets have a high magnetic flux density but a low coercive force so they are easily demagnetized and are thus used in applications where it is convenient to magnetize the magnets lengthwise. Ferrite magnets have a low magnetic flux density but a high coercive force and are thus used in applications where a high magnetic flux density is not necessary or where a small airgap is being used. Ferrite magnets are not easily demagnetized, and their material and production costs are low. Rare earth magnets have a high magnetic remanence and a high coercive force giving them a high energy product and thus a high efficiency to their applications. Rare earth magnets are however expensive and were initially only used in aircraft and by the military, but in recent years are gradually being used more in industry.

1.2 Purpose

Although there is a wealth of literature dealing with permanent magnet dc motors, uncertainties and doubts still exist. Amongst others, whether the finite element method is superior to the classical method in calculating the steady state and transient performance characteristics. This has to be considered not only from the point of view of the final accuracy of the results, but also from the convenience and speed at which the results were obtained.

The objective of this thesis is to develop an understanding of the classical theory and the finite element theory in an attempt to obtain the full characteristics of small permanent magnet dc motors. A comparison of the results from the different methods and the amount of work needed to obtain the results will outline the advantages and disadvantages of the two methods.

Before a comparison between the different methods can be done, the optimization of the accuracy of the methods is necessary. This means obtaining the best possible model of the motor using the classical method as well as the finite element method. To this end, an investigation into the finite element models is proposed to ensure that a reasonable number of elements are used to maintain accurate results, ensure that the actual dimensions of the model are simulated and that the effects of using two dimensional models is properly accounted for, and to ensure that the most appropriate method of calculating torque is used. The different methods of calculating the transient characteristics, in the

classical and finite element models are also analyzed.

1.3 Procedure

The classical simulation is based on circuit machine theory, including the development of the operating point of the permanent magnet, and the calculation of the armature reaction and its effect on the operating point. The writing of a computer program is proposed to calculate the performance, due to the lengthy calculations in the classical method and due to the non-linearity in estimating the operating point of the permanent magnet.

The finite element simulation is based on a commercial finite element package. The torque calculation method is investigated using the results of the finite element simulation and a set of short computer programs are proposed for this need. The theory behind the finite element method, as well as the different torque calculation methods is briefly documented.

The theory behind the transient simulations, classical and finite element methods, is described. The different methods of obtaining transient results is analyzed and the results are compared.

The results from the classical simulation and the finite element simulation are compared against experimental data, for which a data acquisition system was build. The steady state and transient results are compared against this experimental data.

Variations in the motors design is considered in an attempt to find the machine parameters that would be crucial to the motors success. This has been done by firstly investigating the cogging torque of the motor, which is of great interest in control systems where the motors are needed to run at low speeds. The quantity of permanent magnet material used in the motor is also investigated and the asymmetry of the magnetic circuit created when the magnets are not perfectly positioned during manufacture, is also investigated.

Conclusions are drawn as to the success of the simulations and to the best use of each of the methods in machine design. Conclusions are also drawn to the limitations of the classical method and finite element method in calculating the steady state and transient performance of small permanent magnet dc motors.

Recommendations are made towards future research in this field where necessary. Recommendations are also made to the relevance of this study to the South African industry, since there is no manufacture of permanent magnet motors in South Africa.

The possibility of machine designers in South Africa needing appropriate design tools to design permanent magnet motors in the future is of great relevance.

University of Cape Town

Chapter 2

Steady-State Performance: Classical Approach

2.1 Torque

Calculating the steady-state performance of a permanent magnet (PM) dc commutator motor differs from field wound dc motors due to the fact that the airgap magnetic flux per pole Φ_g is not simply calculated, as is the case with field wound dc motors. The importance of obtaining the airgap flux in calculating the performance of a PM dc motor can be seen from Ampere's experimental results ($d\vec{F} = I_a d\vec{l} \times \vec{B}$), the torque on a current loop is then

$$\vec{T} = I_a \int \int d\vec{S} \times \vec{B} \quad (2.1)$$

where $d\vec{S}$ is the vector area. Eqn (2.1) leads to the scalar formula for torque

$$T_e = \frac{pN}{2\pi a} I_a \Phi_g \quad (2.2)$$

which is the electromagnetic torque of a dc motor in which p is the number of pole pairs, N is the number of armature conductors, a is the number of current path pairs on the armature and I_a is the armature current.

The steady state performance is accomplished using the assumption that the brush voltage drop (V_{br}) is assumed to be constant and thus independent of armature current. The energy conversion process between the electrical and mechanical quantities is assumed to be a pure conversion process so [29]:

$$E_r I_a = T_e \omega_r \quad (2.3)$$

where E_r is the E.M.F of the motor (rotational EMF), I_a is the armature current, T_e is the electromagnetic torque and ω_r is the rotor speed (rad/s).

The total losses of the motor have to be considered when trying to calculate the output power and the output shaft torque. These losses will be discussed in Section 2.5 [17].

Eqn (2.2) illustrates the importance of calculating the airgap magnetic flux in finding the performance characteristics of a PM dc motor. The airgap magnetic flux is calculated using the operating point of the PM, which will be described in the following section. The armature reaction and the leakage inductance are also important quantities in calculating the operating point of a PM and will also be discussed [2]. The power losses of the PM motor are then considered.

2.2 The Operating Point of a Permanent Magnet

Permanent magnets operate on the demagnetization curve of the hysteresis loop, in the upper left-hand quadrant. The demagnetization curve for the majority of hard magnetic materials can be described analytically using a hyperbola equation [11].

$$B = \frac{B_r(H_c - H)}{H_c - aH} \quad (2.4)$$

where

$$a = \frac{1}{n} \sum_{i=1}^n \left(\frac{H_c}{H_i} + \frac{B_r}{B_i} - \frac{H_c B_r}{H_i B_i} \right) \quad (2.5)$$

To calculate the operating point of a PM an equivalent magnetic circuit per pole pair is used (Fig 2.1). The various leakages are lumped into an equivalent flux Φ_l in a path of permeance λ_l . The useful flux Φ_g in the gap permeance and with an armature reaction (M.M.F.) F_a , occupies a parallel path. The "open circuit", M.M.F. F_o acting through a permeance, occupies another parallel path. The total flux Φ_t with total permeance is the summation of the useful and leakage flux. The height of the PM is h_m and its cross sectional area is S_m .

Using the equivalent magnetic circuit, the magnetic flux density of the permanent magnet is [11]

$$B_m = \frac{1}{S_m}(\Phi_g + \Phi_l) = -\lambda_l \frac{h_m}{S_m} \left(H_m - \frac{1}{\sigma_1} H_a \right) \quad (2.6)$$

Where

$$H_a = \frac{F_a}{h_m} \quad (2.7)$$

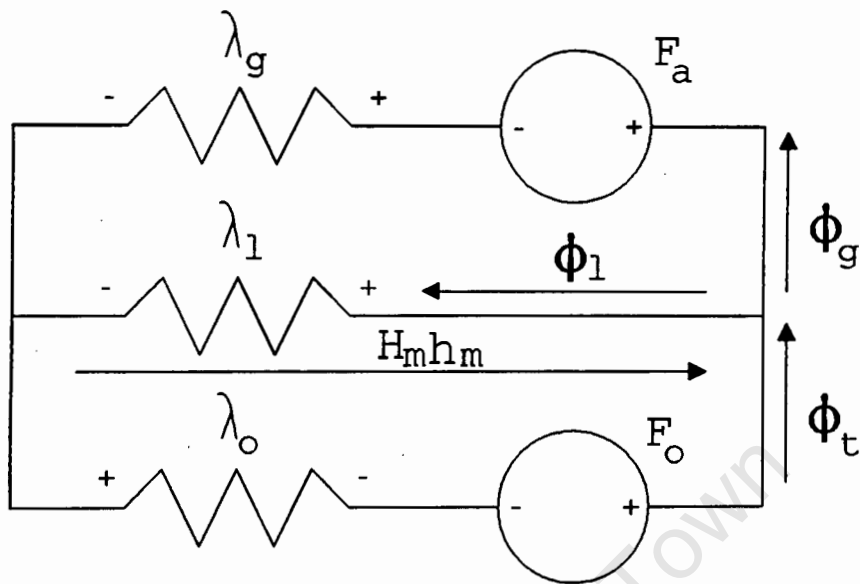


Figure 2.1: Equivalent magnetic circuit per pole pair of a permanent magnet motor is the magnetic field intensity corresponding to M.M.F. of armature reaction. Similarly

$$B_u = \frac{\Phi_g}{S_m} = -\lambda_g \frac{h_m}{S_m} (H_m - H_a) \tag{2.8}$$

is the useful magnetic flux density of the magnet.

From eqns (2.6) and (2.8) straight lines with slopes

$$\tan \alpha_t = \frac{\lambda_t h_m}{S_m} \tag{2.9}$$

$$\tan \alpha = \frac{\lambda_g h_m}{S_m} \tag{2.10}$$

located in the upper left-hand quadrant can be found. The permeances λ_t and λ_g are functions of magnetic permeability which depend on the magnetic field intensity. Thus the lines of B_m and B_u show slight saturation.

The application of a demagnetizing force causes the magnetic flux density within the PM to decrease. The removal of this demagnetization force does not restore the magnetic flux density to its previous position, but moves it along a lower portion of a minor hysteresis loop [21]. This minor hysteresis loop is approximated by a straight line called the recoil line with a slope of $\mu_o \mu_c$, the recoil magnetic permeability. The recoil line has the same slope as the tangent to the demagnetisation curve at B_r (Fig 2.2) [29].

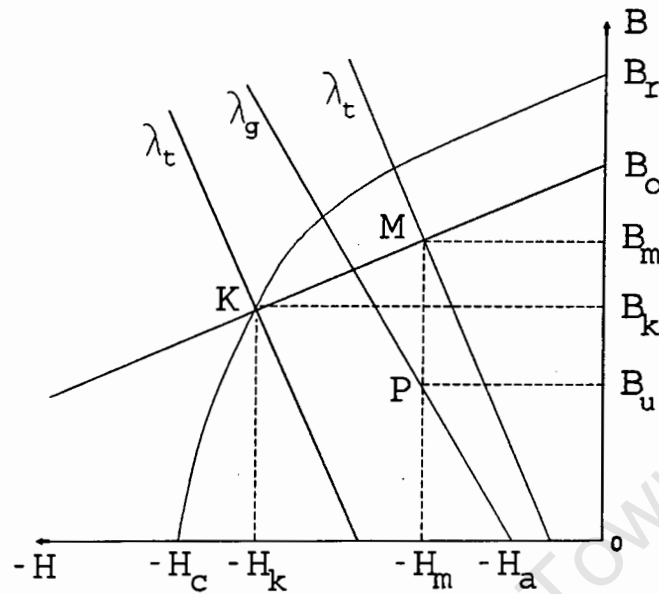


Figure 2.2: Operating point of permanent magnet on demagnetization curve

The point K (Fig 2.2) is taken at the value of maximum armature reaction F_{amax} which takes place during counter-current braking (plugging).

Using eqns (2.4) and (2.7). Finding [11]:

$$H_k = 0.5 \left(A_k + \sqrt{A_k^2 - 4 \left(\frac{H_c H_{amax}}{a \sigma_1} - \frac{B_r H_c}{a \tan \alpha_t} \right)} \right) \quad (2.11)$$

where

$$A_k = \frac{H_c}{a} + \frac{H_{amax}}{\sigma_1} - \frac{B_r}{a \tan \alpha_t} \quad (2.12)$$

Since the recoil line intersects the demagnetisation characteristic curve at point K (Fig 2.2). The equation of the recoil line can be written as :

$$B_m = B_k \mu_o \mu_c (H_m - H_k) \quad (2.13)$$

The operating point M can be found using eqns (2.6) and (2.13) giving:

$$H_m = - \frac{B_k - \mu_o \mu_c H_k - \frac{H_a \tan \alpha_t}{\sigma_1}}{\tan \alpha_t + \mu_o \mu_c} \quad (2.14)$$

The point P corresponding to the useful magnetic flux density is at the intersection of eqn (2.8) with a perpendicular line to the axis OH through the point H_m (Fig 2.2), giving :

$$B_u = \tan \alpha (H_a - H_m) \quad (2.15)$$

The airgap magnetic flux per pole is then

$$\Phi_g = B_u S_m \quad (2.16)$$

2.3 Armature Reaction

The armature reaction i.e. the action of the armature magnetising force on the main magnetising force can be expressed as [21]:

$$F_a = F_{aq} - F_{ad} - F_{ak} \quad (2.17)$$

where F_{aq} is the cross armature reaction, F_{ad} is the direct axis armature reaction and F_{ak} is the commutation armature reaction.

The magnetising force of the armature is calculated using the effective air-gap length, which is found using the unit of armature periphery length, called the armature electric loading.

$$A = \frac{NI_a}{2\pi a D_{2out}} \quad (2.18)$$

where D_{2out} is the outer diameter of the armature core.

The MMF of the armature is necessary in analyzing the armature reaction. The MMF of the cross armature reaction is calculated using a numerical method, which will be discussed next. The calculations of the direct-axis armature reaction and commutation armature reaction are then discussed.

2.3.1 Cross Armature Reaction

Armature current produces an armature cross magnetising force which distorts the main magnetic field, produced by the permanent magnets, when the brushes are on the geometrical neutral line. This armature cross magnetising force weakens the main field under the trailing edge of pole and increases it under the leading edge of the pole, in a motor. Due to saturation in the magnetic circuit, the field components cannot simply be summed to find the resultant field [17].

With reference to the transient characteristic curve (Fig 2.3). The area of rectangle $aCFd$ serves as an indication of the flux (Φ_m) magnitude at no-load. The curvilinear tetragen serves as an indication of the magnitude of flux at a certain load. For a saturated machine, the area ABC is larger than ADF . Thus the machine has an increase in the excitation current, if the terminal voltage is constant and thus the pole magnetising force

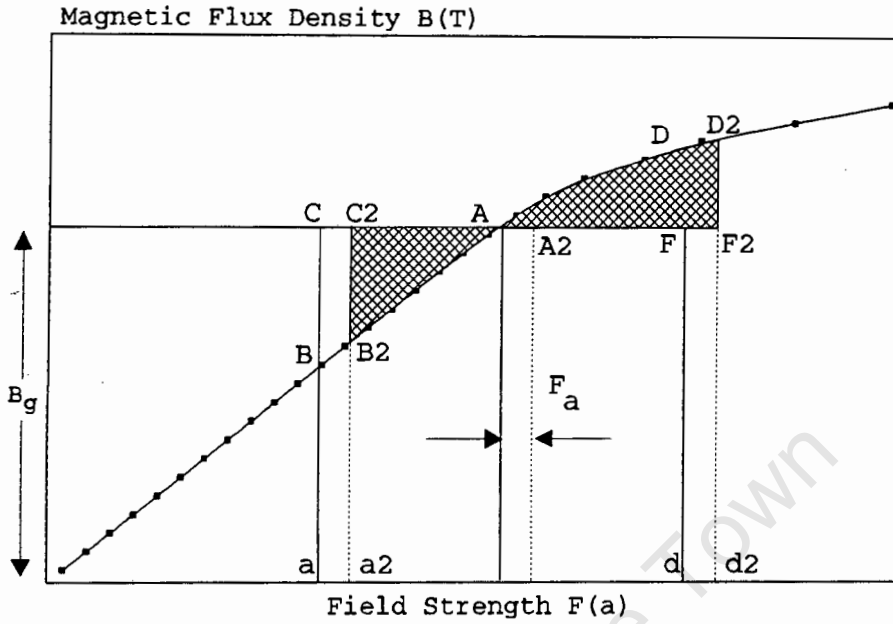


Figure 2.3: Graph of transient characteristics showing the cross armature reaction

must be increased. By increasing the magnetising force by AA_2 , the areas B_2C_2A and AD_2F_2 are equal. The cross armature reaction per pole is then given by AA_2 , called F_a .

2.3.2 Direct-Axis Armature Reaction

When the brushes of a motor are shifted in the opposite direction to direction of motion. An axis armature reaction of a magnetising nature is found.

The direct-axis armature reaction can then be expressed as :

$$F_{ad} = 2Ab_{br} \tag{2.19}$$

where b_{br} is the distance the brush is shifted and A is the armature electric loading. For small DC motors the brush shift $b_{br} = (0.15..0.3) * 10^{-3}m$ [11].

2.3.3 Commutation Armature Reaction

The commutation reaction of an armature is the action of the magnetising force induced by the currents of the coil sections being commutated on the main flux of a machine.

The commutation armature reaction can be approximated using the following expres-

sion [11].

$$F_{ak} = \frac{b_k N^2 L_a n}{k \sum R_k} \lambda'_k A \quad (2.20)$$

Where $b_k = 0.8\tau(1 - \alpha)$ is the width of the commutation zone, k is the number of the commutator segments, $\sum R_k$ is the resistance of the short circuited coils section plus contact resistances of the leading and trailing edges of brushes. λ'_k is the leakage permanence of a short-circuited coil section during its commutation, n is the speed in rev/s and L_a is the length of the armature core.

2.4 Slot Leakage Inductance

PM dc motors have winding slots and thus the leakage inductance of the slots has to be considered. Leakage fields encounter mainly air-gap reluctances. The reluctances of the steel parts may therefore be disregarded for practical purposes and it is therefore considered that the leakage inductance be constant.

When considering the full number of conductors N_c in a slot, the expression for the leakage inductance is [17]:

$$L_s = \mu_0 N_c^2 \sum \lambda_x l_x \quad (2.21)$$

The total permanence $\sum \lambda_x$ can be divided into the equivalent permanence for slot leakage field, λ_s and the equivalent permanence for the end connections, i.e.

$$\sum \lambda_x l_x = 2l\lambda_s + 2l_{end}\lambda_{end} \quad (2.22)$$

where l is the length of the conductor located in the slot and l_{end} is the length of the end connections.

2.4.1 The Slot Leakage Permeance

When calculating the slot leakage permanence the reluctance of the steel may be neglected and it can then be assumed that all magnetic lines cross the gap everywhere as straight and parallel lines. These parallel lines are considered as elementary tubes and the reluctance is considered equal to the width of the slot at a given point. The slot permanence is determined as the ratio of tube width along the slot height to the tube length across the slot width.

The slot leakage permanence varies in accordance to the slot shape [17]. A general slot shape is shown in Fig 2.4 which can be divided into 4 separate areas when calculating the slot leakage permeance.

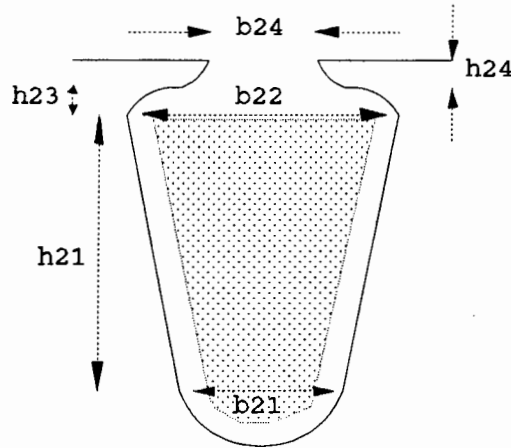


Figure 2.4: The general shape of a rotor slot

So the total slot leakage is [17]:

$$\lambda_s = \frac{1}{2} \left(\frac{r^2}{\text{slot area}} \right)^2 \left(\frac{8\pi^3}{3} + 4\pi + 4 \right) + \frac{2h_{21}}{3(b_{21} + b_{22})} + \frac{2h_{23}}{b_{22} + b_{24}} + \frac{h_{24}}{b_{24}} \quad (2.23)$$

2.4.2 Leakage Permeance of End Connections

The end connection leakage can be calculated with great mathematical difficulty. Since the effect of adjacent coils on each other as well as the effect of the rotor and stator on each other must be considered [19]. The permeance of the end connections varies much less than the resultant permeance of the slot, so certain mean values can be taken. For example Kostenko and Piotrovsky [17] recommends:

- For bands of magnetic materials : $\lambda_{end} = 0.75$
- For bands of non-magnetic materials : $\lambda_{end} = 0.5$

2.5 Losses

The losses of the PM dc commutator motor can be divided into four main types. These are copper losses, brush-drop losses, rotational losses and armature core losses. Any additional losses are considered in stray losses which are assumed to be approximately 1% of the output power [17].

2.5.1 Copper Losses

The copper losses are done to the resistance of the armature windings:

$$P_{cu} = I_a^2 R_a \quad (2.24)$$

2.5.2 Brush-Drop Losses

The brush-drop losses are due to the constant voltage drop across the brushes:

$$P_{com} = V_{br} I_a \quad (2.25)$$

For Carbon-Graphite brushes V_{br} is 2 ± 0.4 volts, independent of armature current.

2.5.3 Rotational Losses

The rotational losses are found using an approximation for the rotational losses at rated speed. The rotor rotational losses are then assumed to have a linear speed relationship, so that the rotational power loss at a specific speed is :

$$P_{rot} = P_{rotr} \left(\frac{n}{n_r} \right) \quad (2.26)$$

where P_{rotr} is the rotational losses at rated speed, n_r is the rated speed and n is the specific speed.

The rotational losses consist of three components, the losses of the bearings, the brush friction losses and the windage losses:

Bearing Losses

The bearing friction losses may be expressed as [17]:

$$P_{bear} = k_f \frac{F_r}{D} V_{jr} \quad (2.27)$$

where F_r is the load on the bearing race in newtons, D is the diameter of a circle drawn through the ball bearing centre (m), V_{jr} is the speed at the journal periphery (m/s) and k_f is the co-efficient of friction for a ball bearing which is between 0.0001 to 0.0002.

Brush Friction Losses

The brush friction losses may be expressed as [17]:

$$P_{fbr} = k_f F_{br} S_{br} v_c \quad (2.28)$$

where k_f is the coefficient of friction of the brushes against the commutation and is between 0.2 and 0.3 for carbon brushes. F_{br} is the specific brush pressure, usually between 15000 and 25000 N/m^2 . S_{br} is the contact area of all the brushes with the commutators (m^2) and v_c is the speed of the commutator in (m/s) at rated speed.

$$v_c = \frac{D_c \omega_r}{2} \quad (2.29)$$

where D_c is the diameter of the commutator.

Windage Losses

Due to the necessity to improve the ventilation and increase the coefficient of heat dissipation of machines most motors have built-in fans, which increase the windage losses and make it necessary to consider these losses.

$$P_w = 2D_2^3 n^3 l_o \times 10^{-8} \quad (2.30)$$

where n is the rotor speed (rpm), l_o is the effective length of the armature (m) and D_2 is the armature diameter (m).

2.5.4 Armature Core Losses

The armature core losses are limited to the total losses within the steel of the armature. The expression for armature core losses is [17]:

$$P_{fe} = P_{\frac{1}{50}} \left(\frac{f}{50}\right)^\beta B^2 G_s \quad (2.31)$$

where P is the specific losses at 50 Hz, f is the frequency of magnetic reversal, β is the exponent averaging between 1.2 and 1.3, B is the flux density and G_s is the mass of the rotor.

Chapter 3

Steady-State Performance: Finite Element Approach

3.1 Electromagnetic Field Equations

Electromagnetic fields are described in terms of the electric field vector \vec{E} and the magnetic field vector \vec{H} . The relationship between these two vectors is set out in Maxwell equations [18].

$$\nabla \times \vec{E} = -\frac{\partial \vec{B}}{\partial t} \quad (3.1)$$

$$\nabla \times \vec{H} = \vec{J} + \frac{\partial \vec{D}}{\partial t} \quad (3.2)$$

$$\nabla \cdot \vec{D} = \rho \quad (3.3)$$

$$\nabla \cdot \vec{B} = 0 \quad (3.4)$$

where: \vec{E} - electric field intensity, $\vec{J} = \sigma \vec{E}$ - current density, σ - electric conductivity, \vec{H} - magnetic field intensity, $\vec{B} = \mu \vec{H}$ - magnetic field density, μ - magnetic permeability, $\vec{D} = \epsilon \vec{E}$ - electric field density and ϵ - electric permittivity. It has been assumed that the medium is isotropic.

Maxwell magnetic divergence equation is satisfied if the divergence of the curl of any twice differentiable vector vanishes. The magnetic vector potential is defined as follows:

$$\vec{B} = \nabla \times \vec{A} \quad (3.5)$$

Maxwell electric curl eqn (3.1) may then be written as:

$$\nabla \times \left(\vec{E} + \frac{\partial \vec{A}}{\partial t} \right) = 0 \quad (3.6)$$

then

$$\vec{E} = -\frac{\partial \vec{A}}{\partial t} - \nabla V \quad (3.7)$$

since \vec{E} differs from the time rate of \vec{A} by some irrotational vector grad V .

The magnetic and electric potentials are written in terms of vector potential (\vec{A}), with a little manipulation of the above mentioned equations forms:

$$\nabla^2 \vec{A} = \nabla(\nabla \cdot \vec{A} + \mu\epsilon \frac{\partial V}{\partial t}) + \mu\epsilon \frac{\partial^2 \vec{A}}{\partial t^2} - \mu \vec{J} \quad (3.8)$$

Since the divergence of \vec{A} has not be specified, the above equation can be simplified by choosing the appropriate value so as to satisfy the Lorentz condition

$$\nabla \cdot \vec{A} = -\mu\epsilon \frac{\partial V}{\partial t} \quad (3.9)$$

and out emerges the inhomogeneous wave equation

$$\nabla^2 \vec{A} - \mu\epsilon \frac{\partial^2 \vec{A}}{\partial t^2} = -\mu \vec{J} \quad (3.10)$$

Boundary conditions are set on a closed surface. The Dirichlet boundary condition is $\vec{A} = f(s)$ and the homogenous Neumann condition is $\frac{\partial \vec{A}}{\partial n} = 0$ where $f(s)$ is a specified function along a boundary and n represents a space coordinate normal to the modelled surface [31].

The assumptions made for further analysis are:

1. The end and edge effects are neglected and no field variations are assumed to occur in the axial direction (z-direction).
2. The permeability of the iron is modelled as a non-linear function of the field strength.
3. Temperature effects on the permeability are ignored.
4. the source function is represented by a current density distribution in the cross-section of ideal conductors.

3.2 Energy Functional

The variational method consists of formulating the partial differential equations of the field problem in terms of a variational expression called the energy functional. The Euler

equation of this functional will yield the original differential equation. The minimization of the energy functional is implemented in the finite element method.

The machine is analyzed on the assumption that it has infinite axial length ($z \rightarrow \infty$). A two dimensional model (x and y axis) is thus used with the added assumption that the slot current is axially-directed, i.e. $\vec{J} = \vec{k}J(x, y)$, and the additional magnetization vector $\vec{M}_o = M_{ox}\vec{i} + M_{oy}\vec{j}$ of the medium, with a resultant axially-directed magnetic vector potential, i.e. $\vec{A} = \vec{k}A(x, y)$ where $\vec{i} = 0, \vec{j} = 0, \vec{k}$ are unit vectors.

The above simplifications allow for the simplification of the general Poisson's equation used for magnetostatic fields in vector potential A from eqn. (3.10). Poisson's equation

$$\nabla \times (\nu \times \nabla \vec{A}) = \vec{J} \quad (3.11)$$

where ν is the reciprocal of the magnetic permeability (μ).

The nonlinear Poisson's equation for z directional current density and magnetic vector potential becomes:

$$\frac{\partial}{\partial x}(\nu(\frac{\partial \vec{A}}{\partial x})) + \frac{\partial}{\partial y}(\nu(\frac{\partial \vec{A}}{\partial y})) = -\vec{J} \quad (3.12)$$

which is subject to the appropriate Dirichlet and homogenous Neumann boundary conditions mentioned earlier.

The field problem can now be written in variational terms as a energy functional as:

$$F = \int \int_R (\int_0^B \vec{H} d\vec{B}) dx dy - \int \int_R \vec{J} \vec{A} dx dy \quad (3.13)$$

where R is the model domain.

In isotropic materials the energy functional can be simplified further depending in the type of ferromagnetic material:

- Hard magnetic materials

$$\vec{B} = \mu_0 \vec{H} + \vec{M} \approx \mu_M \vec{H} + \vec{M}_r \quad (3.14)$$

$$F = \int \int_R (\frac{1}{2\mu_M} B^2 - \frac{1}{\mu_M} \vec{M}_r \vec{B} - \vec{J} \vec{A}) dR \quad (3.15)$$

- Soft magnetic materials

$$\vec{B} = \mu_0 \vec{H} + \vec{M} \quad (3.16)$$

$$F = \int \int_R (\frac{1}{2\mu} B^2 - \vec{J} \vec{A}) dR \quad (3.17)$$

where \vec{M}_r is the remanent magnetization of hard magnetic materials and μ_M is the magnetic permeability. The eqn (3.17) is however just a special case of eqn (3.15) where $\mu_M = \mu$ and $\vec{M}_r = 0$, so the general equation for models including permanent magnet materials is taken as eqn (3.15). The minimization of eqn (3.15) is done by the finite element method which follows.

3.3 Finite Element Analysis

The Finite element analysis method is used with a discretised model of small sub-regions, called elements. The elements are connected at node points and their vertices become the element boundaries. The unknown field variable over each element is approximated by continuous functions expressed in terms of the nodal values of the field variable. The functions defined over each finite element are called interpolation functions or shape functions.

The program used in this simulation has only three and four noded elements. The shape functions are thus only planar or bi-planar functions. The field variable, magnetic vector potential (A), has a value inside each element as:

$$A_k(x, y) \approx \sum_i^n N_i(x, y) A_i \quad (3.18)$$

where $N_i(x, y)$ is the shape function of the i th node, A_i is the magnetic vector potential at the i th node and the index i ranges over the number of element vertices (n).

The energy functional can be written for each element within a model where the total energy functional is the sum of the individual functionals:

$$F = \sum_{e=1}^{N_e} F_e \quad (3.19)$$

where N_e is the total number of elements in the model.

The energy functional for a particular element can then be written using eqn (3.15) and eqn (3.18) as:

$$F_e = \int \int_R \left(\frac{1}{2\mu_M} |\nabla \times (\sum_{i=1}^n N_i A_i \vec{k})|^2 - \frac{1}{\mu_M} \vec{M}_r \cdot \nabla \times (\sum_{i=1}^n n N_i A_i \vec{k}) - j \sum_{i=1}^n n N_i A_i \right) dR \quad (3.20)$$

where \vec{k} is a unit vector.

The variational method is actually the minimization of the energy functional by setting its first derivative with respect to every vertex value \vec{A}_i to zero, so that:

$$\frac{\partial F}{\partial \vec{A}_i} = \sum_{e=1}^{N_e} \frac{\partial F_e}{\partial \vec{A}_i} = 0 \quad (3.21)$$

The solution of the minimization function when using a Cartesian coordinate system per element is:

$$\frac{\partial F_e}{\partial A_i} = \int \int_R \left(\frac{1}{\mu_M} (N'_{ix} \sum_{j=i}^n N'_{jx} A_j + N'_{iy} \sum_{j=1}^n N'_{jy} A_j) - \frac{1}{\mu_M} (M_{rx} N'_{ix} - M_{ry} N'_{iy}) - j N_i \right) dx dy \quad (3.22)$$

where $N'_{ix} = \frac{\partial N_i}{\partial x}$ and $N'_{iy} = \frac{\partial N_i}{\partial y}$ from the shape function.

The minimization of eqn (3.22) is carried out for all the elements of the field region and can be expressed in matrix form in which the unknown vector potential is determined

$$[S] \cdot [A] = [J] \quad (3.23)$$

where J is called the forcing vector and S is the stiffness matrix which is nonlinear, symmetric, sparse and band structured.

The matrix S is nonlinear since it depends not only on the shape and the size of the elements but also on the reluctivities, which depend on A . The problem is thus a nonlinear algebraic one which is solved using the Newton-Raphson method [30]:

$$A^{k+1} = A^k - \left[\frac{\partial}{\partial A_k} S^k A^k \right]^{-1} (S^k A^k - J) \quad (3.24)$$

3.4 Modelling of the Permanent Magnets

Permanent magnets can be modelled using either a finite element function or using a sheet current.

When the permanent magnet function is used the functional of the finite element program has to include the remanent magnetization (M_r) as shown in eqn (3.15). The remanent magnetization of the permanent magnet is equal to the remanent induction of the magnet (B_r) as shown in Fig 2.2.

Simulating the permanent magnet using a sheet current has the advantage that it allows for a general demagnetization curve relation to be used and no special adaptations to the finite element program have to be made. The radial magnetization can also easily be implemented since the magnet does not have to be divided into a number of smaller

magnetics with varying magnetization directions, as is the case when using the permanent magnet function.

The demagnetization curve of the PM is assumed to be single valued.

$$H = \nu(B)B - H_c \quad (3.25)$$

where ν is the isotropic nonlinear function of B and H_c is the coercive force. Substituting eqn. (3.25) into Ampere's law

$$\nabla \times [\nu(B)B - H_c] = \vec{J} \quad (3.26)$$

The PM can thus be modeled as an electromagnet having reluctivity $\nu(B)$ and a current density $J_{pm} = \nabla \times H_c$. The non-linear reluctivity $\nu(B)$ can be calculated as:

$$\nu(B) = \frac{H + H_c}{B} \quad (3.27)$$

which means the B-H curve is shifted to the origin when calculating ν .

In 2-D models the PM's are assumed to be infinitely long in the z direction and uniformly magnetized in the $x - y$ plane.

Considering a magnet magnetized in the y direction then $H_c = H_c \cdot \vec{u}_y$ so $J_{pm} = -\vec{u}_z \frac{\partial H_c}{\partial x}$. H_c is a step function that is zero outside the magnet and H_{cpm} inside the magnet [10].

$$J_{pm} = \frac{\Delta H_c}{\Delta x} = \frac{H_{cpm}}{\Delta x} \quad (3.28)$$

where Δx is small but not infinitesimal (Fig 3.1).

$$I = J_{pm} l_{pm} (\Delta x) = H_{cpm} l_{pm} \quad (3.29)$$

which is a sheet current along both sides of the magnet. When considering an arc section radially magnetized a similar result is found (Fig 3.1):

$$J_{pm} = \frac{1}{r} \frac{\Delta H_c}{\Delta \theta} \quad (3.30)$$

$$I = \int_{r_1}^{r_2} \int_{\theta}^{\theta+\Delta\theta} J_{pm}(r) r dr d\theta = H_{cpm} (r_2 - r_1) \quad (3.31)$$

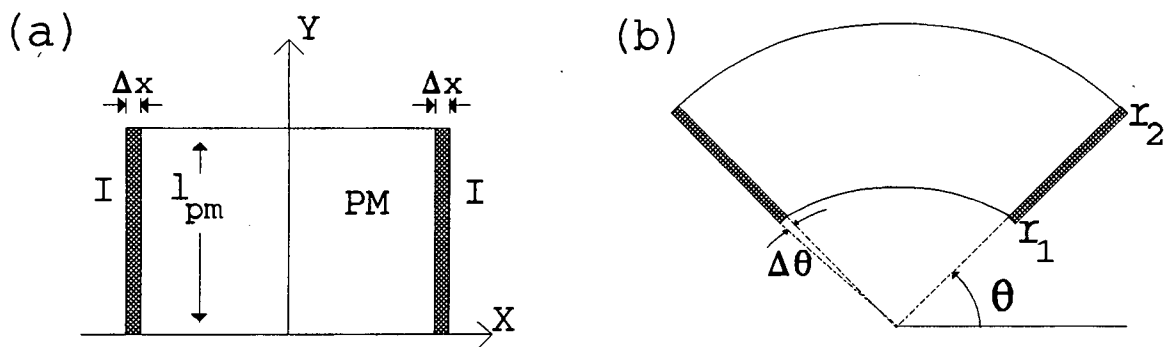


Figure 3.1: Geometric model of permanent magnet with current sheet attached

3.5 Torque Calculations

The calculation of torque using the finite element method is one of the most important functions of this method. There are three main methods of calculating torque of which Maxwell Stress Tensor Method and the Co-Energy Method are the most popular and Ampere's experimental method a less popular approach. Many authors have favoured one method over an other [9] while other authors have shown the advantages and disadvantages of the different methods [6].

The Maxwell Stress Tensor and Co-Energy Methods are both considered, with improvements made to both methods in an attempt to obtain the most accurate and also convenient method of calculating torque. A comparison is made between the different approaches on their ease of calculating the torque and their accuracy.

3.5.1 Maxwell Stress Tensor Method

The use of the Maxwell Stress Tensor method is due to its simplicity, from a computational perspective, since it requires only the local flux density distribution along a specific contour in the airgap of a machine.

This methods accuracy is markedly dependent on the model discretization and on the selection of the integration contour [22]. The Maxwell Stress Tensor line integration necessitates a precise solution in the airgap, demanding a fine discretization of the model in the airgap since the flux density is not continuous at the nodes and across boundaries of first-order elements. A more accurate solution would be to use several contours within

the airgap and find the average value of torque. This has led to the development of the area integral using the Maxwell Stress Tensor method.

The Maxwell Stress Tensor line integral and Maxwell Stress Tensor area integral methods will be described below and their application within a post processor program will be compared in a later section.

Line Integration

Using the definition of Maxwell's stress tensor, the total electromagnetic torque in the airgap of an electrical machine can be determined by the line integral along a closed path located within the airgap [26]:

$$T = -\frac{2pL_{eff}r^2}{\mu_0} \int_{\theta_1}^{\theta_2} B_r B_\theta d\theta \quad (3.32)$$

where r is the radius of the circumference which lies in the airgap, p is number of pole pairs, L_{eff} is the length of the rotor, B_r and B_θ are the radial and tangential components of the flux density respectively.

Since a finite grid is being used the above equation can be written for element i as:

$$T = -\frac{2pL_{eff}}{\mu_0} \sum_{i=1}^{N_g} r^2 \int_{\theta_i}^{\theta_{i+1}} B_{ri} B_{\theta i} d\theta \quad (3.33)$$

where N_g is the total number of elements along the line integral and r is the radius of the gauss point within the element (Fig 3.2).

Transforming B_{ri} and $B_{\theta i}$ of equ (3.33) into B_{xi} and B_{yi} of an x-y coordinate using $B_{ri} = B_{xi} \cos\theta_i + B_{yi} \sin\theta_i$, $B_{\theta i} = B_{yi} \cos\theta_i + B_{xi} \sin\theta_i$ and integrating we find [26]:

$$T = -\frac{2pL_{eff}}{\mu_0} \sum_{i=1}^{N_g} r^2 \left[\frac{1}{2} (B_{xi}^2 - B_{yi}^2) \sin(\theta_{i+1} + \theta_i) \sin(\theta_{i+1} - \theta_i) \right. \\ \left. - B_{xi} B_{yi} \cos(\theta_{i+1} + \theta_i) \sin(\theta_{i+1} - \theta_i) \right] \quad (3.34)$$

Area Integration

The area integration of Maxwell stress tensor method removes the reliance of the line integration method on the models discretization and on the contour selection within the airgap.

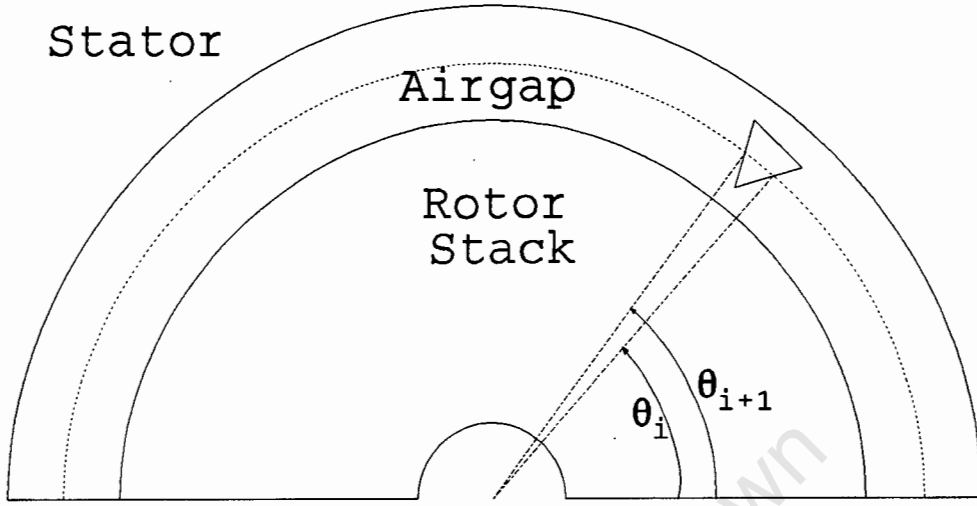


Figure 3.2: Line integration path

Consider an airgap of thickness g being divided radially into k equal intervals [6]. If a line integral is done on every interval the average torque is given by:

$$T_{av} = -\frac{1}{k} 2pL_{eff} \sum_{j=1}^k \left[\frac{1}{\mu_0} \int_{\theta_1}^{\theta_2} r^2 B_r B_\theta d\theta \right]_j \quad (3.35)$$

which can be multiplied and divided by $\Delta g = g/k$ to obtain:

$$T_{av} = -\frac{2pL_{eff}}{g} \sum_{j=1}^k \left[\frac{1}{\mu_0} \int_{\theta_1}^{\theta_2} r^2 B_r B_\theta d\theta \right]_j \Delta g \quad (3.36)$$

As k approaches infinity the limit will give the torque as:

$$T = -\frac{2pL_{eff}}{\mu_0 g} \int_g \int_\theta r^2 B_r B_\theta d\theta dg \quad (3.37)$$

Substituting in $dA = r d\theta dg$ into eqn. (3.37) gives:

$$T = -\frac{2pL_{eff}}{\mu_0 g} \int \int_{area} r_i B_r B_\theta dA \quad (3.38)$$

Since the magnetic flux density is constant within each element. The final equation is:

$$T = -\frac{2pL_{eff}}{\mu_0 g} \sum_{i=1}^{N_g} r_i B_{r_i} B_{\theta_i} A_i \quad (3.39)$$

where N_g is the number of elements within the airgap and A_i is the area of the element i .

3.5.2 Co-Energy Method

The co-energy method is generally recognized as the most accurate method of calculation torque as it includes the whole FE model in its calculation and therefore suppresses the adverse effects of local errors due to coarseness of discretization on the final result [22].

The torque is calculated as the derivative of the magnetic co-energy with respect to angular displacement. This is done by the finite difference approximation or the exact derivative method.

Finite Difference

The finite difference approximation approximates the derivative of co-energy by the change in co-energy at two rotor positions, called the co-energy finite difference method.

$$T = \frac{dW}{d\theta} = \frac{W'_1 - W'_0}{\theta_1 - \theta_0} \quad (3.40)$$

The problem with the finite difference approach is that two finite element models have to be calculated, doubling the calculation time, and the most suitable value of angular increment $\Delta\theta$ is unknown and has to be found using a trial-and-error procedure. If $\Delta\theta$ is too small, rounding-off errors in ΔW will dominate. If $\Delta\theta$ is too large, the calculated torque will no longer be accurate for the specific rotor position.

Exact Derivative

A lot of time could be saved if the co-energy derivative could be obtained directly from one FE solution, instead of from two FE solutions and from determining an appropriate $\Delta\theta$. The "exact derivative" co-energy method uses the virtual-work principle in calculating the electromagnetic torque.

The magnetic co-energy W' is:

$$W' \approx F_{opt} = F(A_{opt}(x, y)) \quad (3.41)$$

and F_{opt} is the result of the minimization of the energy functional i.e. $\frac{\partial F}{\partial A_i} = 0$ and A_{opt} is the vector potential. The electromagnetic torque from the co-energy method is:

$$T = \frac{\partial F_{opt}}{\partial \theta} = \frac{\partial F_{opt}}{\partial \theta} \Big|_{(A_i=const.)} + \frac{\partial F_{opt}}{\partial A_i} \Big|_{(\theta=const.)} \frac{\partial A_i}{\partial \theta} \quad (3.42)$$

where θ is the angular measure of virtual rotation and $\frac{\partial F}{\partial A_i} = 0$ as from the definition of the finite element method, so:

$$T = \frac{\partial F}{\partial \theta} \Big|_{A_i = \text{const.}} = \frac{\partial}{\partial \theta} \int \int_R \left[\int_0^B H dB - \vec{J} \vec{A} \right] dR \quad (3.43)$$

The virtual shift produces 3 different types of movement on the elements (Fig 3.3):

1. The nodes of an element are not moved at all.
2. All the nodes of an element are shifted, resulting in a completely shifted element.
3. Only some of the nodes of an element are shifted, a partially shifted or distorted element.

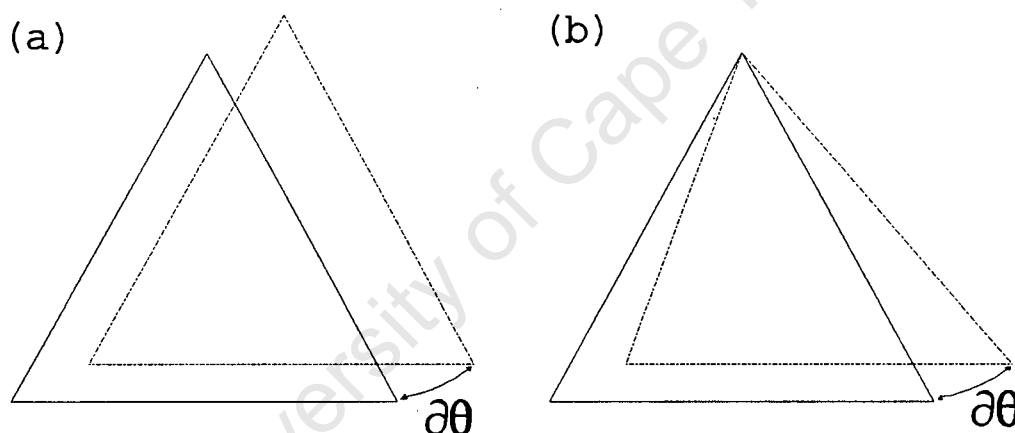


Figure 3.3: Virtual shift of elements: (a) Completely shifted (b) partially shifted

The virtual work principle means there has to be some virtual shift within the model. This virtual movement is done within the airgap of the electrical machine where the physical movement within the real model would take place. Since there is no forcing current ($J = 0$) in the airgap, eqn (3.43) becomes:

$$T = \frac{\partial}{\partial \theta} \int \int_R \int_0^B H dB dR \quad (3.44)$$

The finite element method is discretized into elements and so eqn (3.44) is written for each element separately. Each element is transformed into a isoparametric form using the

isoparametric coordinates (u, v) and thus equ (3.44) becomes:

$$T = \frac{\partial}{\partial \theta} \sum_e \int \int_{\square_e} \int_0^B H dB |D| dudv \quad (3.45)$$

which can be written as:

$$T = \sum_e \int \int_{\square_e} \left[\frac{\partial}{\partial \theta} \left[\int_0^B H dB \right] |D| + \int_0^B H dB \frac{\partial |D|}{\partial \theta} \right] dudv \quad (3.46)$$

where \square_e is the area of the element and $|D|$ is the determinate of the Jacobian matrix D .

$$D = \begin{pmatrix} \partial x / \partial u & \partial y / \partial u \\ \partial x / \partial v & \partial y / \partial v \end{pmatrix} = \begin{pmatrix} \sum_{i=1}^n N'_{iu} x_i & \sum_{i=1}^n N'_{iu} y_i \\ \sum_{i=1}^n N'_{iv} x_i & \sum_{i=1}^n N'_{iv} y_i \end{pmatrix} \quad (3.47)$$

Integrating eqn (3.46) and simplifying to the following form:

$$T = \sum_{\square_e} \left[-\frac{1}{\mu_0} \vec{B}^T G^{-1} \frac{\partial G}{\partial \theta} \vec{B} |D| + \frac{|B|^2}{2\mu_0} \frac{\partial |D|}{\partial \theta} \right] w_i \quad (3.48)$$

where w_i is a weighting function for the different element types [8] and G is:

$$G = \begin{pmatrix} \partial y / \partial u & -\partial x / \partial u \\ \partial y / \partial v & -\partial x / \partial v \end{pmatrix} \quad (3.49)$$

Eqn. (3.48) is simplified for use with three and four node linear elements. The simplification is necessary so that the method can be successfully implemented in a computer program. For a three noded triangular element with node 1 being the movable node then eqn. (3.48) becomes Appendix A:

$$T = \frac{1}{2} \sum_e \sum_i \left[\left[\frac{1}{\mu_0} [B_x^2 x_1 (x_2 - x_3) + B_y^2 y_1 (y_2 - y_3) + B_x B_y (y_1 (x_2 - x_3) + x_1 (y_2 - y_3))] \right. \right. \\ \left. \left. + \frac{|\vec{B}|^2}{2\mu_0} [x_1 (x_3 - x_2) + y_1 (y_3 - y_2)] \right] \right] \quad (3.50)$$

where e is the number of virtually distorted elements and i the number of virtually moved nodes within an element. A similar result can be written for a four noded bilinear element with node 1 having the virtual movement as Appendix A:

$$T = \frac{1}{2} \sum_e \sum_i \left[\left[\frac{1}{\mu_0} [B_x^2 x_1 (x_2 - x_4) + B_y^2 y_1 (y_2 - y_4) + B_x B_y (y_1 (x_2 - x_4) + x_1 (y_2 - y_4))] \right. \right. \\ \left. \left. + \frac{|\vec{B}|^2}{2\mu_0} [x_1 (x_4 - x_2) + y_1 (y_4 - y_2)] \right] \right] \quad (3.51)$$

It should be noted that in eqns. (3.50, 3.51) the movable node is always node 1 and if more than 1 node in a particular element moves there has to be a rotation in the labelling of the nodes. The labelling of the nodes should thus be done in only one direction, clockwise, to avoid the cancelation of different torque components within the computer program.

Chapter 4

Transient Performance

The transient response of permanent magnet dc motors is of great interest during start-up and braking conditions. The importance of being able to model these responses accurately is of great importance to manufacturers and industry wanting to use these motors. The high start-up and braking current surges are of importance since their magnitude can damage the rotor windings by causing overheating and high mechanical forces in structural members, or even demagnetize the permanent magnets. In industrial applications the high currents could also damage other equipment. These effects adversely affect the performance and reliability of the electrical motor.

A Classical approach and a finite element solution to calculating transient performance are described below.

4.1 Classical Approach

The classical approach to the calculation of transient performance is based on general machine theory. The assumptions made in the transient classical simulation are:

1. The segmental permanent magnets are modelled in the same manner as in the steady state simulation, assuming there are no transient effects on the magnets.
2. Eddy currents in the armature laminations are neglected.
3. The brush voltage drop is assumed constant even at very low voltages.

Since the armature current is not constant in a transient simulation, the airgap flux cannot be assumed constant either. The operating point of the PM has thus got to be

calculated for each time step and the useful magnetic flux density calculated, as was described in Chapter 2 on the steady state classical simulation. The general machine equations are:

$$V = R_a I_a + L \frac{dI_a}{dt} + k\omega_r + V_{br} \quad (4.1)$$

and

$$T_e = J \frac{d\omega_r}{dt} + T_m + T_{loss} \quad (4.2)$$

where V is the terminal voltage, V_{br} is the brush voltage drop, L is the inductance of the armature winding, T_e is the electromagnetic torque, T_m is the mechanical output torque, T_{loss} is the rotational torque losses, J is the moment of inertia of the total machine-load system and k is the machine constant defined as:

$$k = \frac{pN}{2\pi a} \Phi_g \quad (4.3)$$

where p is the number of pole pairs, N is the number of armature conductors, a is the number of current path pairs in the armature and Φ_g is the airgap magnetic flux per pole.

Eqns (4.1) and (4.2) are solved using Laplace transforms and a State Space approximation. The Laplace transform solution has been attempted since it will give a result at any time during the transient step without having to calculate the complete transient time solution to obtain just the one result, as is the case with the state space solution. The results from the two methods will be compared in Chapter 7.

The armature inductance and rotor inertia have to be calculated for the transient simulations. The armature inductance is calculated as [29]:

$$L = \frac{1}{48} \pi N^2 D l \left(\frac{b}{y} \right)^3 \frac{\mu_o}{l_g} \quad (4.4)$$

where b is the pole width, y is the pole pitch, D is the rotor diameter, N is the number of armature turns, l is the effective length of the rotor and l_g is the airgap length.

The armature inductance can also be calculated as [12]:

$$L = \Lambda \left(\frac{N}{4ap} \right)^2 10^{-8} \quad (4.5)$$

where

$$\Lambda = 0.33 \frac{\alpha^3 D l}{l_g} \quad (4.6)$$

where $\alpha = b/y$. Since the calculations, from eqns (4.4) and (4.5), of inductance are both seen as approximations the average result has been used in the simulation.

The inertia of the total system is calculated using [13]:

$$I = \sum_i M_i R_i^2 \quad (4.7)$$

where M_i is the mass of the object and R_i is its radius. The inertia of the rotor for the dc motor is calculated by calculating the separate inertias of the rotor shaft, rotor core and armature copper windings. The three inertia components are added together as well as the total inertia of the external load to obtain the total machine-load inertia J .

The brush voltage drop V_{br} is assumed to be constant throughout the entire armature current range, at 2 volts. The rotational losses are included in the simulation as a function of the rotor speed and the load torque is assumed to be constant and independent of rotor speed for this transient simulation.

4.1.1 Laplace Solution

The Laplace solution is done on one important assumption.

- The armature reaction is neglected.

This assumption needs clarification since the machine constant k is proportional to Φ_g , it is not constant due to the changing armature current during the transient simulation. The assumption is however made that k does not change during the transient simulation, since in the real machine k does not change a great deal, and thus the Laplace transform approximation can be used. The possible error in this simulation will be discussed later.

Although the inverse Laplace equations are based on the fact that the machine constant k is constant, in the simulation k is calculated for each value of armature current and rotor speed thus the Laplace solution differs for each time step, but is not dependent on any results obtained before or after it.

The eqns (4.1) and (4.2) are written using Laplace notation in matrix form as:

$$\begin{bmatrix} V_t \\ T_t \end{bmatrix} = \begin{bmatrix} R_a + Ls & k \\ k & -Js \end{bmatrix} \begin{bmatrix} I_a \\ \omega_r \end{bmatrix} \quad (4.8)$$

where $V_t = V - V_{br}$ and $T_t = T_m + T_{loss}$.

The equation (4.8) can be rewritten in terms of armature current and rotor speed as:

$$\begin{bmatrix} I_a \\ \omega_r \end{bmatrix} = \frac{1}{DET} \begin{bmatrix} -Js & -k \\ -k & R_a + Ls \end{bmatrix} \begin{bmatrix} V_t \\ T_t \end{bmatrix} \quad (4.9)$$

where

$$DET = \frac{1}{-Js(R_a + Ls) - k^2} \quad (4.10)$$

is the determinant of the matrix.

The start-up and braking simulations have to be considered separately since the Laplace equations differ for the two cases and the initial conditions are different.

Start-Up

The start-up calculation simulates the armature current and rotor speed for any time after the input voltage is applied to the motor. The sudden application of the input voltage means that in the Laplace domain there is a step input in voltage. The load on the motor is assumed constant throughout the whole simulation and thus independent of speed. The output load is also seen, in the Laplace domain, as a step input in torque. Eqn (4.9) is then written as:

$$\begin{bmatrix} I_a \\ \omega_r \end{bmatrix} = \frac{1}{DET} \begin{bmatrix} -Js & -k \\ -k & R_a + Ls \end{bmatrix} \begin{bmatrix} V_t/s \\ T_t/s \end{bmatrix} \quad (4.11)$$

The armature current and rotor speed can be written as:

$$\omega_r = \frac{kT_t}{LJ}C1 + \frac{V_t}{L}C2 \quad (4.12)$$

$$I_a = \frac{kV_t - T_tR_a}{LJ}C1 + \frac{V_t}{L}C2 \quad (4.13)$$

where

$$C1 = \frac{1}{s(s^2 + \frac{R_a}{L}s + \frac{k^2}{LJ})} \quad (4.14)$$

$$C2 = \frac{1}{s^2 + \frac{R_a}{L}s + \frac{k^2}{LJ}} \quad (4.15)$$

The inverse Laplace transforms of eqns (4.12) and (4.13) are shown in [27].

The initial conditions on the start-up simulation are that $I_a = 0$ and $\omega_r = 0$.

Rheostatic braking

Rheostatic braking is done by switching out the terminal voltage and switching in an external resistor at a time when the motor is running at steady state. The switching of the terminal voltage means that in the Laplace domain there is a negative step in voltage. The output load is assumed constant throughout the transient simulation and thus there is a negative step in output torque in the Laplace equations. Eqn (4.9) is then written as:

$$\begin{bmatrix} I_a \\ \omega_r \end{bmatrix} = \frac{1}{DET} \begin{bmatrix} -Js & -k \\ -k & R_t + Ls \end{bmatrix} \begin{bmatrix} -V_t/s \\ -T_t/s \end{bmatrix} \quad (4.16)$$

where $R_t = R_a + R_{ext}$ and where R_{ext} is the external resistor added for braking. Eqn (4.16) can be written in separate parts for rotor speed and armature current as:

$$\omega_r = -\frac{kT_t}{LJ}C1 - \frac{V_t}{L}C2 \quad (4.17)$$

$$I_a = -\frac{kV_t - T_tR_t}{LJ}C1 - \frac{V_t}{L}C2 \quad (4.18)$$

where C1 and C2 are the same as in eqns (4.14) and (4.15) respectively except that R_a in both equations is replaced with R_t .

The initial conditions for the transient rheostatic braking is calculated using the steady state results. The initial armature current and rotor speed is found from a look-up table for the specific terminal voltage and output torque.

4.1.2 State Space Solution

The State Space approximation is a linear approximation of the first order differential equations. The eqns (4.1) and (4.2) are rewritten as:

$$\frac{dI_a}{dt} = \frac{1}{L}(V - R_a I_a - k\omega_r - V_{br}) \quad (4.19)$$

and

$$\frac{d\omega_r}{dt} = \frac{1}{J}(T_e - T_m - T_{loss}) \quad (4.20)$$

The solution to the above derivatives is found using a linear approximation for a small time step. Eqns (4.19) and (4.20) are thus solved as:

$$\Delta I_a = \frac{1}{L}(V - R_a I_a - k\omega_r - V_{br})\Delta t \quad (4.21)$$

and

$$\Delta\omega_r = \frac{1}{J}(T_e - T_m - T_{loss})\Delta t \quad (4.22)$$

Thus at a specific time (t) the change in I_a and ω_r are both assumed to be linear functions for a time period (Δt) and the new I_a and ω_r are calculated for time ($t + \Delta t$) as:

$$\omega_{r(i+1)} = \Delta\omega_{r(i)} + \omega_{r(i)} \quad (4.23)$$

and

$$I_{a(i+1)} = \Delta I_{a(i)} + I_{a(i)} \quad (4.24)$$

The start-up and braking transient simulations use the same equations but with different initial conditions and with some parameter changes. In both simulations the transient change starts at time (t) = 0.

Start-up

The start-up initial conditions are $I_a = 0$ and $\omega_r = 0$ so $I_{a(0)} = 0$ and $\omega_{r(0)} = 0$ for eqns (4.23) and (4.24), assuming that at $t = 0$ and increment $i = 0$. The input voltage V and the output load T_m are set as constants.

The simulation is run until the steady state condition is reached. The accuracy of the simulation in terms of the number of time steps taken will be discussed in a later chapter.

Rheostatic braking

The initial conditions of I_a and ω_r in the braking simulation are taken from the steady state simulation for the particular value of terminal voltage and output torque. At the start of the braking transient the terminal voltage is switched out and a resistor added. This means that equ (4.21) becomes:

$$\Delta I_a = \frac{1}{L}(-R_t i_a - k\omega_r - V_{br})\Delta t \quad (4.25)$$

and equ (4.22) remains the same since the torque is seen as being constant throughout the transient simulation. The reversal of the armature current is seen as a negative current in reference to the simulation.

4.2 Finite Element Approach

The advantage of using the finite element method in transient simulations is the possibility of calculating the eddy current losses in the motor. The high armature currents mean that

saturation of the stator yoke and rotor stack become more important. The non-linearity of the ferromagnetic materials can easily be included into the finite element simulation.

Many papers have been written on the use of the finite element analysis method in the calculation of the transient performance of electrical machines [26],[15],[1]. Some of the analyses were done on the assumption that the rotor speed [5] is constant or that the armature current is known [32]. Other authors identified the need to combined generalized machine theory with a finite element simulation in an attempt to obtain the best possible transient results with the most effective saving of time [7],[25].

The finite element analysis of transient performance of the permanent magnet dc motor is based on the non-linear Newton-Raphson method. The analysis uses a two-dimensional model of the motor, as discussed in Chapter 3, with the following assumptions:

1. The source function is represented by a current density distribution in the ideal conductor as a function of time.
2. The displacement currents are neglected since they are negligible in comparison to the eddy currents.
3. The permeability of the iron is field and time dependent.
4. Eddy currents are assumed present in the iron and metallic structures of the motor.
5. Material conductivity is constant and single-valued.
6. Temperature effects on the electrical conductivity and permeability are ignored.
7. Edge effects are neglected and no field variations are assumed to occur in the axial direction (z-direction).

The Maxwell equation can thus be written as [31]:

$$\nabla \frac{1}{\mu} \nabla \vec{A} = -\sigma \frac{\partial \vec{A}}{\partial t} + J \quad (4.26)$$

using the above assumptions and where σ is the conductivity.

The energy functional can now be written using the Maxwells equation as is described in Chapter 3 as:

$$F = \int \int_R \left(\frac{1}{2\mu} B^2 - \frac{\sigma}{2} \vec{A} \cdot \frac{\partial \vec{A}}{\partial t} - \vec{J} \vec{A} \right) dR \quad (4.27)$$

The armature inductance can be found from the finite element simulation if the source to the permanent magnet is removed to eliminate any false mutual inductance between

the armature windings and the current sheet modelling of the permanent magnet. The inductance per slot is [4]:

$$L_{slot} = \frac{\lambda}{I} \quad (4.28)$$

where λ is the flux linkage and I is the armature slot current. The flux linkage is:

$$\lambda = N_{slot}\Phi \quad (4.29)$$

where N_{slot} is the number of coils in the slot and Φ is the coil flux.

The use of eqn (4.26) in calculating the start-up or braking transient performance is extremely time consuming. The problem is that the finite element computer package does not incorporate circuit theory into its transient analysis. The EMF of the motor has to be calculated separately from the finite element simulation and then the rotor speed can be calculated.

The solution to the problem is a finite element simulation package that incorporates circuit theory into its simulation. Using the general dc machine equations:

$$V = I_a R_a + L \frac{dI_a}{dt} + k\omega_r + V_{br} \quad (4.30)$$

and

$$T_l = T_e - J \frac{d\omega_r}{dt} - T_{loss} \quad (4.31)$$

and starting at time ($t=0$), with initial conditions for I_a and ω_r . The simulation as proposed is not implemented, due to the scope of this project and the lack of finite element source code. The simulation could however be run as follows:

1. Begin with initial I_a and ω_r
2. Calculate ΔI_a and $\Delta \omega_r$ using the present I_a and ω_r in eqns (4.30) and (4.31).
3. Assume a linear armature current change for a small time step Δt . Build I_a versus time plot as input to the finite element simulation and run the simulation for time Δt .
4. Obtain electromagnetic torque T_e and rotor core losses from the finite element solution.
5. Return to step 2 and repeat until steady state conditions are reached.

The problem with this type of solution is that if the new armature current and rotor speeds have to be calculated manually between running each finite element solution, and simulation will take a few weeks and that will only be for one specific transient simulation.

The finite element package available is good for simulations where the armature current versus time function is known and can be entered into the program. If the problem is one of finding the armature current function then the finite element package needs the modifications as state above, which is beyond the scope of this project.

4.2.1 Simpler Finite Element Solution

A simpler solution to the problem discussed above is one in which the eddy current losses are ignored. The real advantage of using the finite element is thus lost, but if the classical method is not available then this is a quicker, but not as accurate solution, to obtaining transient results using the finite element method.

The simulation would be run as follows:

1. Build-up a plot of electromagnetic torque versus armature current for a large range of armature currents using the finite element steady state simulation.
2. Set the initial conditions for I_a and ω_r .
3. The problem is then the same as for the classical linear simulation using the state space method. Except that the machine constant, for a particular armature current, is found using the finite element method and not by classical theory.
4. The simulation is run up till steady state.

The results from this method will be compared with the experimental results in Chapter 7.

Chapter 5

Physical Models and Data Acquisition System

5.1 Description of Motors

The two motors used in this project are both permanent magnet commutator direct current motors. The one being a 370 W motor manufacture by Baldor, FortSmith USA and the other a 8 W motor by Factory of Automobile Electrical Engineering in Duszniki Zdroj, Poland. The dimensions of the two motors as well as there winding diagrams are important to the success of the finite element and classical simulations.

The dimensions of the two motors differ considerably due to there power rating differences, but there general design is very similar. Table 5.1 lists both motors main dimensions and ratings. The windings of both motors are simplex lap windings. The commutation in both the motors is assumed to be linear for the finite element and classical simulations. Both motors use Barium Ferrite permanent magnets on there stators, the demagnetization curve for Barium Ferrite is shown in Appendix B. The B-H curves for the rotor core and stator yoke of the two motors are shown in Appendix B, as well as the specific loss curve for the rotor core (W/kg versus B).

The shape of the armature slots are considered in both the finite element and the classical simulations since there shape effects the performance characteristics of the motor. The general shape of a slot is shown in Chapter 2 and the measurements taken on it to be used in the simulations. Table 5.1 shows the slot dimensions for the two motors.

Table 5.1: Design data of tested motors

	370W motor	8 W motor	Units
Rated speed	1750	2800	rpm
Terminal voltage	180	24	V
Power rating	370	8	W
No. of pole pairs	1	1	
Shaft diameter	19	6	mm
Rotor diameter	82.5	41	mm
Airgap length	2.25	0.7	mm
Thickness of stator yoke	4.4	1.5	mm
Length of armature core	63.4	12	mm
Permanent magnet height	16.5	4	mm
Permanent magnet length	79.6	25	mm
Overlap angle of magnet	2.6878	1.832	rad
Armature slot skew	0	5	mm
Diameter of conductor	0.574	0.22	mm
No. of armature turns	920	560	
No. of armature slots	20	8	
Commutator segments	40	8	
No. of Coil-sides per slot	2	2	
No. of Coils per side	2	1	
No. of Turns per coil	23	56	
Stacking factor	0.96	0.96	
H21	0.0123	0.0075	m
H23	0.001263	0.0025	m
H24 Slot	0.0008	0.0006	m
B21 Dimensions	0.003398	0.003	m
B22	0.00731	0.00825	m
B24	0.003	0.0025	m

5.2 Data Acquisition System

The data acquisition system was build so that accurate results could be obtained for the 370 W motor in calculating the steady state performance as well as transient performance.

The calibration of the data acquisition system was done against reliable calibrated sources giving the data acquisition system a high accuracy. The calibration was repeatable thus increasing the confidence in the accuracy of the results.

The data acquisition system consists of 4 inputs from the motor test bed, a set of protection circuits and a link to the computer via a PC-30 analog to digital card, with 16 channels of 12 bit analog to digital converters. The inputs from the test rig are input voltage and input current supplied to the motor, the speed of the motor and the torque reading from the load cell. Fig 5.1 is a representative layout of the test rig.

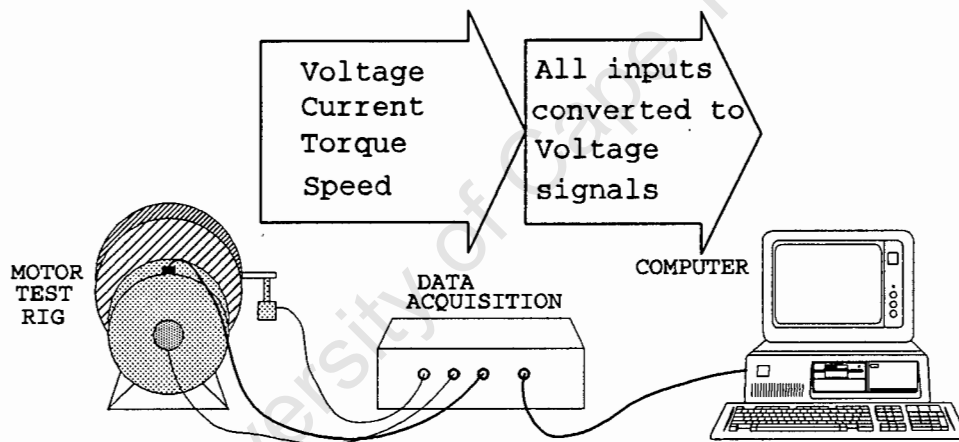


Figure 5.1: Layout of Test rig with data acquisition system and link to computer

The input voltage is measured using a potential divider to scale down the input voltage magnitude. The input current is read as the potential difference across a small resistor. The schematic circuit diagram for the current circuit is shown in Appendix C. The input voltage and current are isolated from the computer by photo coupled isolating circuitry to avoid any noise spikes from damaging the computer. The isolating is done by converting the input voltage signals into a frequency which is then transferred through the photo coupled isolating chips and then converted back to a voltage.

The speed is read using a opto-interrupting circuit which produces an frequency proportional to the rotor speed. This frequency is then converted into a voltage and fed into

the computer. The opto-interrupting is possible due to the disc fixed to the rotor shaft with 56 holes in it.

The torque is measured using a Sealed Universal Block Loadcell (SUB) that produces an output voltage proportional to the force applied to it. The SUB was supplied by Loadcell Services of Pretoria West with a rated accuracy of 0.2%. The output potential difference is obtained and fed into the computer.

The PC-30 analog to digital card placed on the computer bus is a 12 Mhz card. The computer is a standard 80286 16 Mhz IBM compatible machine. The PC-30 card uses Direct Memory Access of the computers memory to ensure the fastest possible reading of data. The data obtained is then read into Quattro Pro spread sheet package where it is scaled and the results obtained.

5.3 Calculating Performance on the basis of measurements

The performance of the two motors have been calculated using different methods. The 8 W motors performance was calculated using a manual method while the 370 W motors performance was calculated using a data acquisition system. It was felt that the use of a data acquisition system to measure the steady state performance of the 8 W motor had no benefits in terms of accuracy or convenience. The data acquisition system was however used in calculating the performance of the 370 W motor in an attempt to obtain the most accurate results for both steady state and transient performance.

Fig 5.2 shows a model of the 8 W motor performance testing rig. The test rig consists of a 8 W permanent magnet motor and a load which consists of a nylon string rapped around a drum with a weight on the one end and a spring scale on the other [24]. The voltage and current are both measured using fluke multimeters. The speed is measured using a optical tachometer, manufactured by Robin with an accuracy of 0.05/avoid the extra losses added when using a mechanical tachometer. The torque is measured using a spring scale, a weight and nylon string producing drag on the drum fixed to the rotor shaft [35]. No calibration is needed in this system since all the meters are precalibrated and there is only a offset known on the spring scale due to the initial mass. The load is changed by changing the weight or by increasing the number of turns the string goes around the drum. Both methods change the friction on the drum thus changing the load torque.

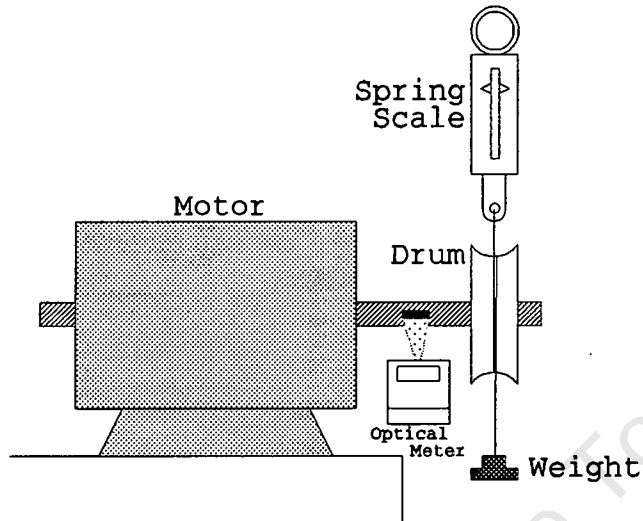


Figure 5.2: Test Rig for 8 W motors steady state performance

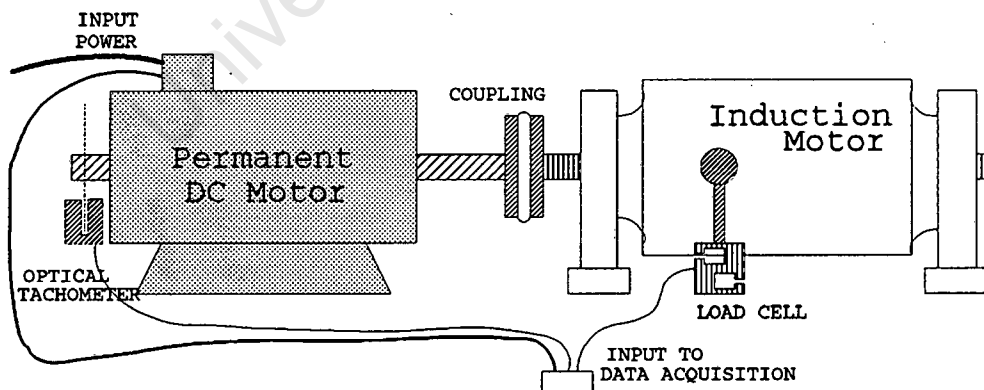


Figure 5.3: Test Rig for 370 W motor used for steady state and transient performance tests

The 370 W motor performance setup consists of an permanent magnet motor connected to an induction motor via a Fenner couple. The induction motors case is pivotally mounted on rocker bearings. The torque is measured from the induction motors case using a lever arm and a torque transducer (SUB). The model of the 370 W motor is shown in Fig 5.3.

The data acquisition system requires input voltages between 0 and 10 volts. The measurements are thus changed into voltages before being fed into the computer. The motor input voltage is scaled down using a resistors and the input current is converted into a voltage using a resistor and buffer. The speed is measured using a optical method using a disc with 56 holes in it. The large number of holes in the disc give the tachometer a quick response to any change in speed. The torque is measured using a load cell which produces an voltage proportional to the force placed on it.

The induction motor acts as the load. It is fed with direct current causing it to act as an dynamic brake [28].

5.4 Experimental Data

The experimental data was obtained for the two motors as explained above. The steady state results were measured for the full range of rated load conditions.

The results from the data acquisition system had in some case to be filtered to obtain the desired results and will be looked at closer.

The data acquisition systems output is shown in Fig 5.4. The voltage and speed results need only to be scaled to obtain there respective correct values. The input current shows a slight ripple on it, which has been ignored in the classical and finite element simulations, but which needs averaging out to obtain the average input current.

The load cell used to measure output torque picks up motor vibration on the test bed, due to its fast response time. This noise was not filtered out using hardware since the possibility of finding high harmonic cogging torque effects in the data was considered possible.

The torque reading shown in Fig 5.4 highlights the large vibrations picked-up by the sensitive transducer. In Appendix D a Fast Fourier analysis of this signal has been done. The results show that the main vibration is a 3rd harmonic in relation to the rotor speed. The 1st and 2nd harmonics are also present. These three harmonic components are due to the vibrations caused by the slight unbalanced rotor [34].

The high order harmonics were investigated in an attempt to determine the magnitude

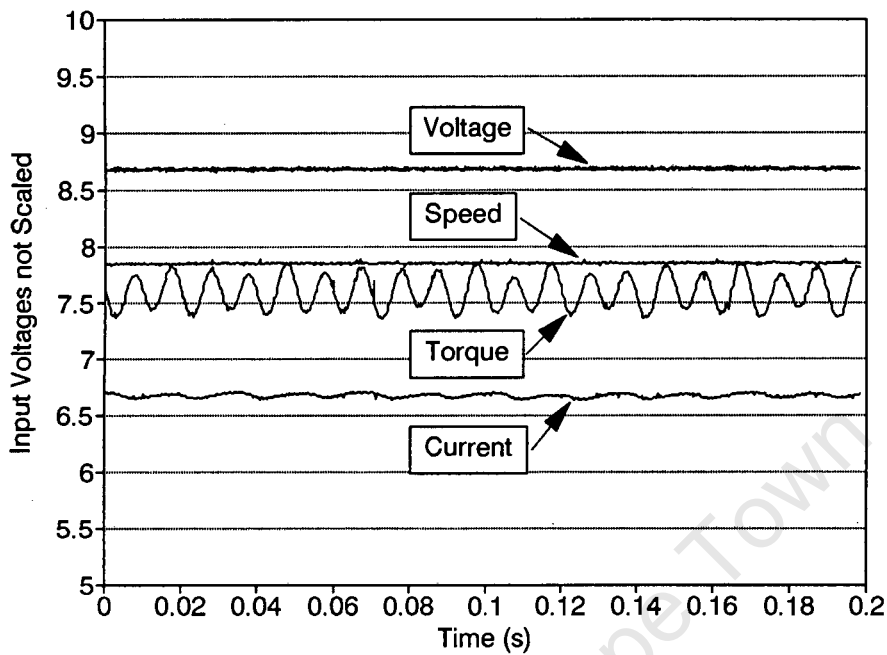


Figure 5.4: Un-scaled output from data acquisition system

of the cogging torques. As can be seen in Appendix D, there is no significant high order harmonics that could be identified solely with cogging torque, and not with noise from the bearings and commutator, and thus no results can be formulated with respect to cogging torque.

Chapter 6

Comparison of the Steady State Characteristics obtained from Classical Analysis, Finite Elements and Experiments

6.1 Classical Simulation

Calculating the performance of a permanent magnet motor using classical theory leads to the use of nonlinear simulation techniques. A computer program was thus written to do the calculation and speed up the simulation.

The Steady State performance calculations are done for a range of torque values ranging from a minimum torque (T_{min}), which is equal to the no-load rotor frictional torque, up to a maximum torque (T_{max}) which is approximately equal to the rated torque plus the rotor frictional torque. A torque increment is calculated, by the computer program, setting twenty intervals between T_{min} and T_{max} rated.

The computer program then sets the total machine torque to T_{min} and the computation to find the useful magnetic flux density is started. The iteration process within the program, shown in Fig 6.1, is as follows:

1. Estimate the useful magnetic flux density, B'_k .
2. Calculate the armature current (I_a) and the motor EMF, which is $EMF = V - I_a R_a - V_{br}$.

3. The armature reaction (F_a) is then calculated as described in Chapter 2. The field strength H_a and the armature field strength H_m are then calculated.
4. A new value for the useful magnetic flux density, B_u is then calculated.
5. If the error $e = ABS(\frac{B_u - B'_u}{B_u})$ is not less than 0.5% then a better approximation for the useful magnetic flux is made and return to (2).

Once the useful magnetic flux density is found the power losses in the motor can be calculated. The power in, power out and efficiency are then calculated. The output data is then written to an output text file. The torque is then incremented and the process repeated. This is done until the torque is greater than T_{max} plus T_{min} (Fig 6.1).

The results from the classical simulation were written to a output file by the computer program. The output data contains all the useful information needed about the motor per torque step. Graphs of the output results are shown Section 6.3.

6.2 Finite Element Simulation

The general finite element model is first described. The methods of calculating electromagnetic torque are then compared.

6.2.1 Finite Element Models

The shape of the magnetic circuits of the analyzed motors are shown in Fig 6.2. Both machines are 2 pole motors, which means that only half of each motor needed modelling due to symmetry in the motors.

A Dirichlet boundary condition or single point constraint (SPC) have been setup on the outer boundary of the stator yoke with a value of vector potential (A) = 0. The cross section through the motor have a periodic multi-point constraint (MPC) of -1 set along it [3].

The non-linearity of the rotor core and stator yoke materials have been included in the simulation by using the B-H curves. The core loss per kilogram versus magnetic flux density for the rotor core have also been included using the specific core loss curve.

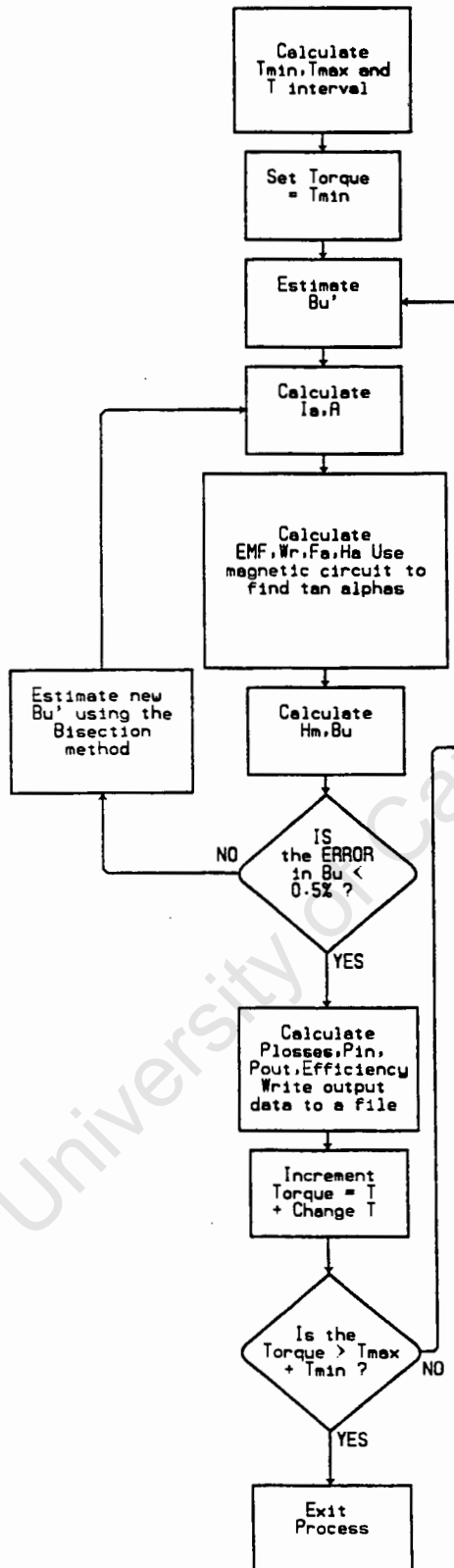


Figure 6.1: Flow Chart showing the logical flow of the Steady State Computer Simulation

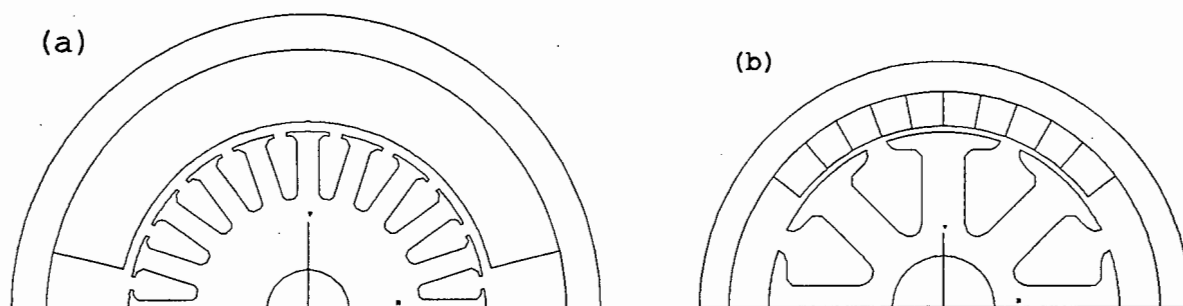


Figure 6.2: Cross sections of magnetic circuits of: (a) 370-W motor, (b) 8-W motor

6.2.2 Torque Calculation

The method of calculating torque by the different techniques is first considered. The accuracy and time efficiency of the different methods is compared later.

The four torque calculation methods described in Chapter 3 all use different algorithms, but the Maxwell stress tensor methods and the co-energy exact derivative method use short computer programs in calculating the torque.

The co-energy finite difference method calculates the torque by finding the difference in co-energy between 2 models with a small change in rotor position between them ($\Delta\theta = 0.1^\circ - 0.5^\circ$). This means that 2 models have to be build and simulated to find the torque at one rotor position. Since the finite element package calculates the total co-energy for each model the final calculation of torque is very easy.

The co-energy exact derivative method and Maxwell stress tensor area and line integration methods all need a greater amount of information from the finite element simulation, concerning the airgap elements (Fig 6.3). The coordinates and the values of magnetic flux density of each element within the airgap is needed to calculate the torque. The different methods manipulate the data differently but the initial raw information is identical. For this reason a short computer program was written that sorts through the airgap finding the path of linking elements across the whole model and writes a file containing element numbers and the coordinates of the grid points for each corresponding element.

Three separate programs were written to calculate the torque for the different methods using the above programs output and the output from the finite element program.

The Maxwell stress tensor line integration method has been written so that it calculates

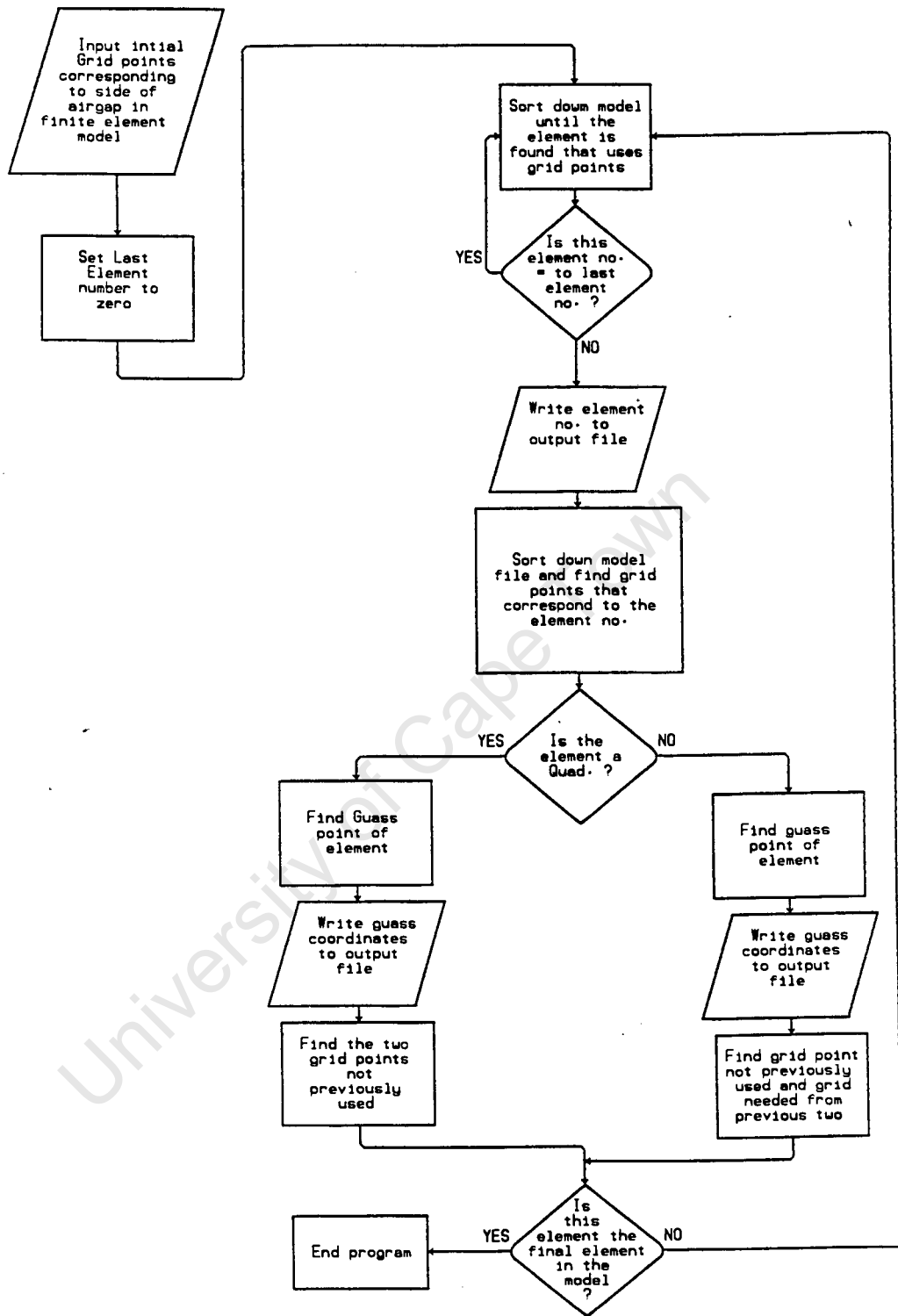


Figure 6.3: Flow Chart showing the Logical calculation of the Airgap path

the average torque from a number of line integrals through the airgap depending on the number of elements making up the airgap.

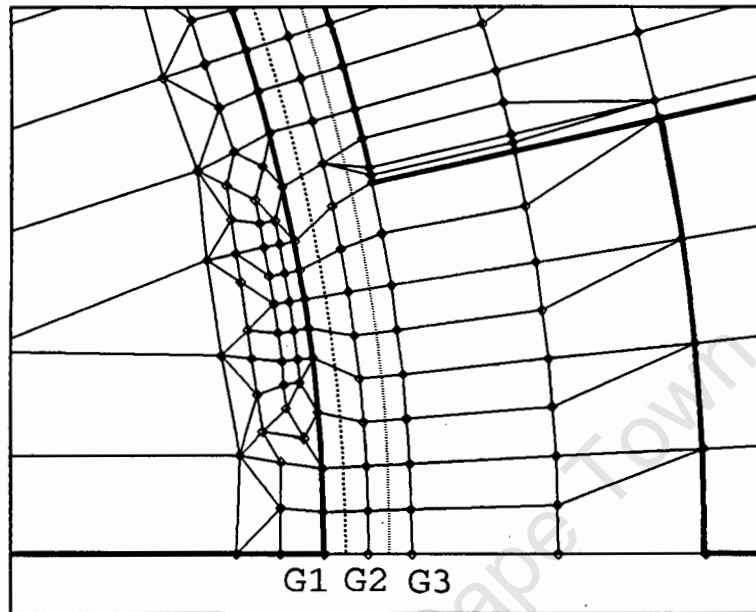


Figure 6.4: Meshed Area of finite element model showing Elements making up the Airgap area

The Maxwell stress tensor area integration method uses all the elements in the airgap but the thickness of the elements in the airgap has to be kept constant, Fig 6.4. This means that artificially thin elements have to be used in the area between the rotor and stator where the permanent magnet does not extend to. This is needed due to the use of a constant airgap length that is not able to distinguish between the airgap that falls under the rotor-permanent magnet or that falls under the rotor-stator yoke.

The co-energy exact derivative method is a little more complicated than the Maxwell stress tensor methods since this method has to know the relative position of the different grid points within each element so that the virtual movement can be placed on the correct elements and that all movable grid points are used in the calculation. This analysis is done on one layer of airgap elements at a time, but if there are more than one layer of airgap elements an average result is calculated, as is the case with the Maxwell stress tensor line integration method.

6.3 Comparison of Results

The experimental results are presented in Chapter 5. The comparison is done using the armature current, rotor speed, output power and motor efficiency versus output torque.

The results for the 370 W motor are shown in Figs 6.5, 6.6, 6.7, 6.8 and for the 8 W motor in Figs 6.9, 6.10, 6.11, 6.12.

The simulation results correlate well with the experimental result in the case of the 370 W motor and to a lesser degree in the case of the 8 W motor. The reasons for the discrepancies are numerous and differ for the classical analysis to the finite element simulations. Some of the more important discrepancies are common to both the classical and finite element analyses and are discussed below.

1. *Rotational losses* are calculated using the formula as stated in Chapter 2. Since the finite element simulation program cannot calculate mechanical quantities, when doing an electromagnetic analysis, the same formulas are used in the finite element simulation. The result is that both the classical and the finite element simulations are affected by the accuracy of the rotational loss calculations. Table 6.1 is a comparison between the calculated rotational losses and the measured quantity for the 370 W motor. The efficiency curves show that the rotational losses in the 370 W motor are under estimated and in the case of the 8 W motor they are over estimated. The problem is thus that the factors set within the rotational loss equations have to be different for the two machines, but it is very difficult to set-up fixed rules as to the value of these factors.
2. *Demagnetization curve* of the permanent magnet is assumed to be a fixed B-H curve for this Barium Ferrite magnet. The problem is that the B-H curve for this type of magnet can vary over a period of a few years and can vary from one manufacture to another. The standard B-H curve could thus possibly not represent the true demagnetization characteristic of the actual magnets.
3. *The errors in the measurements* in the 8 W motor case can be as high as 15%, which will affect the true accuracy of the simulations. The accuracy in the 370 W motor case is below 10% and thus would have a lesser effect on its results.

The errors specific to the classical analysis can be identified in a number of areas:

1. The classical analysis of calculation is on a 1-dimensional model. For small electrical machines the edge effects are significant and cannot be neglected.

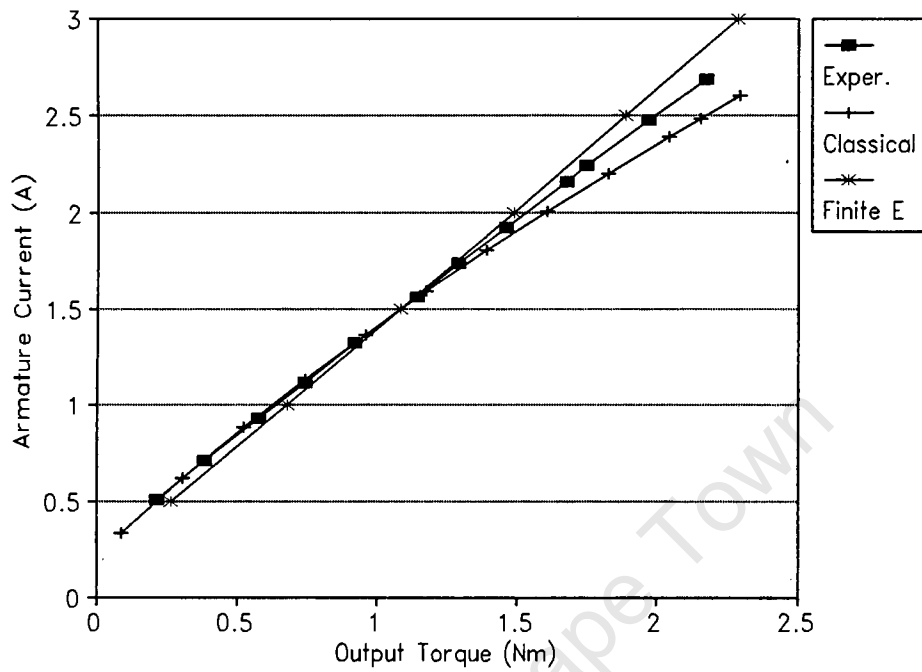


Figure 6.5: Input armature current versus output rotor torque for 370 W motor

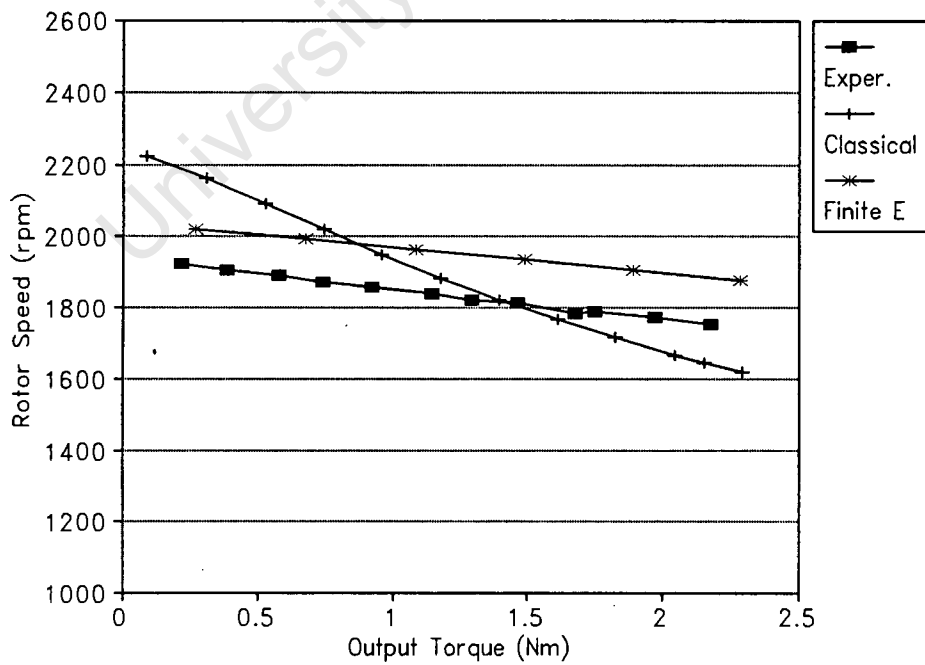


Figure 6.6: Rotor speed versus output rotor torque for 370 W motor

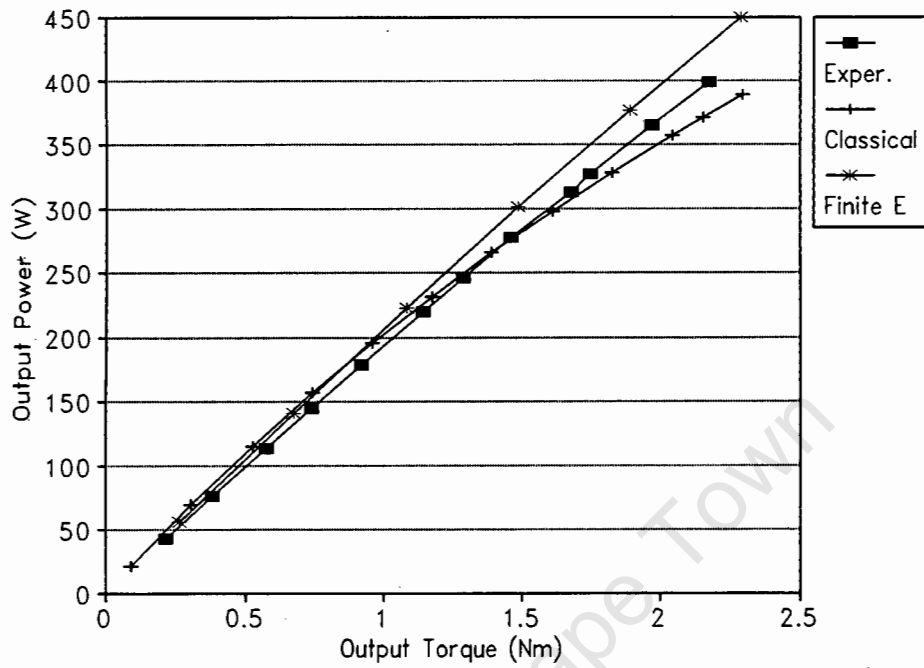


Figure 6.7: Output power versus output rotor torque for 370 W motor

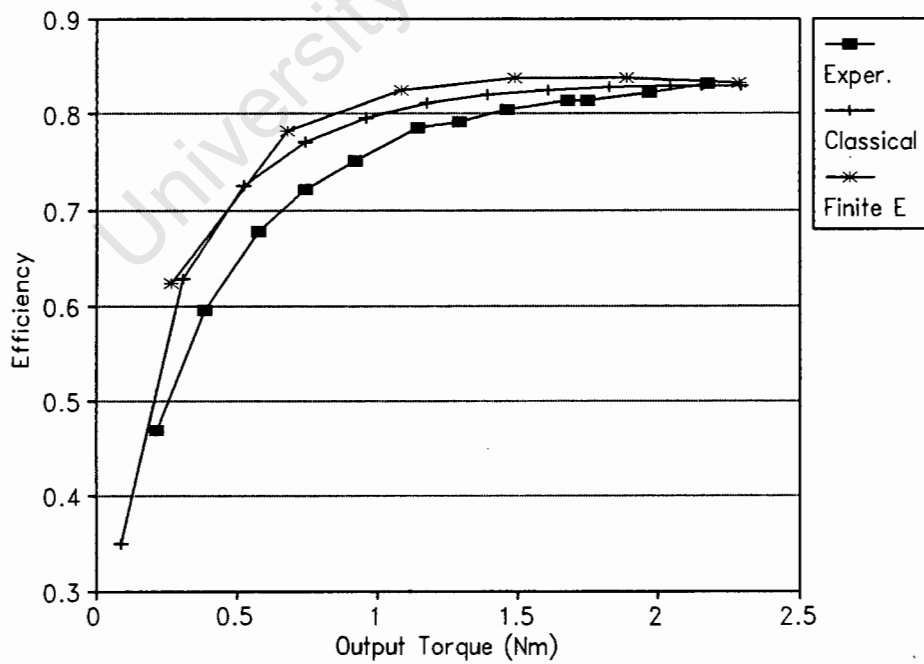


Figure 6.8: Motor efficiency versus output rotor torque for 370 W motor

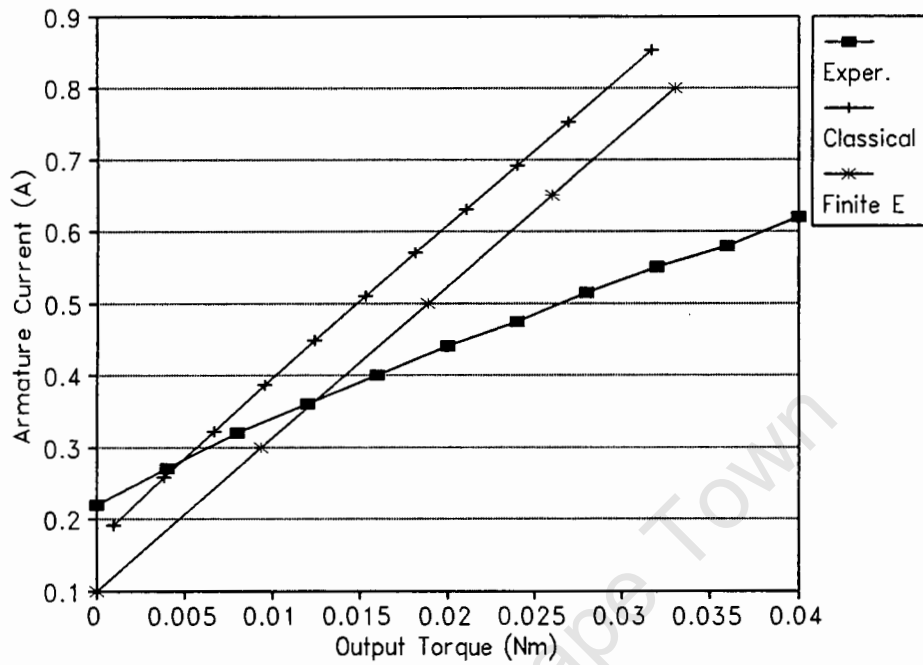


Figure 6.9: Input armature current versus output rotor torque for 8 W motor

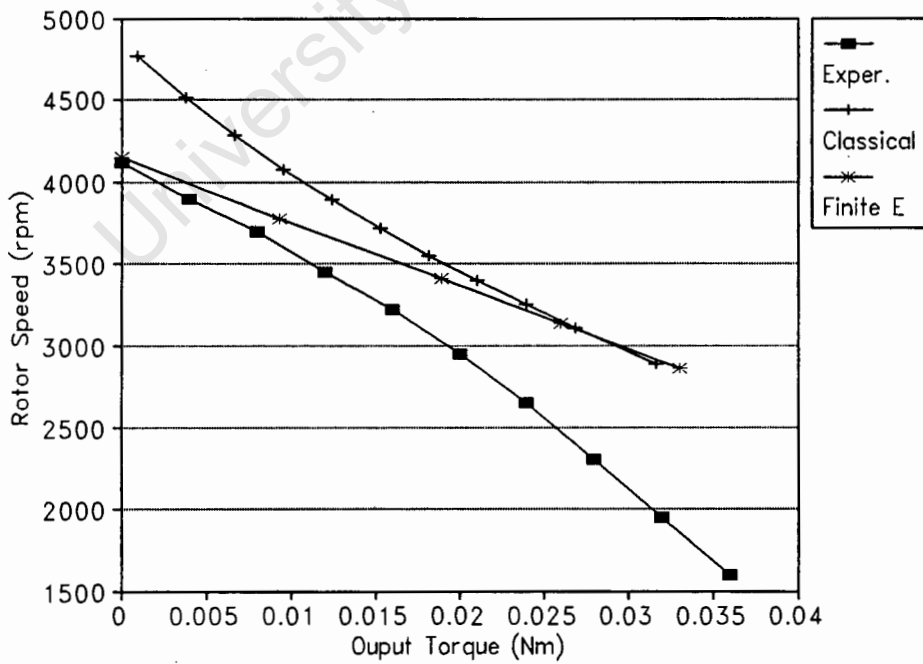


Figure 6.10: Rotor speed versus output rotor torque for 8 W motor

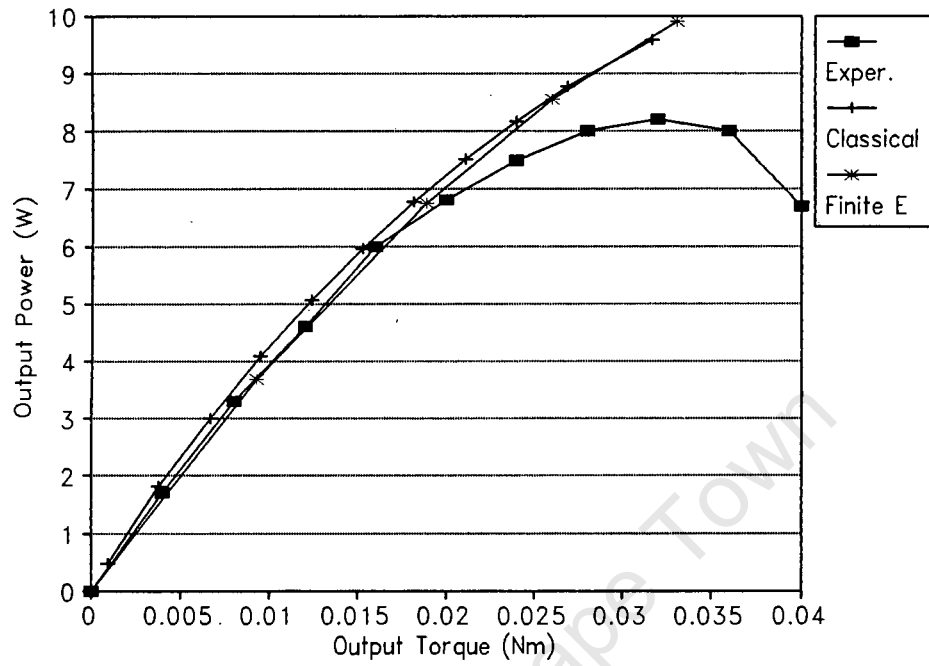


Figure 6.11: Output power versus output rotor torque for 8 W motor

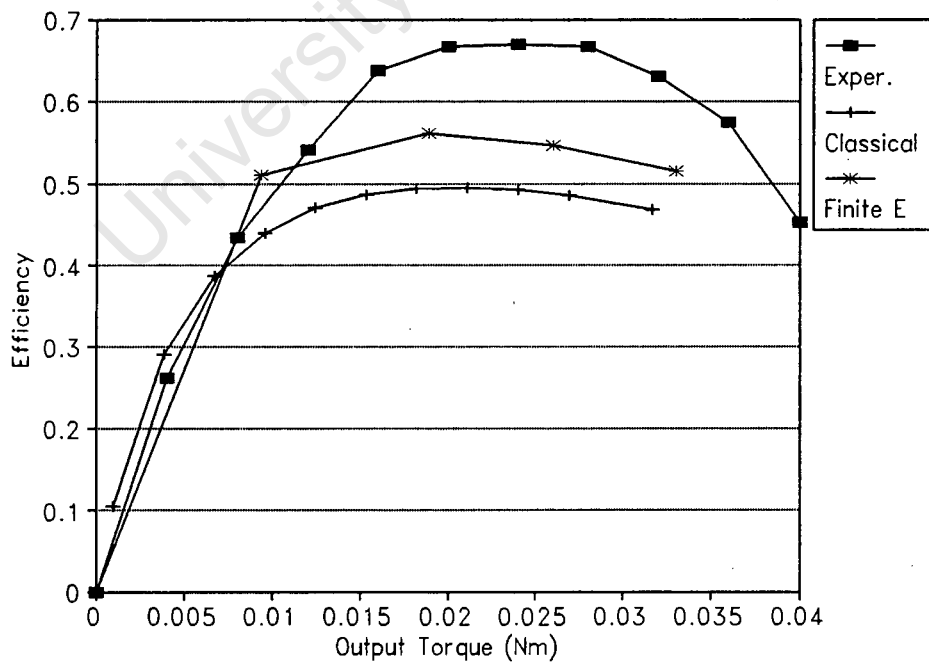


Figure 6.12: Motor efficiency versus output rotor torque for 8 W motor

Table 6.1: Comparison of Rotational Losses measured and calculated for the 370 W and 8 W dc motors

370 W Motor			8 W Motor		
Speed (rpm)	Experimental (watts)	Classical (watts)	Speed (rpm)	Experimental (watts)	Classical (watts)
1650	31.69	24.80	2700	0.978	1.351
1750	35.68	26.30	2800	1.014	1.401
1850	39.46	27.80	2950	1.069	1.476

2. The operating point on the demagnetization B-H curve of the PM is effected by the armature reaction (MMF) which is not accurately taken into account [11].
3. Since there are a low number of rotor slots per pole pair (4-10) in both of the tested motors this results in the commutation zone, the high slot loading and the stepped armature MMF waveforms becoming important. The total flux should be calculated for different tooth-slot regions within the airgap and thus the 1-dimensional average flux calculation can produce greater errors in the classical analysis [36].

The errors specific to the finite element analysis can be identified as:

1. The B-H curves of materials are used in the finite element analysis since saturation in the different part of the motor is taken into account. The knee point of different manufacturers materials vary slightly, but this difference can effect the finite element results.
2. The finite element model is a 2-dimensional model and for this reason the stator yoke of the model had to be thickened to take into account the yoke magnetic flux paths outside the permanent magnet. This could lead to the MMF not being accurately calculated and thus performance errors resulting.
3. The current density within the slots are assumed to be constant and the slots are simulated as single layer windings. The windings are in fact double layer windings.

6.4 Optimization of the Finite element models

The accuracy and optimization of the finite element models meant investigating all aspects of the model and ways of obtaining the best results.

The density of the finite element mesh and the amount of motor needed to be modelled are important considerations when building a finite element model, due to the lengthy simulation time. The method of calculation torque can also lead to a very time consuming exercise without leading to an improvement in the accuracy of the results. Since the motor was simulated using only a two dimensional model the simplifications for doing so had also to be considered.

The final models used in the simulation are shown at the end of the optimization process. These models are used not only for the steady state simulation but also in the transient simulation.

6.4.1 Accuracy of the torque calculation methods

The Maxwell stress tensor method is seen as the simplest method of torque calculation since it only requires the magnetic flux density along a path within the airgap. Studies have shown that its accuracy can be markedly dependent on the model discretization and on the selection of integrating paths [22], [20]. The use of the Maxwell stress tensor area integration eliminates the restriction of contour selection imposed by the conventional Maxwell stress tensor method [6].

The same accuracy of torque results from the Maxwell stress tensor method can be obtained using a much courser mesh when the co-energy method is used, since it takes the energy of the whole model is taken into account [22], [20]. The numerical differentiation of the co-energy method can introduce significant rounding off errors [9], [22]. The co-energy exact derivative method avoids the trial-and-error procedure of selecting a proper incremental displacement value needed in the co-energy finite difference method [6].

The accuracy of the co-energy finite difference method is dependent on the value taken for $\Delta\theta$ as mentioned in Chapter 3. Since the most ideal value of $\Delta\theta$ is not know it was decided to evaluate the co-energy finite difference method for two values of $\Delta\theta$ to see how crucial this increment is and to see whether an ideal value of $\Delta\theta$ could be found. An $\Delta\theta$ of 0.1° and 0.5° were used.

The Maxwell stress tensor line integral and the co-energy exact derivative methods both use the average over the airgap elements instead of only using one layer of elements so as to improve there accuracy. Depending on the density of the elements in the finite element model the number of layers of elements making up the airgap can vary from 1 to 4.

The Maxwell stress tensor area integral method uses all the elements in the airgap as

defined.

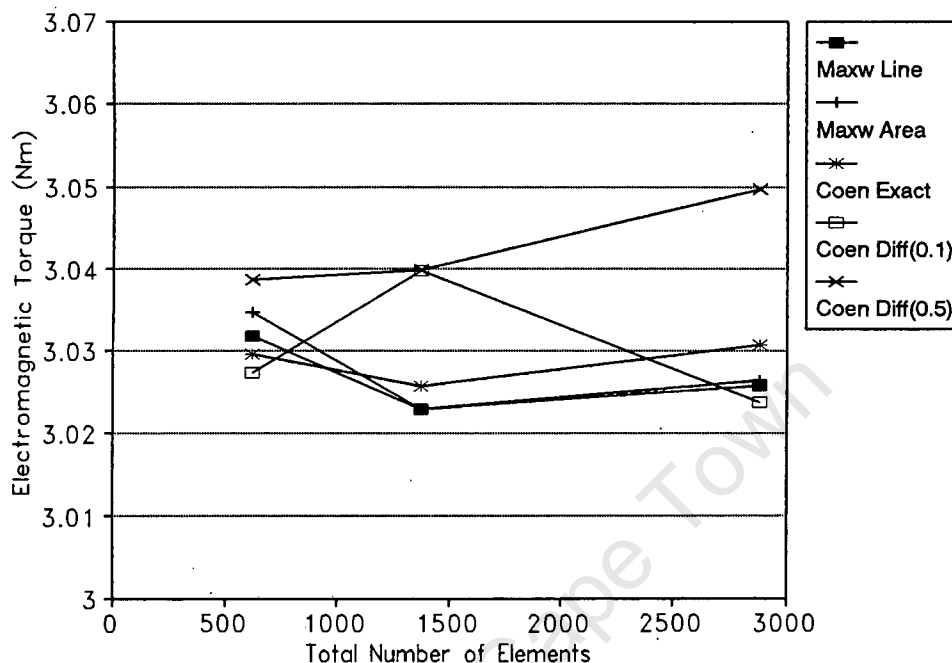


Figure 6.13: Electromagnetic Torque versus the increase in the number of elements used in the model for the 370W motor with 3 A armature current

Figs 6.13,6.14,6.15 show the torque versus an increase in the total number of elements making up the model. The torque comparison is done for a 8 watt and a 370 watt motor and for different load conditions to ensure that the methods are consistent over a full load range and for different motors.

From Figs 6.13,6.14,6.15 it can be seen that the Maxwell stress tensor methods and the co-energy exact derivative method give similar results across most of the increase in element range.

The co-energy finite difference method however does not give consistent results with an increase in the number of elements per model. The value of $\Delta\theta$ also has a noticeable effect on the torque calculation.

The Maxwell stress tensor methods and the co-energy exact derivative method take in general the same amount of time since the calculation of torque after the finite element result is obtained is negligible in comparison to the finite element simulation time (Table 6.2).

The Co-energy finite difference method however takes a lot longer since two finite element simulations have to be run to obtain the torque result for one rotor position.

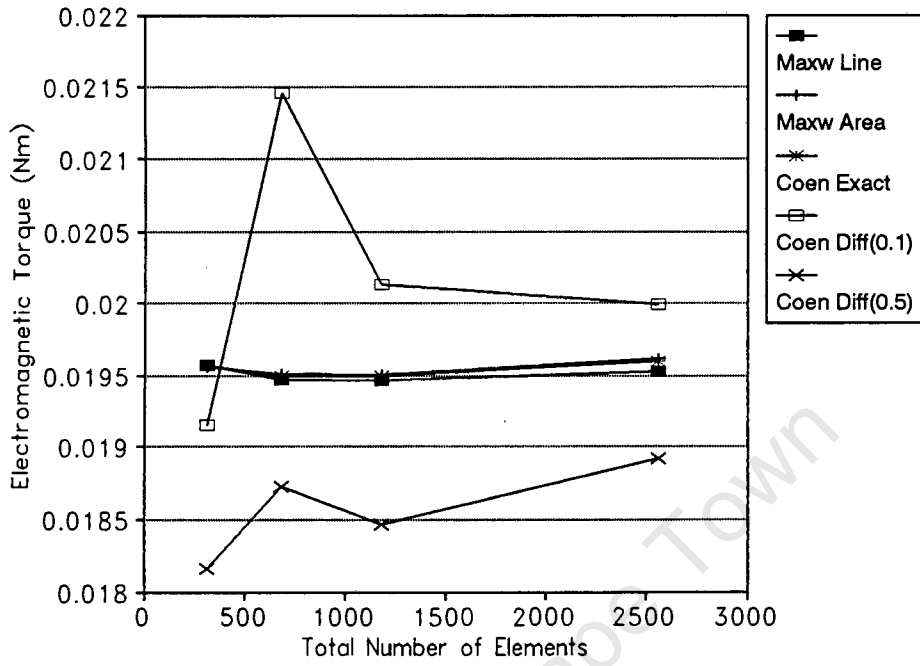


Figure 6.14: Electromagnetic Torque versus the increase in the number of elements used in the model for the 8W motor with 0.8 A armature current

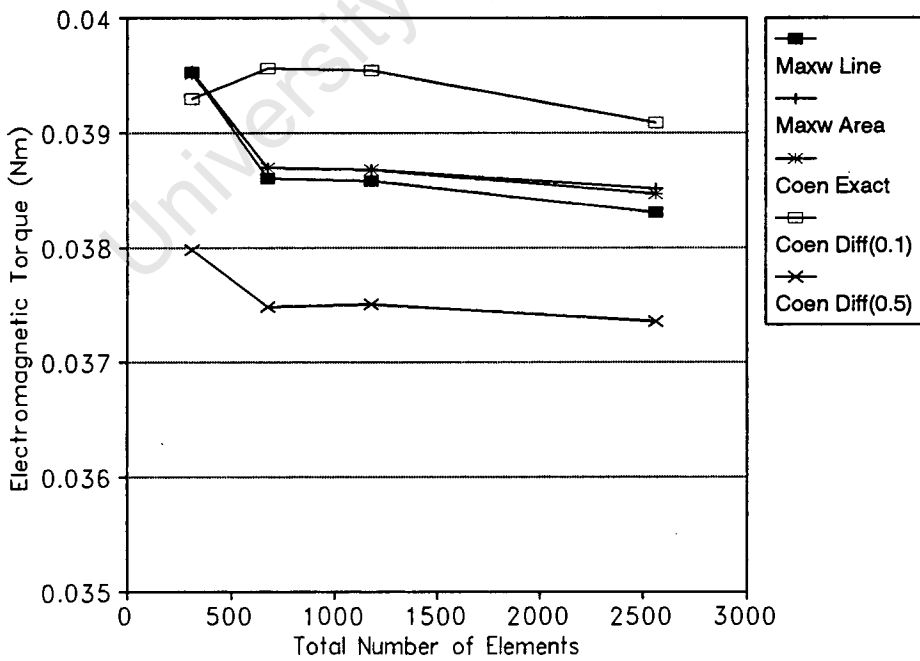


Figure 6.15: Electromagnetic Torque versus the increase in the number of elements used in the model for the 8W motor with 1.6 A armature current

Table 6.2: Processing times for different torque calculation methods

Motor rating	Number of Elements	Time of calculation (s)		
		Maxwells Tensor	Co-Eng. Exact	Co-Eng. Differ.
370 W	618	70	72	140
	1376	1581	1589	3162
	2886	4109	4125	8218
8 W	310	39	40	78
	680	77	79	154
	1178	1354	1360	2708
	2562	3648	3659	7296

The Maxwell stress tensor area integration method was decided to be used since its calculation algorithm is the easiest to implement and thus avoiding any rounding off errors that may occur within the short computer program to calculate torque.

The density of the finite element model relates to the accuracy of the result. The number of elements have to be great enough to describe the physical model without compromising the structure of the model drastically. The best accuracy in torque calculations with the least number of elements is the most ideal model since the simulation time increase faster than the increase in the number of elements, as can be seen in Table 6.2. The graph of torque versus element number, Figs 6.13,6.14,6.15, shows that a confident result can be obtained using just above a 1000 elements without spending to much time on the simulation in both models.

6.4.2 Thickness of the Stator Yoke

The finite element package used in the simulation of the motor was not able to simulate 3 dimensional models so the effect of having a longer stator yoke than armature rotor could not be considered. In the 2 dimensional model this effect will lead to over saturation of the stator yoke and thus a reduced performance from the simulation.

The effect of increasing the stator yoke thickness on the torque calculation is shown in Figs 6.16,6.17. The thickness of the stator yoke can be seen to have an drastic effect on the torque calculation.

From Figs 6.16,6.17 it can be seen that the operating point of the motor is somewhere between 0 % and 400 % increase in the stator yoke. The highest thickness being where there is no saturation within the stator yoke at all. This thickness is felt to be to high

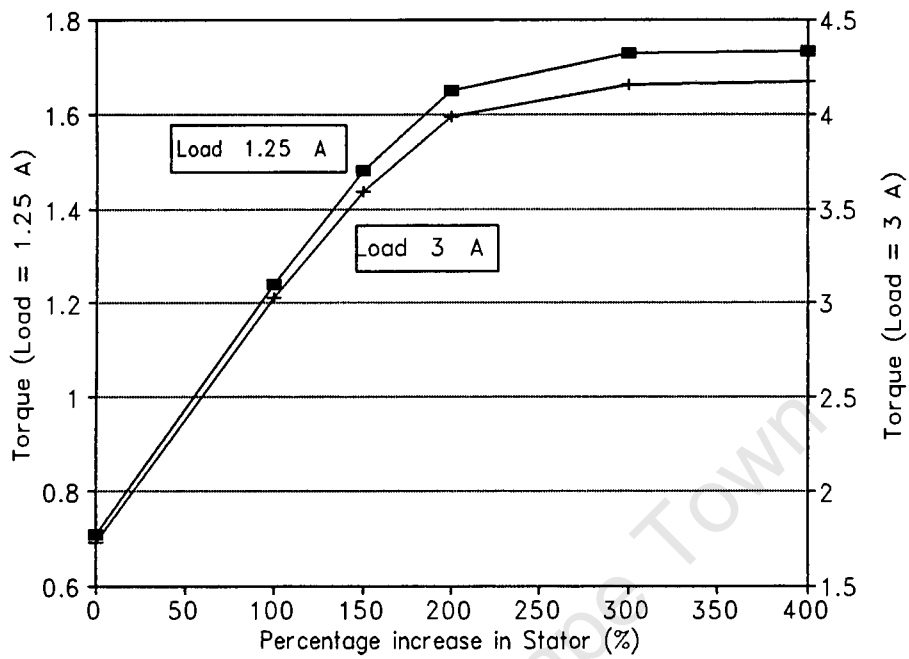


Figure 6.16: Torque versus increase in stator thickness for the 370W motor

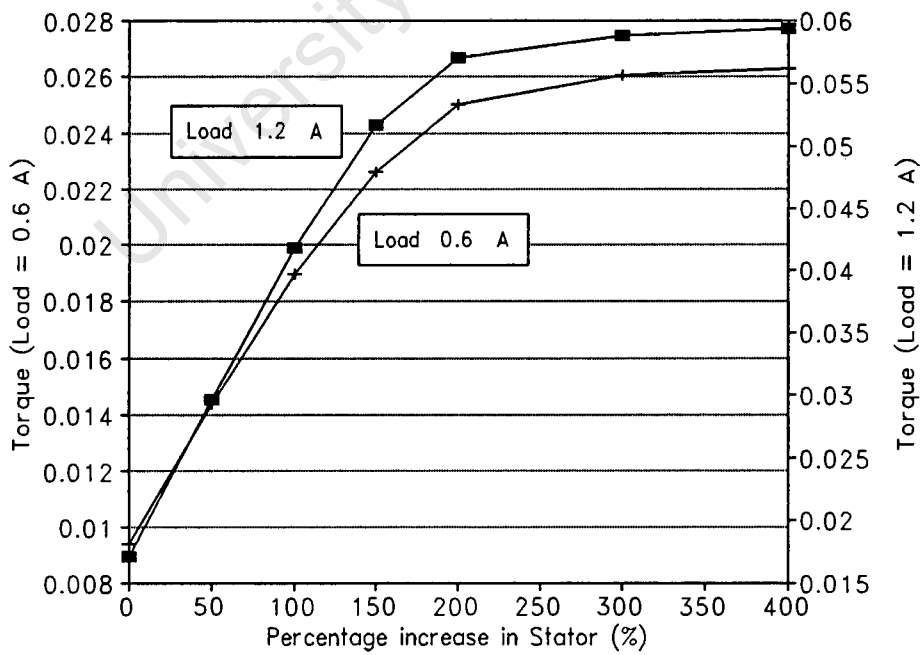


Figure 6.17: Torque versus increase in stator thickness for the 8W motor

since the author expects to find a small amount of saturation within the yoke.

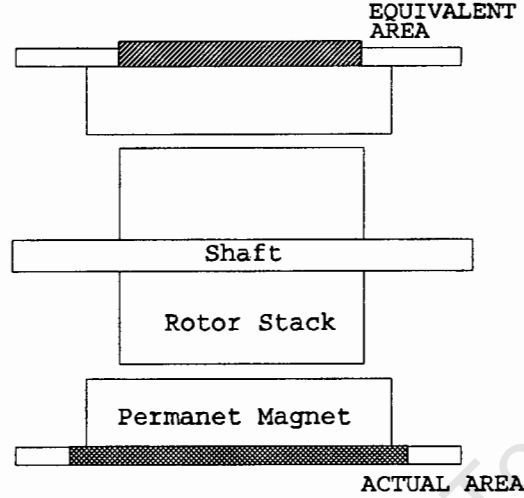


Figure 6.18: Side view through a motor to show the equivalent stator thickness used in the finite element simulation

The equivalent thickness of the stator yoke is found using the equivalent area of the stator yoke assuming that the total area is that above the permanent magnet plus a small amount equal to the thickness of the stator yoke. This area is then assumed to fit into a stator yoke of the same length as the rotor, as shown in Fig 6.18.

$$TotalArea = DK.(LM + 2.DK) \tag{6.1}$$

where DK is the stator yoke thickness and LM is the length of the permanent magnet.

$$EquivalentStatorThickness = \frac{TotalArea}{LA} \tag{6.2}$$

where LA is the length of the rotor core.

6.4.3 Simulation of Permanent Magnet

The finite element package allows the user to setup a permanent magnet material by specifying the magnets magnetization magnitude and direction. To simulate a radial magnet the permanent magnet has to be broken up into smaller magnets all with different magnetization directions. A sheet current equivalent to the permanent magnet can also be used which avoids the breaking up of the magnet into different parts since it can easily

Table 6.3: Increase in stator thickness used in models

Motor Power Rating	DK	LM	LA	Equivalent Stator Thickness	% increase in Stator Thickness
370 W	4.5	79.6	63.4	6.135	39 %
8 W	1.5	25	12	3.5	133 %

simulate a radial magnet. The two methods of simulating a permanent magnet have been compared since the motors tested have large overlap angles on their permanent magnets and the sheet current simulation is thus an easier option.

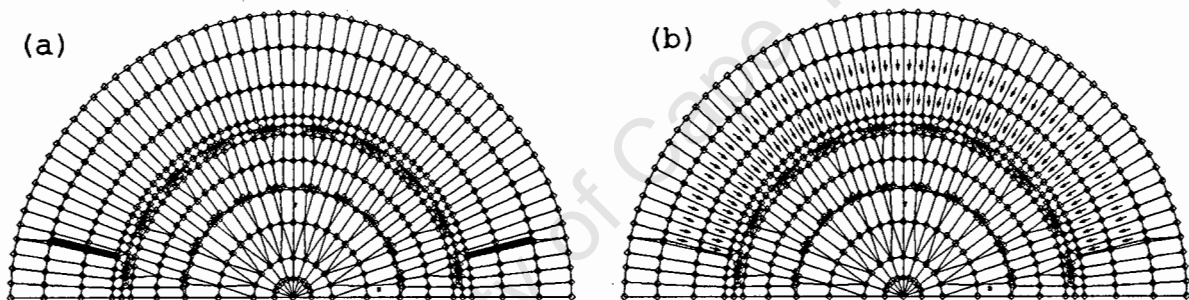


Figure 6.19: Models of the two types of permanent magnet equivalents used in finite element simulations: (a) sheet current equivalent (b) material definition in program

Fig 6.19 show the two models using the different permanent magnet equivalents. Torque is the most important result from the finite element simulation so a comparison of torque versus output load for the two models has been done.

Fig 6.20 shows that either simulation of the permanent magnet can be used since they both give similar results.

6.4.4 The Final Models

The torque calculation analyses showed that the most appropriate torque calculation technique is the Maxwell stress tensor area integration method. The analyses also showed that the number of elements used in the finite element models should be around 1000 elements to ensure good accuracy from the model without having to wait too time. Figs

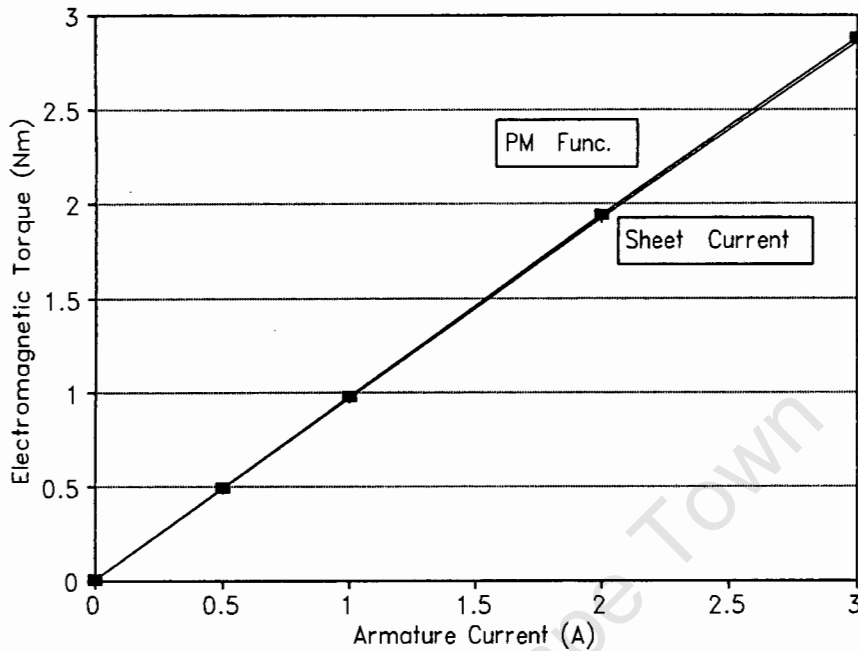


Figure 6.20: Comparison of torque calculations for the two types of permanent magnet models over a full range of loads for the 370W motor

6.21 and 6.22 show the final mesh diagrams for the two motors used.

The stator thicknesses in both models have been increased as mentioned above. The 370 W motor is shown using a sheet current equivalent for the permanent magnet while the 8 W motor is shown using the permanent magnet function. Since both models for the magnets give the same results, it does not matter which one is used.

A set of flux plots for different load conditions and for different rotor positions is shown in Figs 6.23 and 6.24. The armature reaction can be seen clearly in Figs 6.23 and 6.24 as the armature current is increased. The continuous flow of the flux lines show that the element size in the finite element models are small enough.

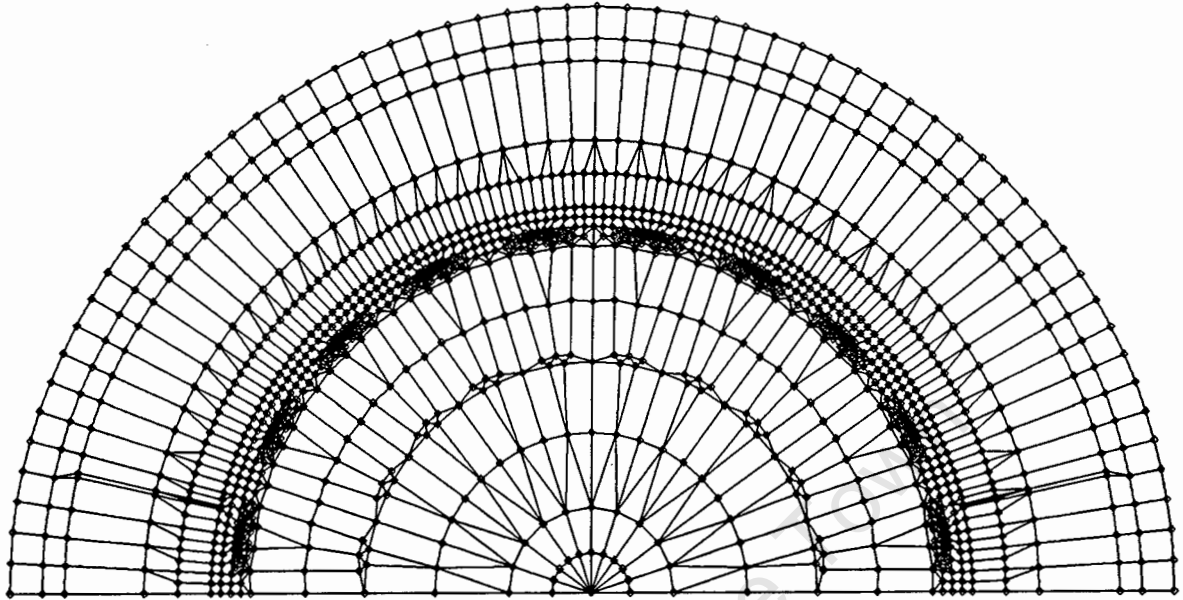


Figure 6.21: Element layout for 370 W motor. The model uses 1300 elements

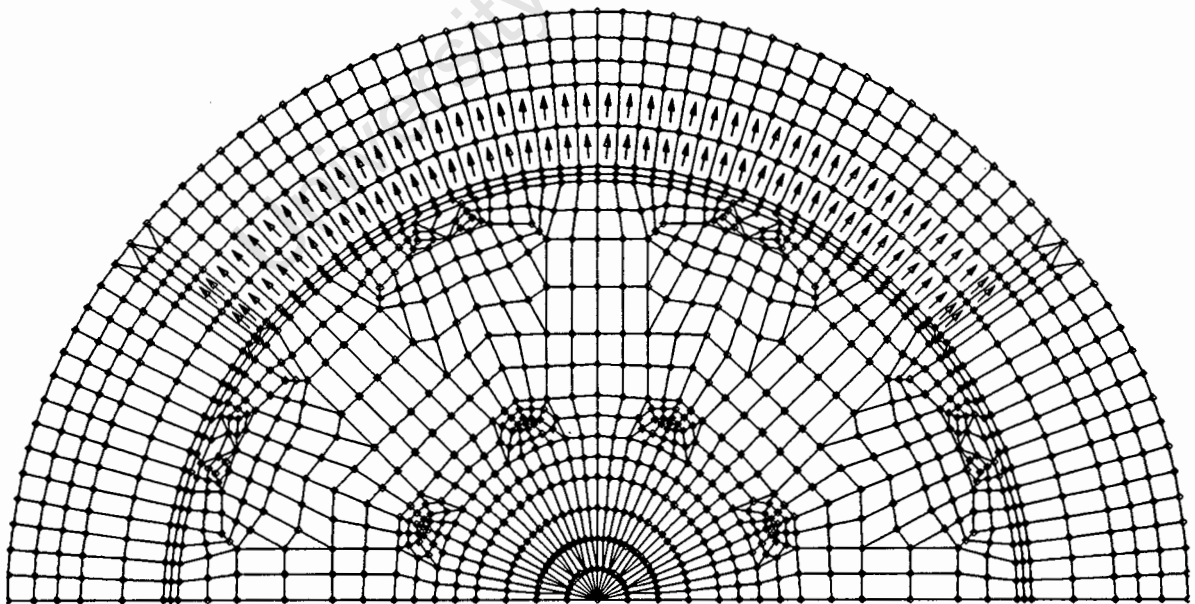


Figure 6.22: Element layout for 8 W motor. The model uses 1150 elements

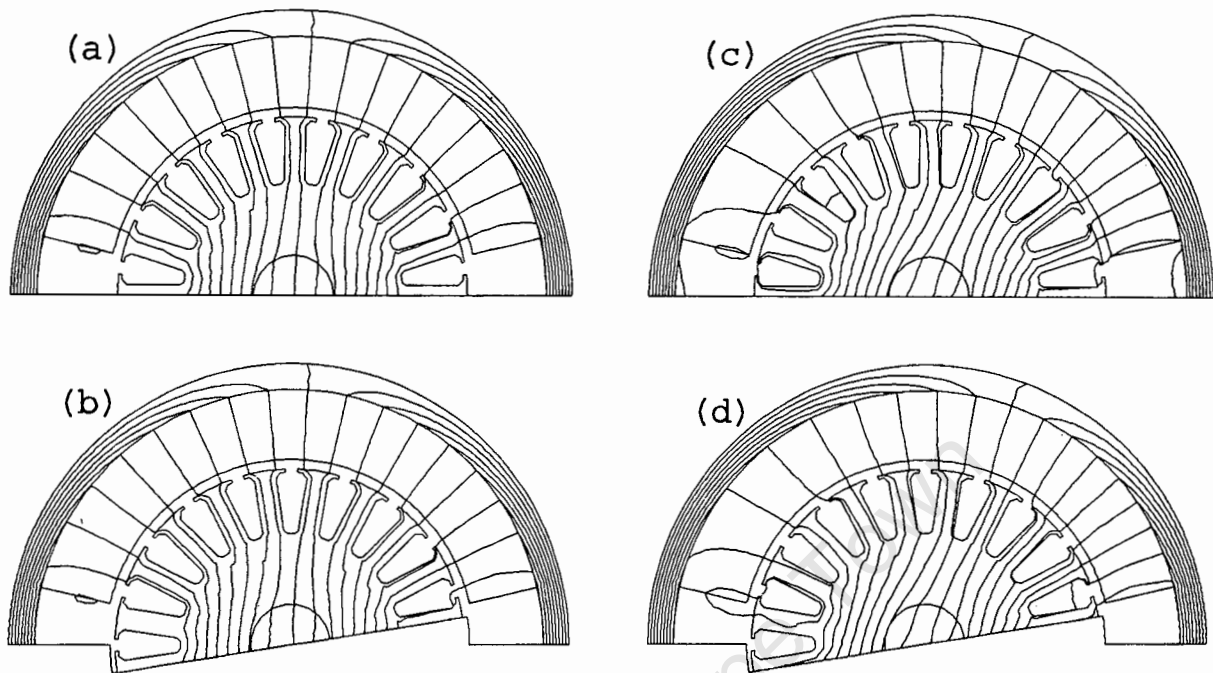


Figure 6.23: Flux plots used in the calculation of torque for 370 W motor. (a), (b) have armature current of 0.5 A, and (c) and (d) a armature current of 3 A. (a),(c) have $\theta = 0^\circ$ and (b),(d) have $\theta = 9^\circ$

6.5 Core Losses in the finite element simulation

The core loss in watts per kilogram is graphed versus the peak magnetic flux density B for laminations carrying uniform B . The peak B is the maximum B over a sinusoidal cycle of applied magnetic field H . The finite element program calculates the magnetic flux density for each element.

The program first calculates B in every finite element and then uses the core loss curve to determine the associated core loss. The overall core loss can be found at a particular instant as the sum of the elementary core losses for each element within the core by a static analysis. Since B could possibly peak at different times depending on the position of the rotor, more than one instants must be analyzed.

The core loss versus rotor position is shown in Fig 6.25.

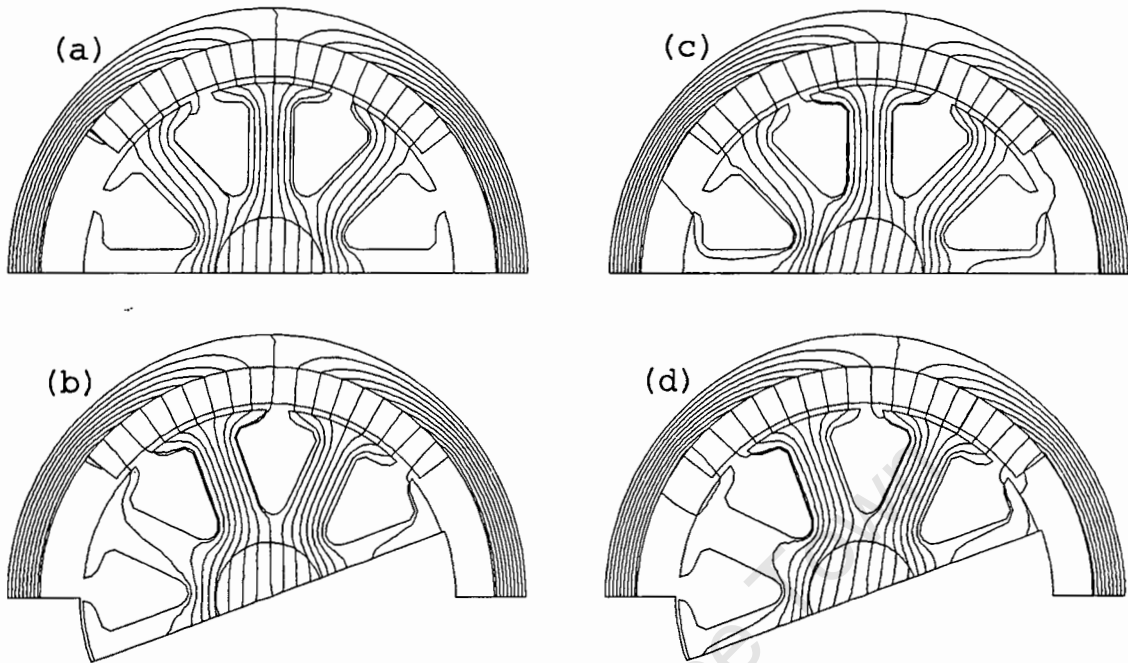


Figure 6.24: Flux plots used in the calculation of torque for 8 W motor. (a), (b) have armature current of 0.1 A, and (c) and (d) a armature current of 0.8 A. (a),(c) have $\theta = 0^\circ$ and (b),(d) have $\theta = 20^\circ$

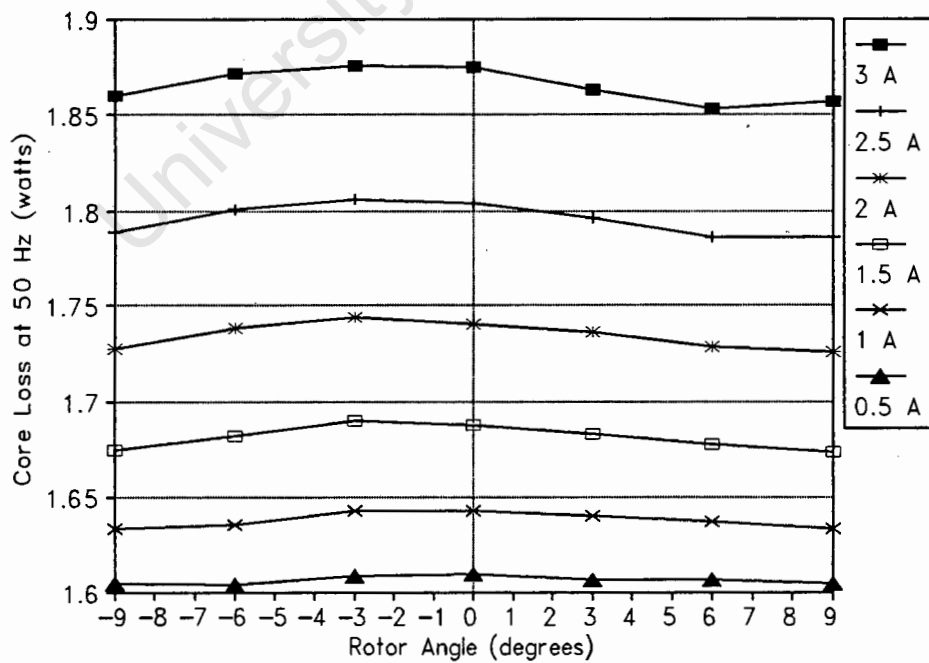


Figure 6.25: Core loss versus rotor position for 370 W motor

Chapter 7

Comparison of Transient Characteristics obtained from Classical Analysis, Finite Elements and Experiments

7.1 Classical Simulation

The transient characteristics of most interest are the start-up and rheostatic braking characteristics, especially the armature current and rotor speed functions versus speed.

The classical approach to the transient simulations have be done using two methods. The first being a Laplace solution to the transient equations and the second being a State Space solution. Both simulations were implemented using computer programs.

7.1.1 Laplace Solution

The Laplace simulation have been investigated due to its ability to calculate the transient performance at any instance in time without having to calculate previous time steps within the transient characteristic.

The computer program was written to step through the transient characteristic until the new steady state condition is reached, so that the results can be compared with the state space and finite element results.

Fig 7.2 shows the flow chart of the Laplace simulation program in summarized form. The error in the Laplace simulation due to the non-linearity of the initial equation will

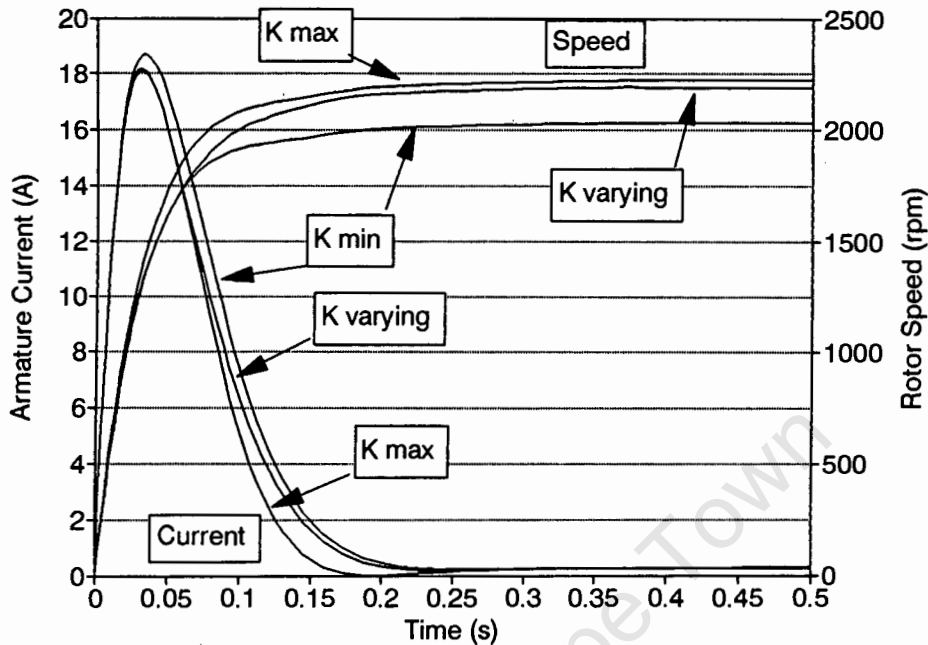


Figure 7.1: Start-up simulation using the extreme values for the machine constant k

differ depending on the motor model. The non-linearity is related to the varying machine constant k . The maximum error in the Laplace solution is thus in the range of the maximum and minimum k values. Fig 7.1 shows the Laplace solution using constant k values and thus showing the maximum error for this particular start-up characteristic.

7.1.2 State Space Solution

The state space characteristic have been used since it allows non-linear equations to be modelled easily. The only disadvantage of this method is that the accuracy of the solution is dependent on the number of time steps used and the initial time step increment should be calculated from the machine time constants, and not estimated. A very large time increment, i.e. as large as the electrical time constant, could result in the simulation being completely unstable and thus no steady state operating point would be reached. A starting time increment of approximately 10% of the electrical time constant is recommended.

Fig 7.3 shows the flow chart for the state space simulation as executed by the computer program. The error introduced by the linear step approximations is estimated by running the transient simulation for smaller time steps until the difference between the steady state rotor speed for the different time step simulations is less than 0.01%. This check

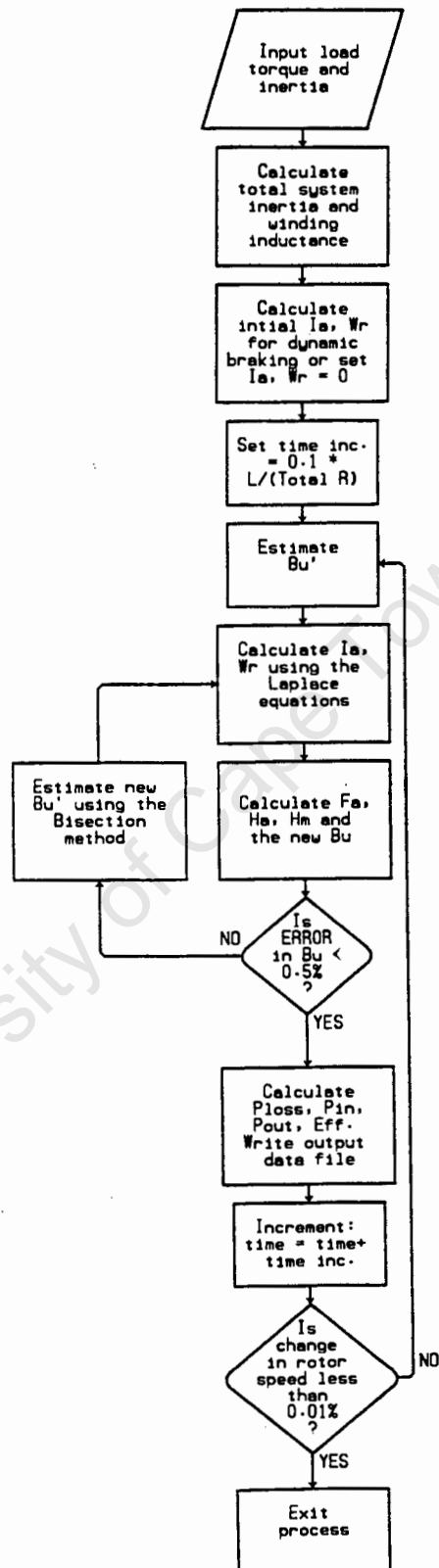


Figure 7.2: Flow chart showing the logical flow of the Laplace transient simulation

also ensures that the steady state values are reached in the same time or within a time step of each other.

7.2 Finite Element Simulation

The finite element transient simulations have been done with the assumption that the eddy current losses are negligible. This has been done due to the lengthy time considerations when doing a transient simulation using the finite element method, as discussed in Chapter 4. The armature current versus time results obtained have however be entered into a finite element transient simulation in an attempt to calculate any increases in eddy current losses in the rotor core.

The transient simulation can then be done using the state space method, as discussed in the classical simulation, except that the electromagnetic torque is obtained from a look up table of armature current versus torque created using the finite element simulation.

The simulation is set out as follows:

1. The finite element steady state simulation is run for a large number of armature current values up to the maximum possible starting current value.
2. A plot of armature current versus electromagnetic torque is build.
3. The initial I_a and ω_r values are input.
4. A state space approximation is used to simulate the transient performance, as discussed for the classical simulation. The machine constant can be obtained using the finite element results, in a look-up table, instead of the classical equivalent magnetic circuit.
5. The simulation is run until the new steady state conditions are reached.
6. The simulation is repeated for a smaller time step and the steady state results for the two simulations are compared to ensure that the step increment is small enough to obtain a reasonable accuracy, as discussed in the classical state space simulation.
7. The process is ended if the accuracy is sufficient else the simulation is repeated for a smaller time increment.

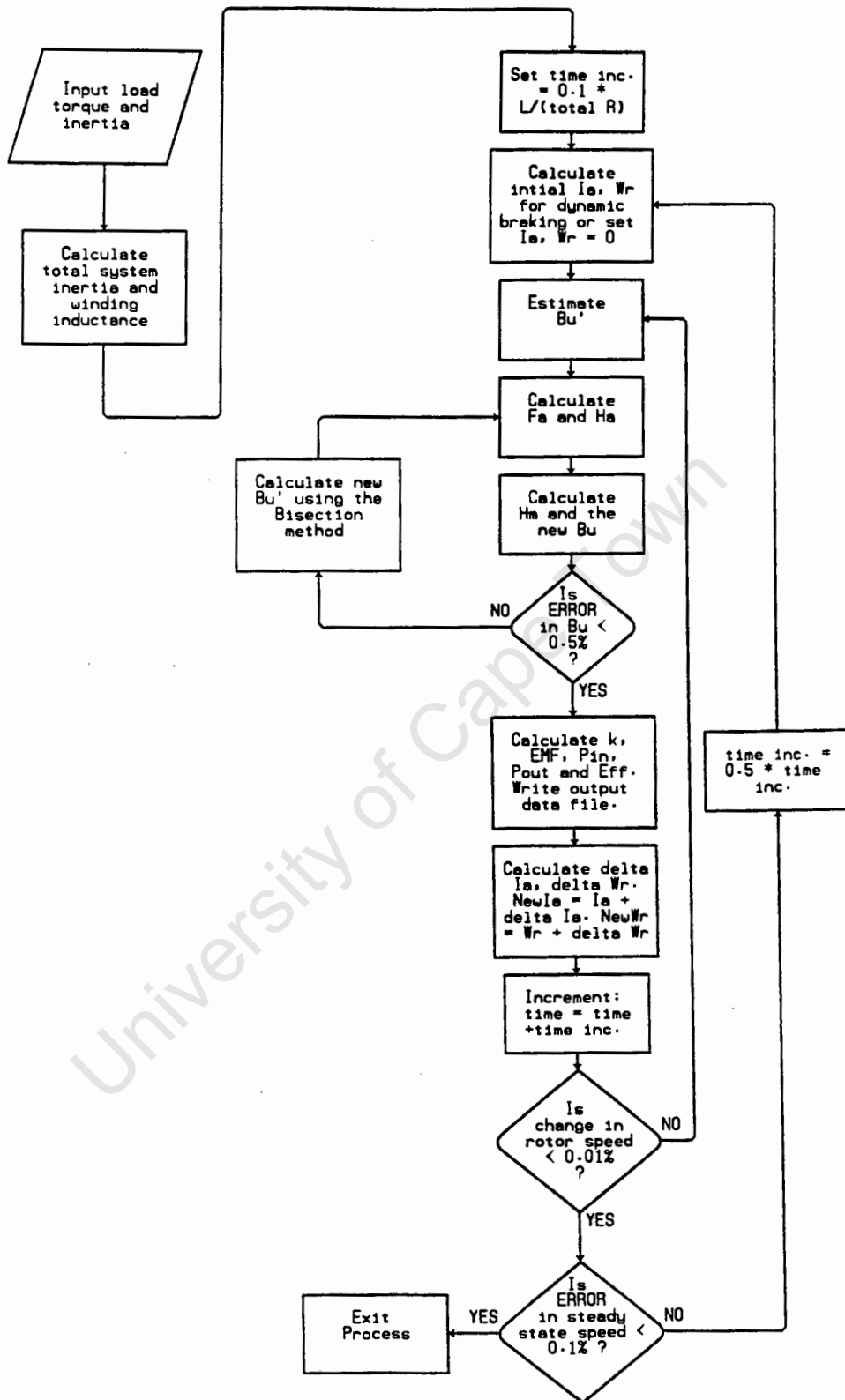


Figure 7.3: Flow chart showing the logical flow of the state space transient simulation

7.2.1 Transient finite element simulation

The armature current values obtained from the above simulation are entered in to the finite element program as the input. The simulation is then run as a true transient finite element simulation, including the eddy current effects in the rotor.

The problem with this simulation is that the main flux produced by the permanent magnets has to be setup in the model before the armature current input can be entered. This means that the first 56 steps of the simulation are used only to setup a steady main flux. Figs 7.4 show the changing flux as the armature current increases during the transient simulation. The core losses calculated from these models did not differ from the steady state core loss results. It was however noted that the equivalent conductivity of the laminated rotor core is difficult to calculate or approximate and tests on the laminations would have to be done, which is beyond the scope of this thesis and are needed before many results can be drawn from this model.

7.3 Results

The transient simulation has only been done for the 370 W dc permanent magnet motor.

The armature inductance has been calculated using two equations in the classical simulation and one method in the finite element simulation, as discussed in Chapter 4. The results from the respective calculations are shown in Table 7.1.

Table 7.1: Armature winding inductance results for 370 W motor

Finite Element (H)	Classical (H)	
	equ (4.4)	equ (4.5)
0.13365	0.11419	0.1145

The armature current and rotor speed are the only parameters used in the comparison, since they represent the most important considerations during any transient simulation. The maximum power losses in motor and the time constant of the motor can be calculated from these plots.

The results from the transient start-up performance for different load and voltage conditions are first shown and then the same is done for transient rheostatic braking.

The results for the start-up performance under different input voltages are shown in Figs 7.5, 7.6, 7.7, 7.8 and the results for the start-up performance with varying load but

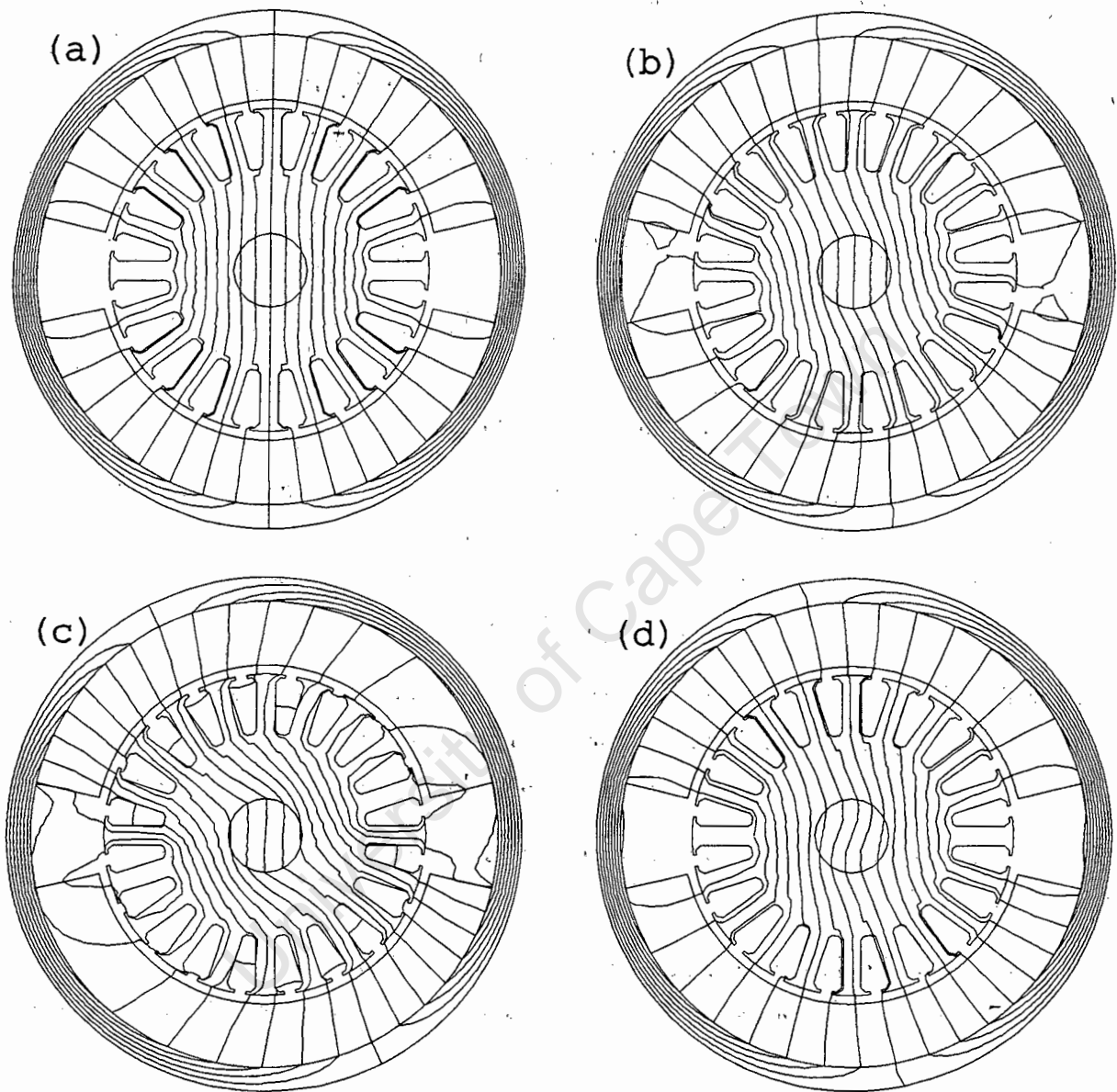


Figure 7.4: Flux plots for the start-up simulation in the 370 W motor with a load connected. (a) at time = 0 when voltage is applied, after setting up the permanent magnet. (b) 0.5 milliseconds after beginning the start-up simulation. (c) after 3.5 milliseconds and (d) 0.6 seconds after start of simulation (steady state is reached)

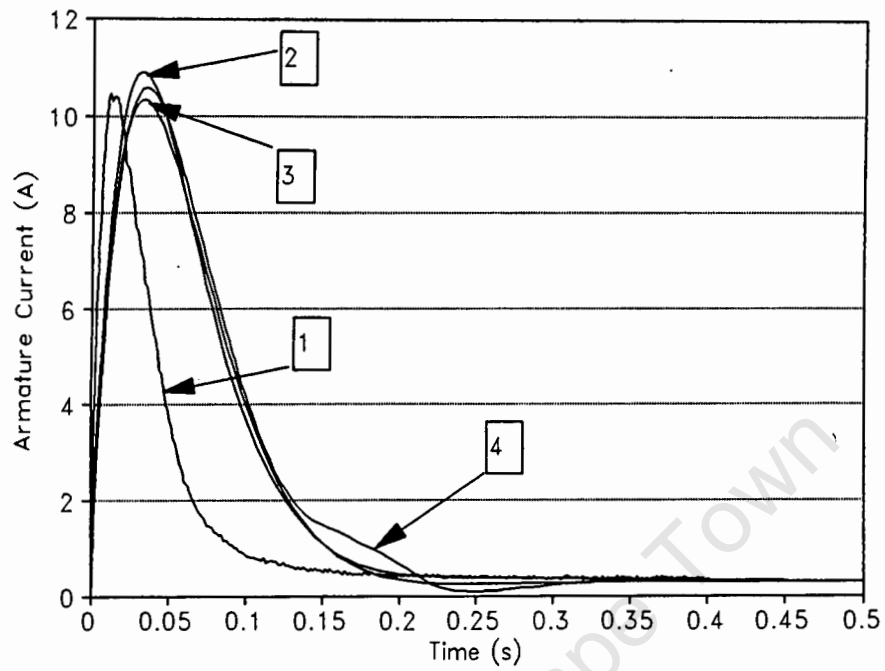


Figure 7.5: Input armature current versus time in start-up characteristic with 90 V input voltage and no load torque

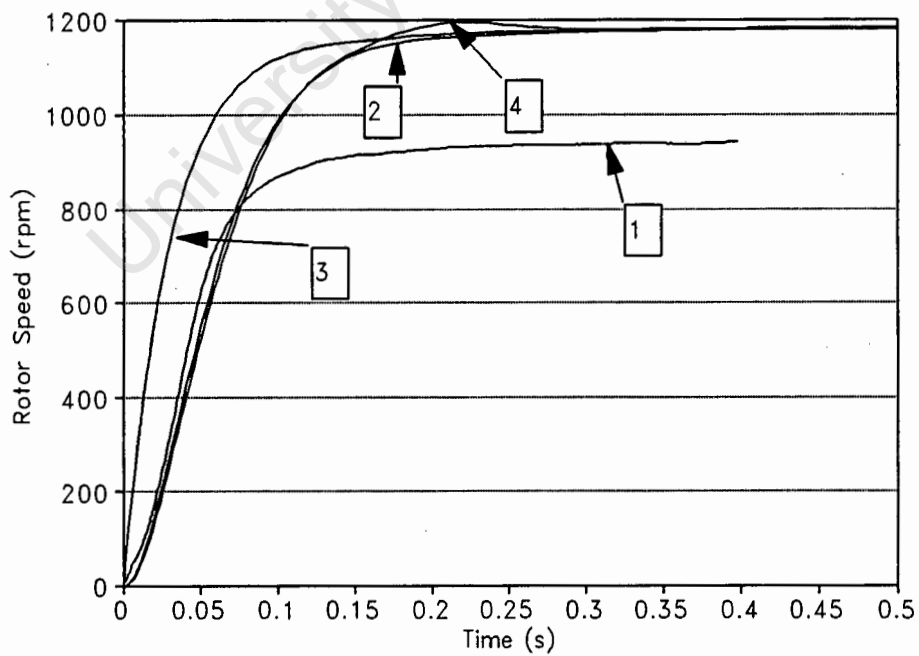


Figure 7.6: Rotor speed versus time in start-up characteristic with 90 V input voltage and no load torque

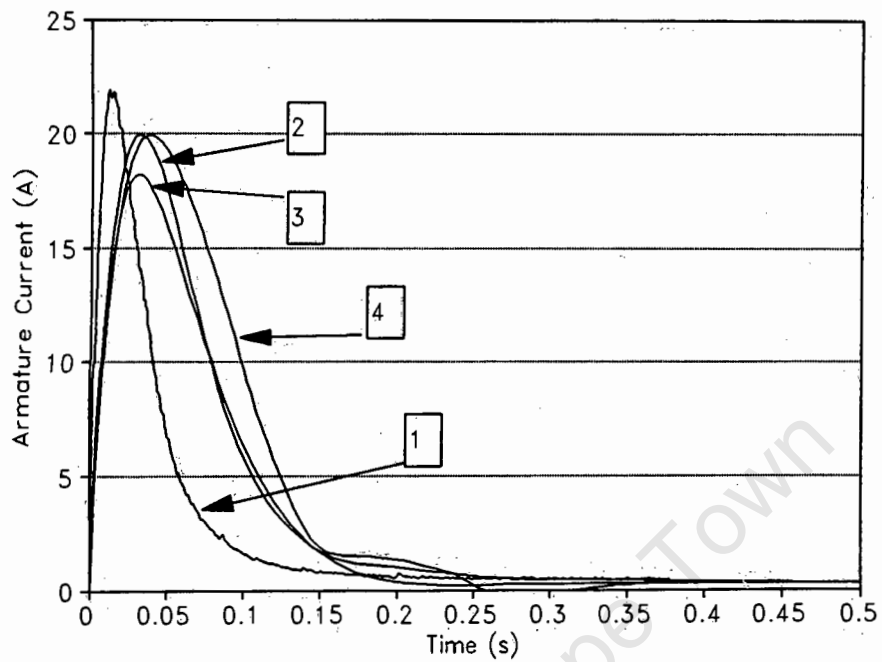


Figure 7.7: Input armature current versus time in start-up characteristic with 180 V input voltage and no load torque

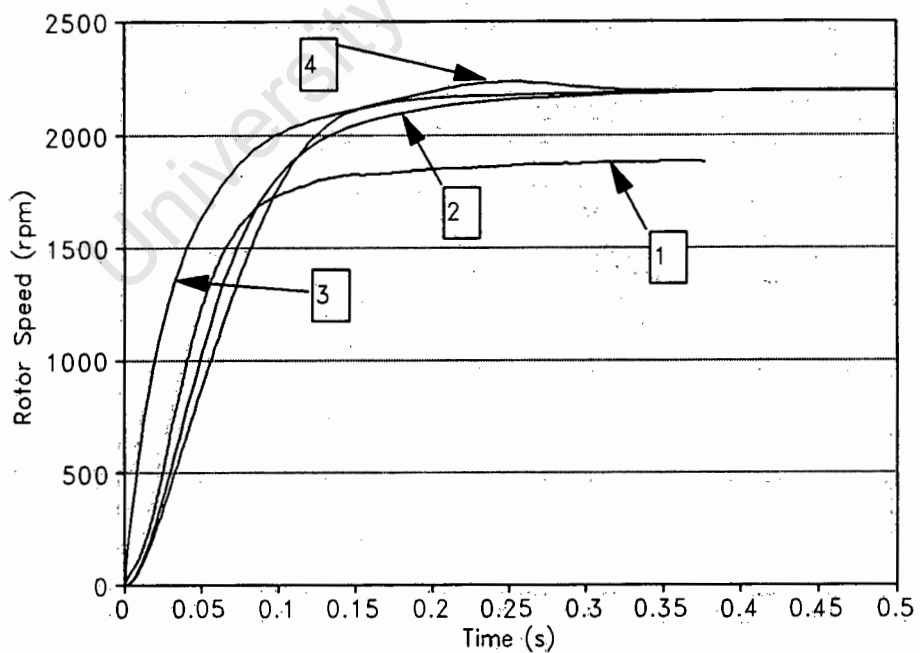


Figure 7.8: Rotor speed versus time in start-up characteristic with 180 V input voltage and no load torque

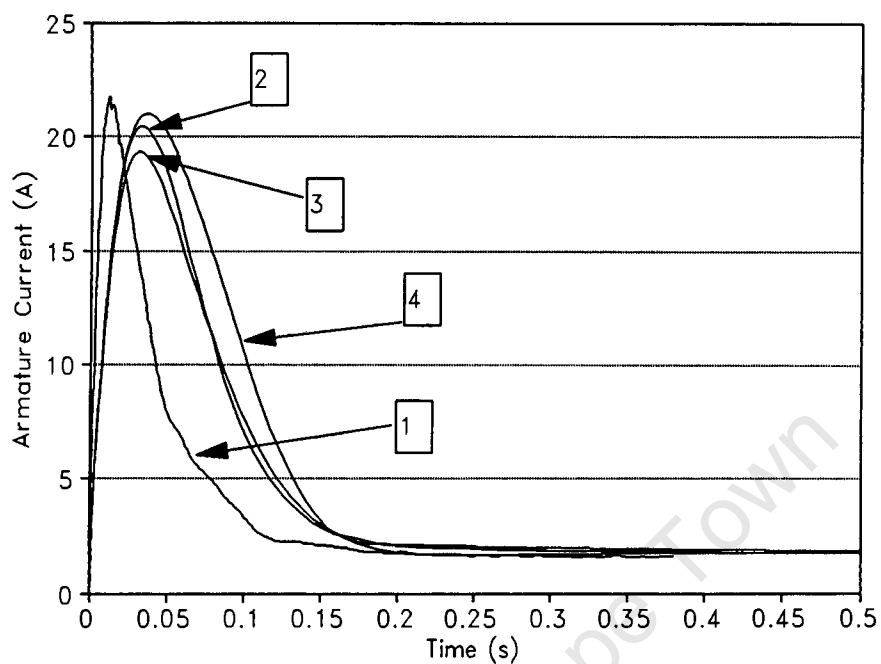


Figure 7.11: Input armature current versus time in start-up characteristic with 180 V input voltage and 1.164 Nm of load torque

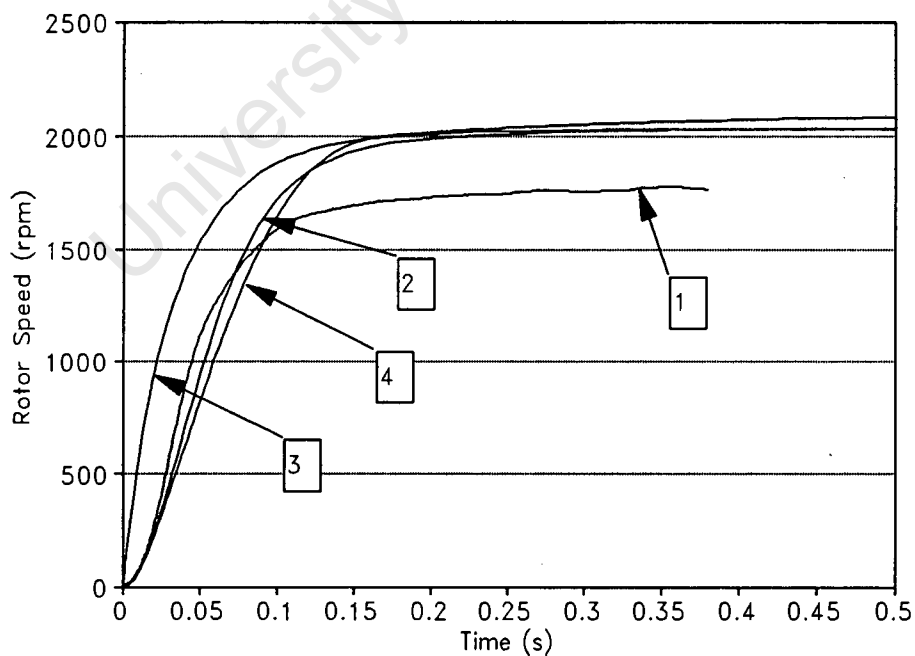


Figure 7.12: Rotor speed versus time in start-up characteristic with 180 V input voltage and 1.164 Nm of load torque

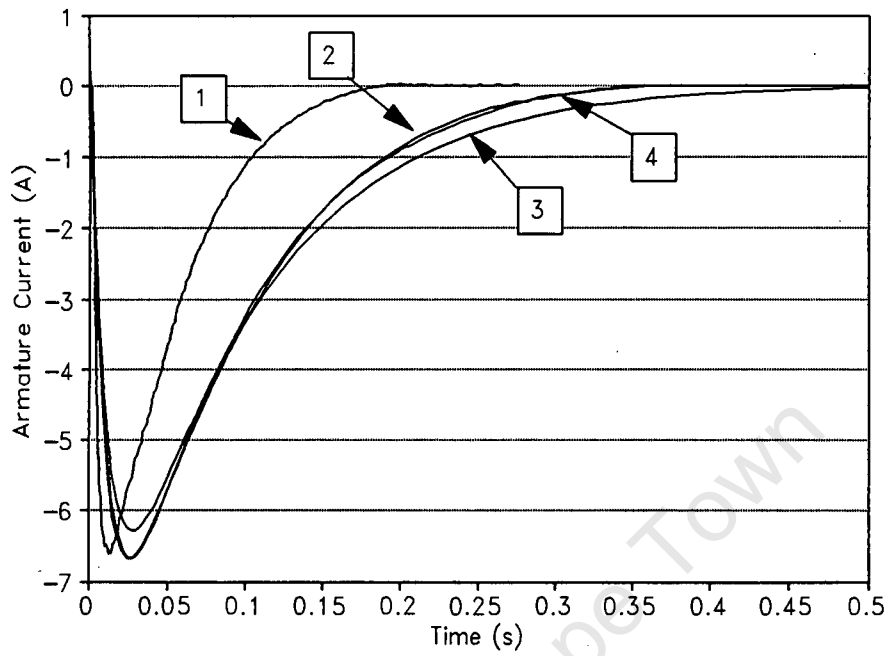


Figure 7.13: Input armature current versus time in rheostatic braking characteristic with 90 V input voltage and no load torque

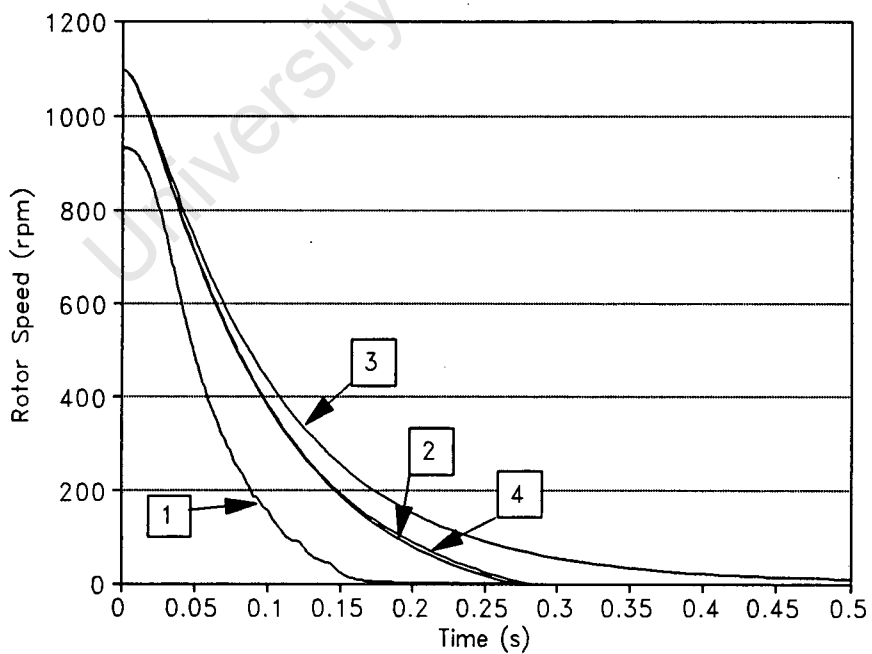


Figure 7.14: Rotor speed versus time in rheostatic braking characteristic with 90 V input voltage and no load torque

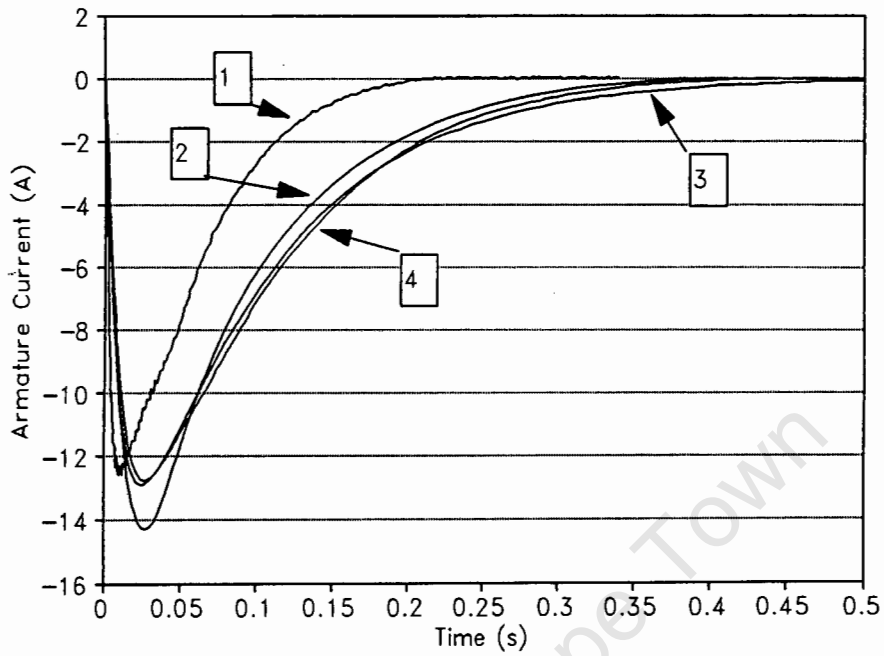


Figure 7.15: Input armature current versus time in rheostatic braking characteristic with 180 V input voltage and no load torque

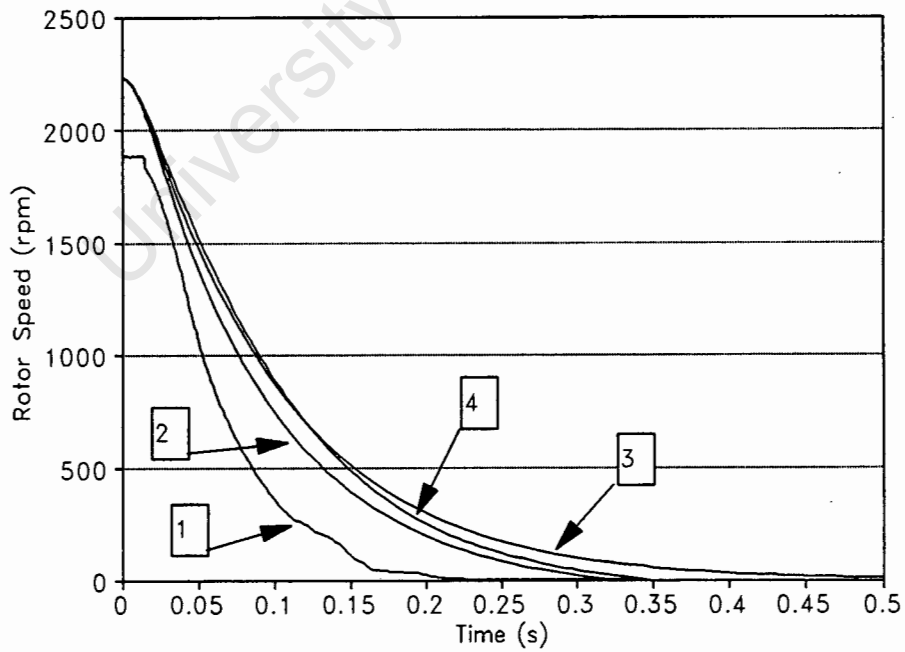


Figure 7.16: Rotor speed versus time in rheostatic braking characteristic with 180 V input voltage and no load torque

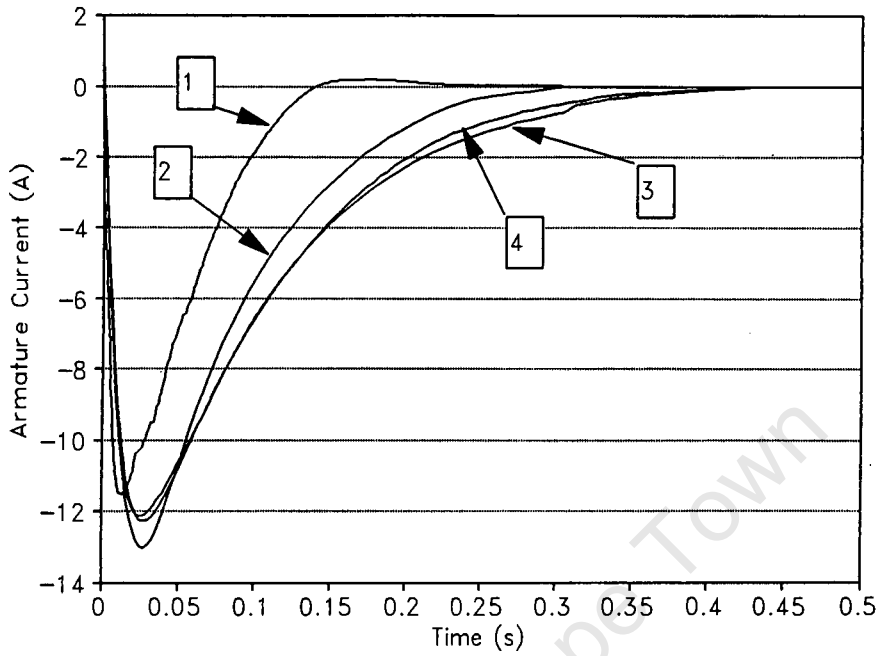


Figure 7.17: Input armature current versus time in rheostatic braking characteristic with 180 V input voltage and 0.56 Nm of load torque

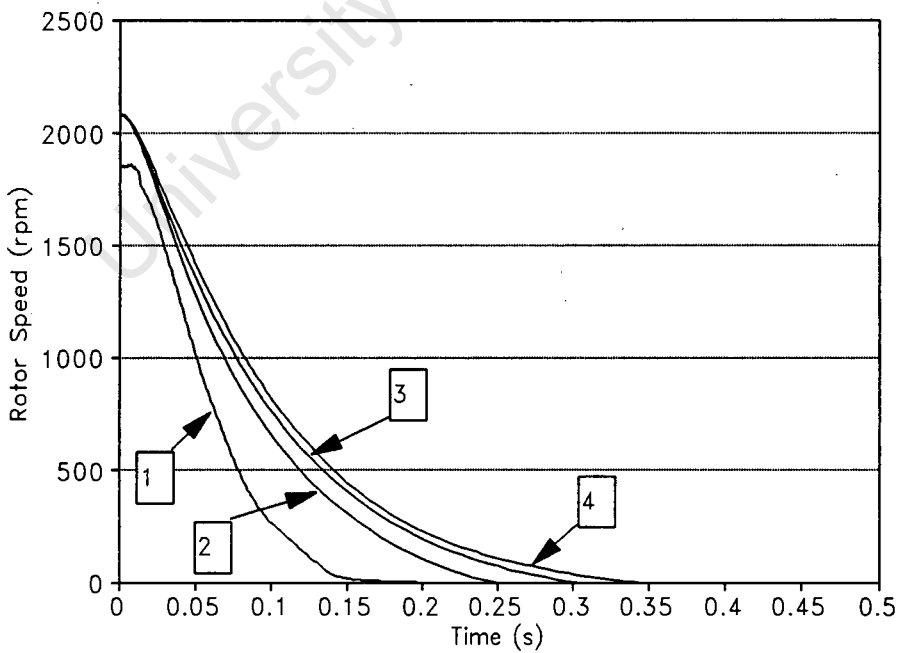


Figure 7.18: Rotor speed versus time in rheostatic braking characteristic with 180 V input voltage and 0.56 Nm of load torque

Chapter 8

Special Topics

8.1 Cogging Torque

The finite element method calculates the electromagnetic torque at one rotor position. To find the average torque produced by the motor a number of different rotor positions have to be modelled. The torque at the different rotor positions is called the cogging torque.

In dc motors the cogging torque is due to the varying relative position between the rotor teeth and the permanent magnet, thus producing flux pulsations and cogging torque. The fewer the rotor slots the greater the cogging effect. Cogging torque is particularly undesirable at low speeds, especially if a constant speed is to be maintained for a constant load condition.

The number of degrees of rotor movement needed to simulate, by the finite element simulation, the entire torque change depends on the number of rotor slots. The cogging torque versus rotor angle θ (Fig 8.1) is shown for a number of load conditions in Fig 8.2 for the 370 watt motor and in Fig 8.3 for the 8 watt motor.

It is evident that the cogging torque to average torque ratio is larger in the 8 W motor than in the 370 W motor. This is due to the fact that the 8 W motor has fewer rotor slots than the 370 W motor and thus the cogging effect is greater.

8.2 Overlap angle of permanent magnet

In the design of dc commutator permanent magnet motors one of the design criteria is the size of the segmental permanent magnets, in particular the overlap angle β of the magnet (Fig 8.1). The effect on the performance and cogging torque of small dc motors due to a

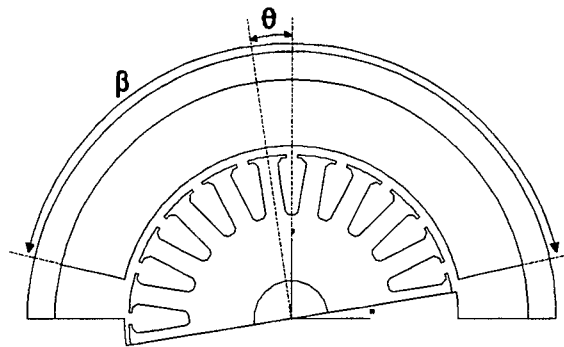


Figure 8.1: Cross section of a dc commutator motor showing the rotor angle θ and the overlap angle β .

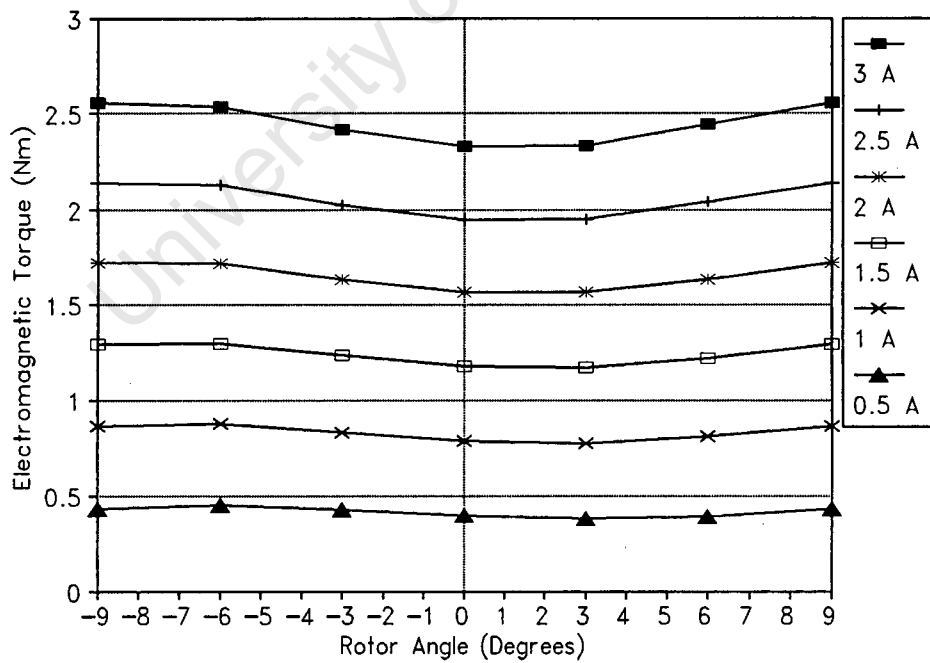


Figure 8.2: Cogging Torque versus rotor angle θ for different loads in the 370 W motor

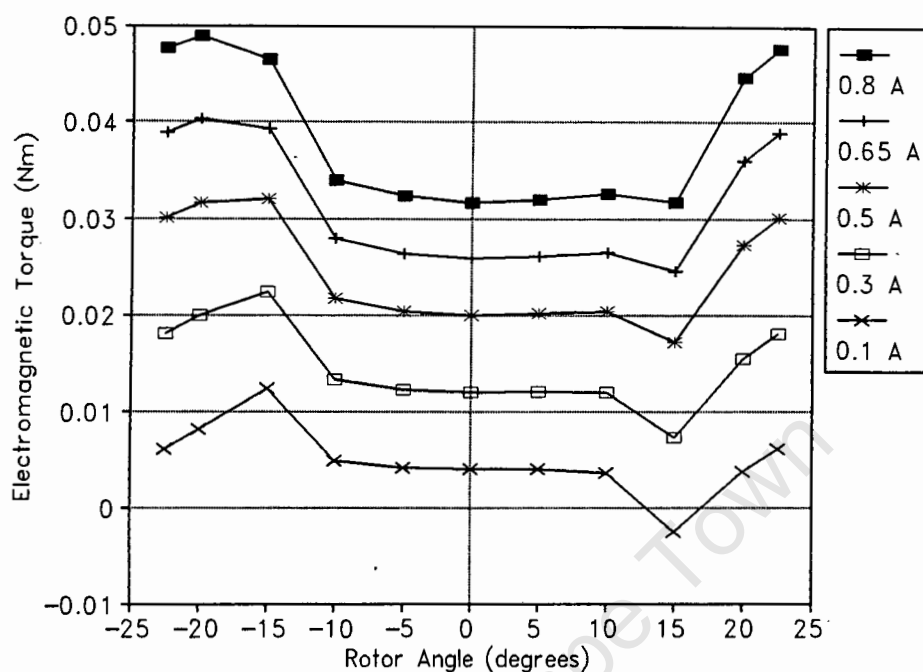


Figure 8.3: Cogging Torque versus rotor angle θ for different loads in the 8 W motor

varying overlap angle is thus investigated.

The cogging torque has been calculated using the finite element method for a constant output shaft torque. This was done by obtaining the performance curves for the different overlap angles and then reading off the armature current that corresponds to the rated output torque. The effect on cogging torque due to a change in the overlap angle is shown in Figs 8.4, 8.5 for the 370 watt and 8 watt motors respectively. As is expected the cogging torque versus rotor angle changes as the ratio of overlap angle to tooth pitch changes. The magnitude of the cogging torque, in the case of the 8 watt motor, increases as the overlap angle decreases due to the greater effect the number of rotor slots will have on the cogging torque.

The effect of varying the overlap angle on the performance of the motors was calculated using the classical analysis, as well as the finite element method. The performance of the motors for a varying overlap angle are shown in Figs 8.6, 8.7. The results were taken at rated output torque for the two motors, i.e. 2 Nm for the 370 W motor and 0.027 Nm for the 8 W motor. Only the rotor speed and efficiency versus overlap angle are shown in the figures since the armature current and output power follow similar curves.

Figs 8.6, 8.7 show that as the size of the magnets increase the efficiency improves and the rotor speed generally decreases. The results from the classical simulation show a

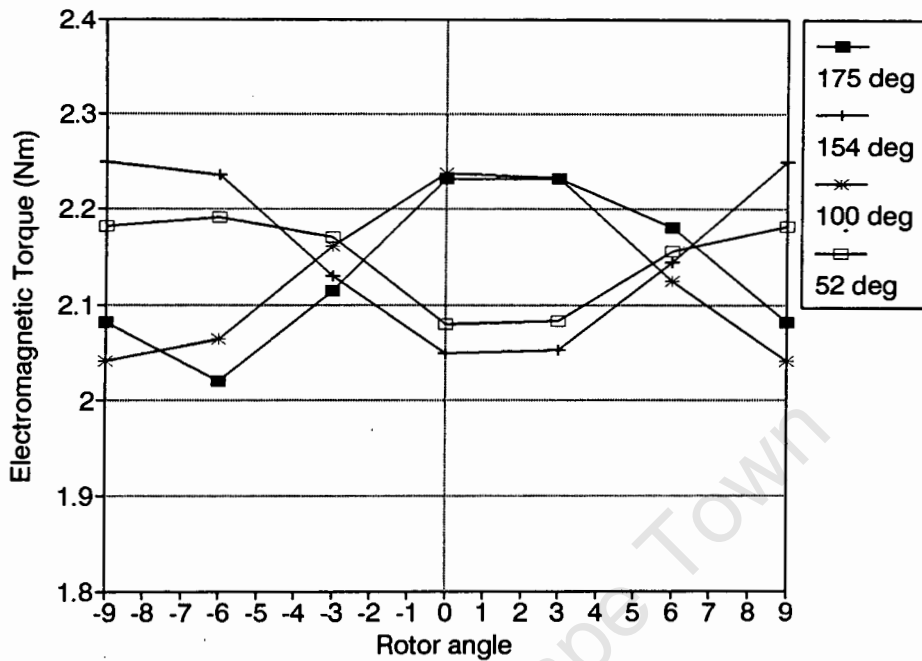


Figure 8.4: Cogging Torque versus rotor angle θ for four different overlap angles β , at a constant output torque of 2 Nm, in the 370 W motor

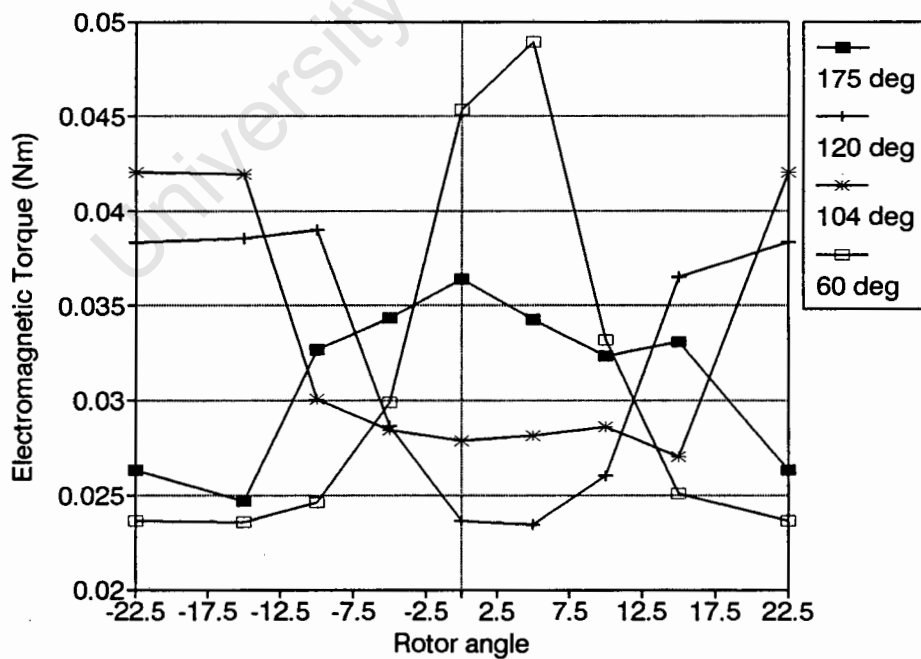


Figure 8.5: Cogging Torque versus rotor angle θ for four different overlap angles β , at a constant output torque of 0.027 Nm, in the 8 W motor

definite optimal operating point in terms of efficiency and rotor speed.

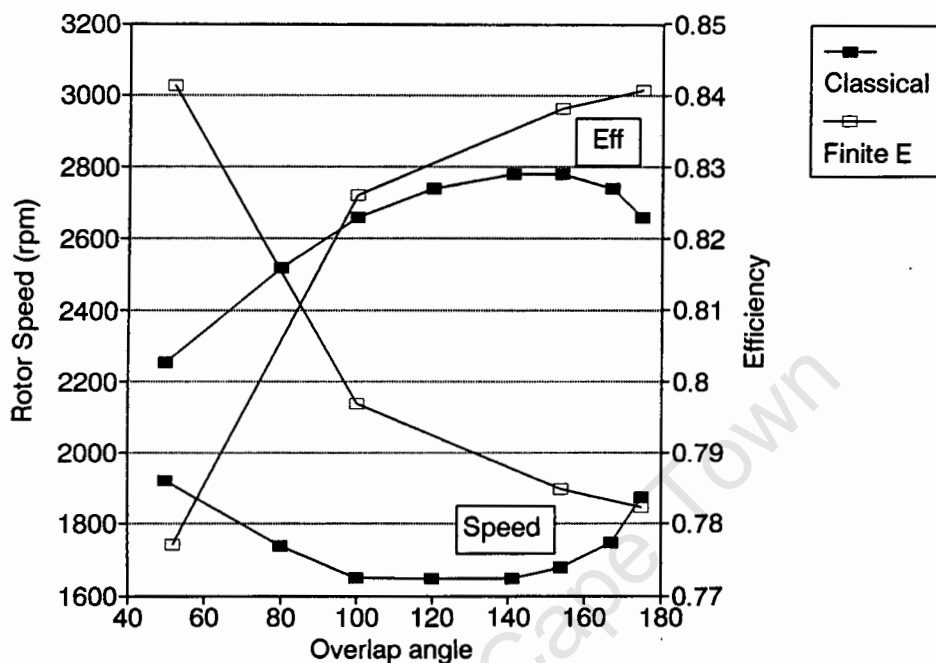


Figure 8.6: Rotor speed and Efficiency versus overlap angle β , at a constant output torque of 2 Nm, in the 370 W motor

8.3 Unsymmetrical permanent magnet positioning

In the manufacture of dc permanent magnet commutator motors, the segmental magnets are generally glued or clamped into position [16]. This can lead to inaccurate positioning of the magnets and thus to an asymmetrical magnetic circuit. It is thus of interest to manufactures to obtain tolerances of these inaccuracies with relation to the motors performance and the forces produced on the shaft due to the imbalanced attraction of the rotor by the magnets.

Due to the asymmetrical nature of this problem classical analysis techniques are not suitable for this type of calculation, but the finite element method is an ideal method since it can model the entire magnetic circuit.

The motor used in this simulation is the 370 W dc permanent magnet commutator motor. The motor had to be modelled as a whole in the finite element simulation. The permanent magnets were simulated using sheet current equivalents and only specific boundary conditions were used around the edges of the model. The Maxwell stress tensor

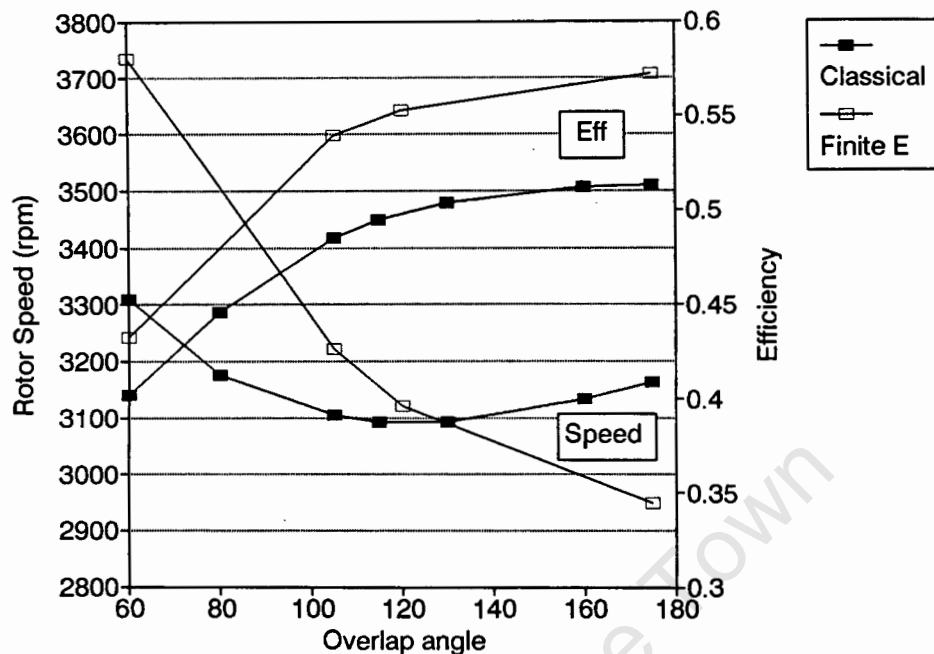


Figure 8.7: Rotor speed and Efficiency versus overlap angle β , at a constant output torque of 0.027 Nm, in the 8 W motor

method was used for calculating the electromagnetic torque produced by the motor and also the normal force between the rotor and the permanent magnets. Linear commutation with no shifting of the brushes is assumed in this model.

In the model the asymmetry was created moving only one permanent magnet, by an angle α as shown in Fig 8.8.

8.3.1 Magnetomotive force

Fig 8.9 shows the effect on the MMF (stator and armature reaction MMF) for different directions of rotor rotation in the asymmetrical conditions [17].

The resultant MMF is either increased or decreased as can be seen in Fig 8.9. It can thus be shown that the torque is increased if the direction of rotation is in the same direction as to the movement of the magnet and the torque will decrease if the magnet is shifted in the opposite direction [23].

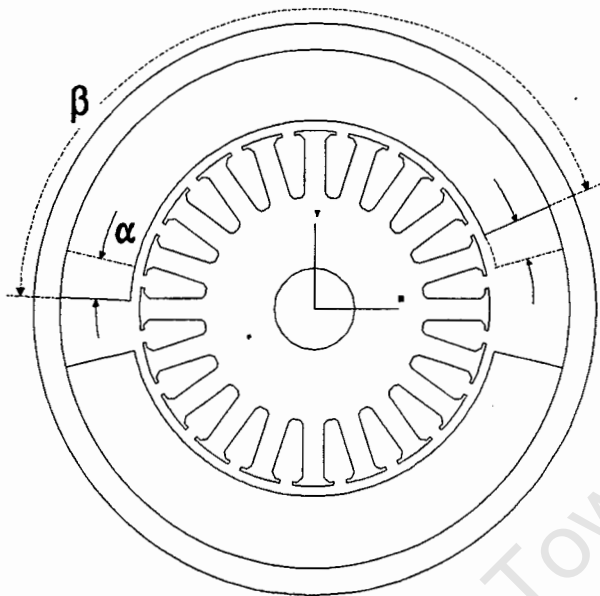


Figure 8.8: Cross section of a dc commutator motor showing overlap angle of the permanent magnet β and permanent magnet shift angle α .

8.3.2 Asymmetry of magnetic circuit and performance characteristics

The performance of the motor was modelled for different shifts in one magnet by an angle α (Fig 8.8). In the manufacture of permanent magnet motors the error in placing the magnets is usually $\alpha < 2^\circ$. Exaggerated magnet shifts of $\alpha = 3^\circ$ and $\alpha = 10.5^\circ$ were assumed, to simulate the extreme cases of magnet misalignment.

The performance of the motor is dependent on the direction of rotation of the rotor with respect to the direction of movement of the magnet.

The reduction in performance as the magnet shift increases, in the opposite direction to that of the rotor rotation, can be seen from the characteristics in Figs 8.10 and 8.11.

8.3.3 Force distribution

The unsymmetrical magnets produce a net force on the rotor shaft. This force produces greater stress on the motors bearings and leads to greater vibration of the motor system. Fig 8.12 shows the normal force on the rotor of a permanent magnet motor, in the symmetrical case and with a magnet shift of 10.5° , running at a constant load current.

The net magnetic attraction force for a load of 3 A is shown in Table 8.1. The normal

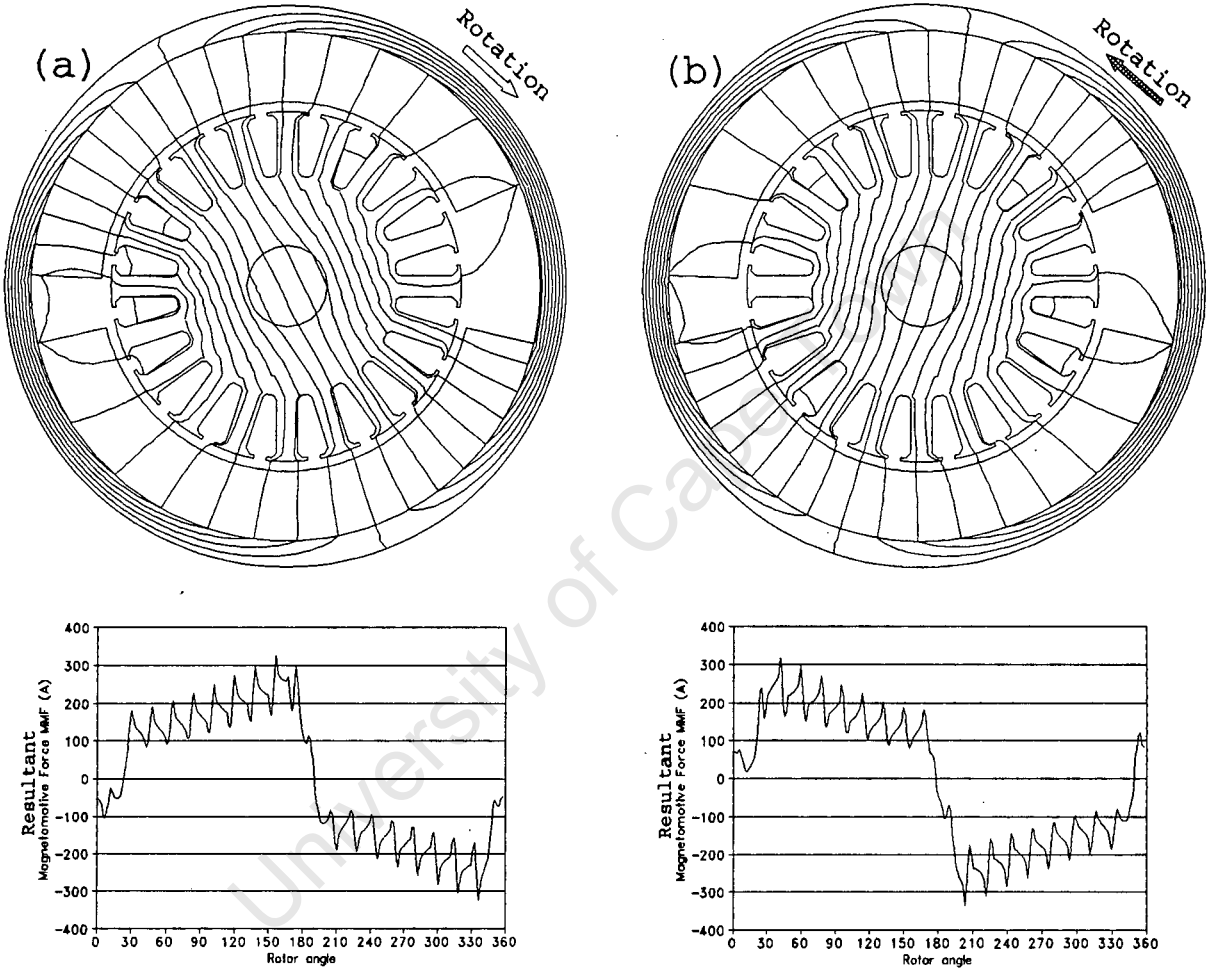


Figure 8.9: Flux plots and resultant MMF distributions for two different directions of rotor rotation with one magnet shifted 10.5°.

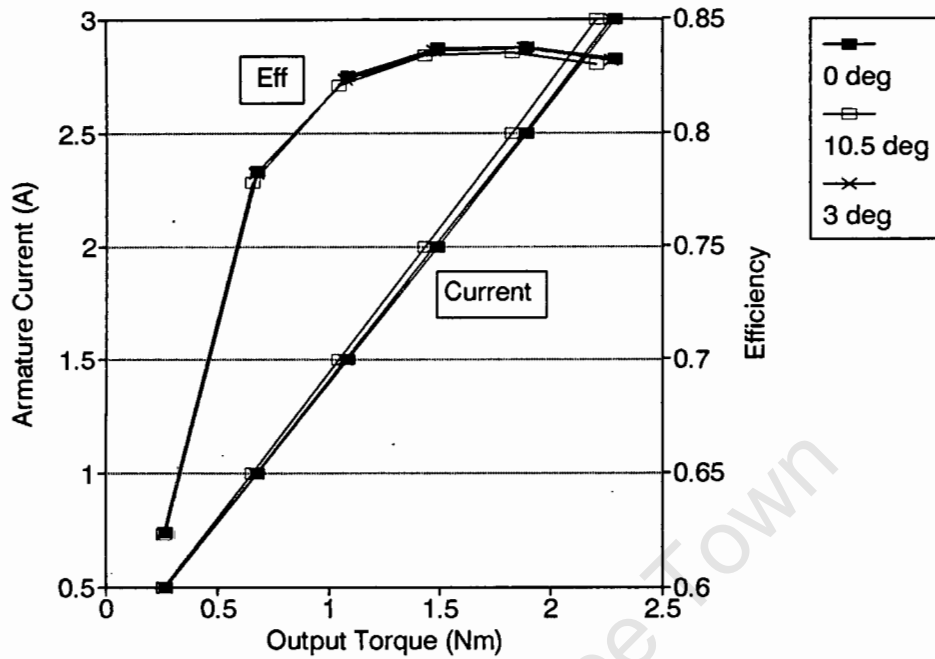


Figure 8.10: Armature current and efficiency versus output torque for three different values of magnet shift α , when the rotor rotates in the opposite direction to the magnet shift.

force is calculated using the Maxwell stress tensor equation for a normal force within a airgap element [33].

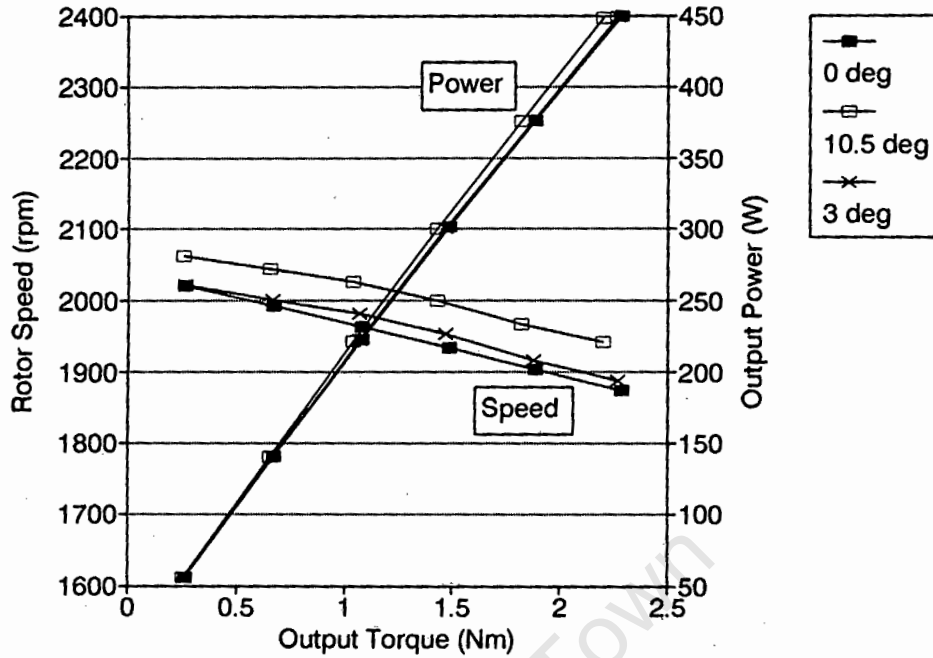


Figure 8.11: Rotor speed and Output power versus Output torque for three different values of magnet shift, when the rotor rotates in the opposite direction to the magnet shift α .

Table 8.1: Attraction force of asymmetrical magnetic circuit in 370 W motor with 3 A of load current.

Rotor angle	Net attraction force	
	Magnitude (N)	Angle
-9°	44.89629	188.6705°
-6°	43.96645	187.9772°
-3°	41.37521	188.4543°
0°	41.34293	189.7211°
3°	42.30593	190.5453°
6°	43.67182	189.8705°
9°	44.89629	188.6705°

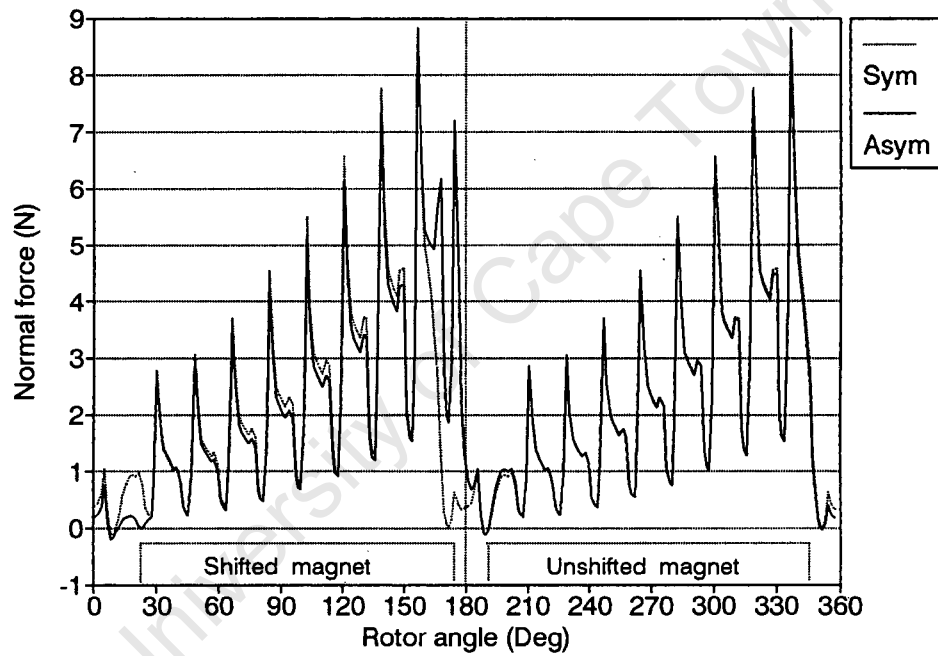


Figure 8.12: Normal force between the rotor and the magnets versus rotor angle for a symmetrical magnetic circuit and for a magnet shift of 10.5° .

Chapter 9

Conclusions

9.1 Steady State

The steady state results showed a good correlation between the experimental data and the simulations. The simulations showed the greatest error in the calculation of rotor speed, especially in the 8 W motor. This error in the speed calculation is due to the calculation of rotational losses which were calculated using the same method in the classical and the finite element method. The rotational losses are an important percentage of the total losses in small dc motors and thus effect the simulations greatly.

9.1.1 Classical simulation

The classical simulation gave good results for both motors. The classical simulation is however a one dimensional method and thus the results for the 8 W motor were not as good as the ones for the 370 W motor, since the number of rotor slots effect the simulation and thus the higher the number of slots the better the simulation results.

The classical simulation produced its results very quickly and for a range of output powers from zero up to 10% above the rated output power. This meant that in less than a minute the full performance characteristics of a motor can be found.

9.1.2 Finite element simulation

Building the finite element model is a complex and time consuming procedure. Due to the fact that the torque at one rotor position is not sufficient in calculating the motors performance, a number of different models, with a change in rotor position have to be

build. If the motors general performance is needed (average torque) there is no quick solution and the average torque has to be found from the cogging torque. Calculating the characteristic performance of a motor using the finite element method is thus every time consuming.

The use of a two dimensional model in the finite element method means that the equivalent thickness of the stator yoke has to be calculated. The tests showed that the torque calculated from the finite element method is very sensitive to the stator thickness. The method of estimating the equivalent stator yoke area worked well in the modelling of the small motors but the use of a three dimensional method is seen as a more accurate method.

The Maxwell stress tensor area integral method of calculating electromagnetic torque was shown to be the easiest method to implement and as accurate as the co-energy exact derivative method. The results on the best method of calculating torque cannot be generalized to all finite element problems, but in terms of dc motors the Maxwell stress tensor area integral is the most efficient in terms of accuracy and implementation time. The co-energy finite difference method was shown to be inferior to the other methods not only in terms of accuracy, due to rounding-off errors, but also in terms of execution time since two finite element models have to be build.

9.2 Transient

9.2.1 Classical simulation

The classical simulation was done using two methods of calculating the transient responses to both start-up and braking simulations.

The Laplace simulation was attempted since it would be able to give the motors performance at any point in time without having to calculate the whole transient sequence. There is however an added error in the Laplace simulation due to the non-linearity of the system, varying machine constant, which the Laplace solution ignores. Although this error was not large in the motor simulated, due to the limited variation in the machine constant, the error could in general make the simulation unreliable.

The state space transient simulation is easy to implement but has the disadvantage that it has to run through the whole transient motion. The time step taken also effects the accuracy of the simulation, but since the simulation is easy to implement a sufficiently small time step can be taken and the results are still obtained in seconds. This makes the

state space simulation a better solution than the Laplace simulation.

9.2.2 Finite element simulation

The finite element simulation package only allows armature current as a input load. This means that unless the armature current versus time function is known the transient simulation using the finite element method becomes unfeasible. The method can solve transient problems where the initial armature current is known, but if the armature current at each new step in the transient simulation has to be calculated separately from the finite element package the transient simulation would take a few weeks to complete.

The solution to the lengthy time problems with a transient simulation in the finite element method is to build a plot of electromagnetic torque versus armature current using steady state finite element models. This neglects the eddy current losses in the lamination and uses a state space approximation to calculate the transient response. Once the current-torque plot is calculated any transient response can be simulated just using the plot as a look-up table.

9.3 Special topics

Problems such as cogging torque, the size of the permanent magnets overlap angle and the asymmetry in the magnetic circuit are very important from a practical point of view. The design engineer and manufacture need this type of information to help estimate the efficiency, noise level and vibration of the motor [34].

The results from the cogging torque showed that the fewer rotor slots the motor has the greater the cogging torque in proportion to its average torque, assuming there is no skewing of the rotor.

The overlap angle of the segmental permanent magnet has been shown to play a important role in the motors characteristic performance. The optimal overlap angle was shown to be very close to the actual overlap angle chosen by the motor designers. The classical analysis showed a definite optimal overlap angle while the finite element analysis indicated that the larger the overlap angle the higher the efficiency. The finite element method did however show that the effect of increasing the overlap angle above a certain angle improved the performance proportionally less, usually the actual overlap angle of the motor.

The asymmetry of only one motor has been simulated and it would need a number of

different motor sizes to be tested before any generalized conclusions can be drawn. The following conclusions can however be made about this particular motor:

1. The performance of the permanent magnet motor was not effected in any significant manure due to the asymmetry of the stator magnetic poles. The variation of the calculated armature current, efficiency and rotor speed showed a maximum change of 3%.
2. The torque produced can either be increased or decreased depending on the direction of rotation. The torque will in general improve if the magnets are moved in the direction of rotation.
3. The asymmetry of the magnetic circuit contributes to the imbalanced magnetic pull on the rotor shaft.
4. The force produced by the imbalanced magnetic pull is in the same direction as the magnet movement. This net force can lead to unwanted noise and increased wear of bearings.

Chapter 10

Recommendations

10.1 Future development in this field

The recommendations that can be made about future development in the field of small permanent magnet motor design and analysis are:

1. The rotational losses in small motors make up a large proportion of the total losses in the system. It is thus recommended that improved methods of calculating rotational losses are developed for use in the classical and finite element simulations.
2. The errors in simulating PM dc motors using the classical method increased with a decrease in the number of rotor slots. A discretized classical simulation taking into account the different magnetic circuit parts in the motor would improve this limitation.
3. The integration of the classical machine theory into the finite element simulation package to obtain a totally integrated transient simulation package, as proposed briefly in Chapter 7.

10.2 The relevance to South African Industry

The fact that no manufacture in South Africa is producing any permanent magnet motors means that the development of this industry must start with the design. The recommendations made to industry from this research are:

1. The implementation of the classical simulation into an expert system for general design purposes and to do any initial designs on.

2. The use of the finite element to check the magnetic circuit of the design in an attempt to optimize the magnetic circuit in reducing the amount of material used in low magnetic flux density areas and increasing the material quantity where the material is saturated. The optimization of the slot shape to reduce leakage flux can also be done using the finite element method.
3. It is recommended that the transient simulations be done using the classical method, until the finite element method is integrated into the classical method, and that the finite element method only be used for analyzing the eddy currents from the classical simulation results.

University of Cape Town

Bibliography

- [1] Z. Ren B. Davat and M. Lajoie-Mazenc. "The movement in field modeling". *IEEE Transactions on Magnetics*, Mag-21(6):2296–2298, 1985.
- [2] N. Boules. "Design optimization of permanent magnet dc motors". *IEEE Transactions on Industrial Applications*, 26(4):785–792, 1990.
- [3] J. R. Brauer. *What every Engineer should know about Finite Element Analysis*. Marcel Dekker, New York, 1988.
- [4] J. R. Brauer, E. A. Aronson, K. G. McCaughey, and W. N. Sullivan. "Three dimensional finite element calculation of Saturable Magnetic fluxes and Torque of an Actuator". *IEEE Transactions on Magnetics*, MAG-24(1):455–458, 1988.
- [5] B. Brunelli, D. Casadei, U. Reggiani, and G. Serra. "Transient and Steady State behaviour of Solid rotor induction machines". *IEEE Transactions on Magnetics*, MAG-19(6):2650–2654, 1983.
- [6] L. Chang, A. R. Eastham, and G. E. Dawson. "Permanent Magnet Synchronous Motor: Finite Element Torque Calculations". In *IEEE (I.A.S.) Industry Applications Society Annual Meeting*, volume 1, pages 69–73, 1989.
- [7] L. Chang, T. R. Eastham, and G. E. Dawson. "Permanent Magnet Synchronous Motor Modelling: Finite Element and Analytical Approaches". In *International Conference on the Evolution and Modern Aspects of Synchronous Machines*, volume 3, pages 1157–1162, 1991.
- [8] M. V. K. Chari and P. P. Silvester. *Finite Elements in Electrical and Magnetic Field Problems*. John Wiley and sons, Norwich, 1984.

- [9] J. L. Coulomb and G. Meunier. "Finite Element Implementation of Virtual Work Principle for Magnetic or Electric Force and Torque Computation". *IEEE Transactions on Magnetics*, Mag-20(5):1894–1896, 1984.
- [10] F. A. Fouad, T. W. Nehl, and N. A. Demerdash. "Permanent magnet modeling for use in vector potential finite element analysis in electrical machinery". *IEEE Transactions on Magnetics*, MAG-17(6):3002–3004, 1981.
- [11] J. F. Gieras. "Performance calculation for small DC motors with segmental permanent magnets". *Trans. of the SA IEE*, 82(1):14–21, 1991.
- [12] Z. Gogolewski and W. Gabrys. *DC Current Machines (in Polish)*. PWT, Warsaw, 1960.
- [13] D. Halliday and R. Resnick. *Fundamentals of Physics*. John Wiley and Sons, United States of America, 2nd edition, 1986.
- [14] K. H. Huebner. *The Finite Element Method for engineers*. John Wiley and Sons, United States of America, 1975.
- [15] M. K. Jamil and N. A. Demerdash. "Effects of chopper control on core losses of permanent magnet dc motors". *IEEE Transactions on Magnetics*, MAG-25(5):3572–3574, 1989.
- [16] T. Kenjo and S. Nagamari. *Permanent magnet and brushless dc motors*. Oxford University Press, New York, 1985.
- [17] M. Kostenko and L. Piotrovsky. *Electrical Machines*, volume 2. Mir Publishers, Moscow, 1974.
- [18] J. D. Kraus. *Electromagnetics*. McGraw-Hill Book company, Republic of Singapore, 1985.
- [19] M. Liwschitz-Garik and C. C. Whipple. *Electric Machinery*. D van Nostrand company Inc, United States of America, 3rd ed edition, 1947.
- [20] M. Marinescu and N. Marinescu. "Numerical Computation of Torque in Permanent Magnet Motors". *IEEE Transactions on Magnetics*, Mag-24(1):463–466, 1988.
- [21] L. W. Matsch. *Electromagnetic and Electromechanical Machines*. Harper and Row Publishers, New York, 2nd ed edition, 1977.

- [22] J. Mizia, K. Adamiak, A. R. Eastham, and G. E. Dawson. "Finite Element Force Calculation: Comparison of methods for Electric Machines". *IEEE Transactions on Magnetism*, Mag-24(1):447-450, 1988.
- [23] F. Odor and A. Mohr. "Two-component magnets for dc motors". *IEEE Transactions on Magnetism*, Mag-13(5):1161-1162, 1977.
- [24] S. F. Philport. *Fractional Horse Power Motors*. Jarrold and Sons, Ltd, Great Britain, Norwich, 1951.
- [25] P. G. Potter and G. K. Cambrell. "A combined Finite Element and Loop analysis for nonlinearly interacting magnetic fields and circuits". *IEEE Transactions on Magnetism*, Mag-19(6):2352-2355, 1983.
- [26] Tang Renyuan, Hu Yan, Lu Zhanhong, and Yang Shiyou. "Computation of Transient Electromagnetic Torque in a Turbogenerator under the cases of different Sudden Short Circuits". *IEEE Transactions on Magnetism*, Mag-26(2):1042-1045, 1990.
- [27] G. E. Roberts and H. Kaufman. *Table of Laplace Transforms*. W. B. Saunders company, United States of America, 1966.
- [28] M. G. Say. *The Performance and Design of Alternating Current Machines*. Sir Isaac Pitman and Sons, Ltd, Great Britain, London, 1949.
- [29] M. G. Say and E. O. Taylor. *Direct Current Machines*. The Pitman Press, Great Britain, Bath, 1980.
- [30] P. P. Silvester and M. V. Chari. "Finite Element Solution of Saturable Magnetic Field Problems". *IEEE Transactions on Power Apparatus and Systems*, PAS-89(7):1642-1651, 1970.
- [31] P. P. Silvester and R. L. Ferrari. *Finite Elements for Electrical Engineers*. Cambridge university press, Great Britain, Cambridge, 1983.
- [32] S. C. Tandon, A. F. Armor, and M. V. Chari. "Nonlinear Transient finite element field computation for electrical machines and devices". *IEEE Transactions on Power Apparatus and Systems*, PAS-102(5):1089-1095, 1983.
- [33] T. Tarnhuvud and K. Reichert. "Accuracy problems of force and torque calculation". *IEEE Transactions on Magnetism*, Mag-24(1):443-446, 1988.

- [34] P. L. Timar, A. Fazekas, J. Kiss, A. Miklos, and S. J. Yang. *Noise and Vibration of Electrical Machines*. Elsevier Science Publishers, New York, 1989.
- [35] R. H. Warring. *Sub-miniature Electric motors*. Arco Publishers, Great Britain, London, 1967.
- [36] R. L. White, A. W. Scott, and R. H. Hartley. "Optimum design and performance calculations of highly magnetically saturated d.c. machines for large-scale production". *Proceedings of IEE*, 116(11):1891–1899, 1969.

University of Cape Town

Appendix A

Co-energy exact derivative derivation

The coenergy exact derivative method uses isoparametric elements in order to find a general equation to any particular element shape. The transformation is a one-to-one transformation from a element in the (x, y) plane to a known shape in the (u, v) plane.

The shape functions of the two types of elements used in the finite element simulation, in the (u, v) coordinates system, are:

Table A.1: Shape functions

Linear Triangular	Bilinear Quadratic
$N_1 = 1 - u - v$	$N_1 = (1 + u)(1 + v)/4$
$N_2 = u$	$N_2 = (1 - u)(1 + v)/4$
$N_3 = v$	$N_3 = (1 - u)(1 - v)/4$
	$N_4 = (1 + u)(1 - v)/4$

The shape functions can be used to describe the (x, y) values within the particular element as:

$$\begin{bmatrix} x \\ y \end{bmatrix} = N \begin{bmatrix} x_1 & y_1 \\ x_2 & y_2 \\ \vdots & \vdots \\ x_i & y_i \end{bmatrix} \quad (\text{A.1})$$

where N is the shape function matrix and the x_i and y_i are the coordinates of the i th

node point.

The first derivative of the shape function is used to obtain a one-to-one relationship between (x, y) and (u, v) . The final result is [14]:

$$\begin{bmatrix} \partial N_i / \partial u \\ \partial N_i / \partial v \end{bmatrix} = D \begin{bmatrix} \partial N_i / \partial x \\ \partial N_i / \partial y \end{bmatrix} \quad (\text{A.2})$$

The shape functions are used in determining the Jacobian matrix D which is used in the transformation.

$$D = \begin{bmatrix} \partial x / \partial u & \partial y / \partial u \\ \partial x / \partial v & \partial y / \partial v \end{bmatrix} = \begin{bmatrix} \sum_{i=1}^n N'_{iu} x_i & \sum_{i=1}^n N'_{iu} y_i \\ \sum_{i=1}^n N'_{iv} x_i & \sum_{i=1}^n N'_{iv} y_i \end{bmatrix} \quad (\text{A.3})$$

where

$$N'_{iu} = \frac{\partial N_i}{\partial u} \quad \text{and} \quad N'_{iv} = \frac{\partial N_i}{\partial v} \quad (\text{A.4})$$

The electromagnetic torque from the coenergy method with no forcing current ($J = 0$) in the airgap gives the equation:

$$T = \frac{\partial}{\partial \theta} \int \int_R \int_0^B H dB dR \quad (\text{A.5})$$

The finite element method is discretized into elements and so eqn (A.5) is written for each element separately. Each element is transformed into a isoparametric form using the isoparametric coordinates (u, v) . The integration is accomplished by replacing the differential area dR with $dR = dx dy = |D| du dv$ where $|D|$ is the determinate of the Jacobian matrix D

Equ (A.5) is written using isoparametric element as:

$$T = \frac{\partial}{\partial \theta} \sum_e \int \int_{\square e} \int_0^B H dB |D| du dv \quad (\text{A.6})$$

which can be written as:

$$T = \sum_e \int \int_{\square e} \left[\frac{\partial}{\partial \theta} \left[\int_0^B H dB \right] |D| + \int_0^B H dB \frac{\partial |D|}{\partial \theta} \right] du dv \quad (\text{A.7})$$

where $\square e$ is the area of the element.

Without magnetostriction phenomena in the distorted area, the first derivative becomes

$$\frac{\partial}{\partial \theta} \int_0^B H dB = H^T \frac{\partial B}{\partial \theta} \quad (\text{A.8})$$

and using $B = \nabla A$

$$\begin{bmatrix} B_x \\ B_y \end{bmatrix} = \begin{bmatrix} \partial A / \partial y \\ -\partial A / \partial x \end{bmatrix} \quad (\text{A.9})$$

which with the chain rule used on the differential of the shape functions gives the transformation

$$\begin{bmatrix} \partial A / \partial u \\ \partial A / \partial v \end{bmatrix} = \begin{bmatrix} \partial y / \partial u & -\partial x / \partial u \\ \partial y / \partial v & -\partial x / \partial v \end{bmatrix} \begin{bmatrix} \partial A / \partial y \\ -\partial A / \partial x \end{bmatrix} \quad (\text{A.10})$$

and where

$$G = \begin{bmatrix} \partial y / \partial u & -\partial x / \partial u \\ \partial y / \partial v & -\partial x / \partial v \end{bmatrix} = \begin{bmatrix} \sum_{i=1}^n N'_{iu} y_i & -\sum_{i=1}^n N'_{iu} x_i \\ \sum_{i=1}^n N'_{iv} y_i & -\sum_{i=1}^n N'_{iv} x_i \end{bmatrix} \quad (\text{A.11})$$

Integrating eqn (A.7) and simplifying to the following form:

$$T = \sum_{\square_e} \left[-\frac{1}{\mu_0} \vec{B}^T G^{-1} \frac{\partial G}{\partial \theta} \vec{B} |D| + \frac{|B|^2}{2\mu_0} \frac{\partial |D|}{\partial \theta} \right] w_i \quad (\text{A.12})$$

where w_i is a weighting function for the different element types [8].

Eqn (A.12) is simplified for use with three and four node linear elements. The derivations differ for the two element type due to there differing shape functions.

A.1 Triangular Elements

Using the shape functions shown in Table A.1 the matrix D and G can be simplified for the triangular elements to

$$D = \begin{bmatrix} x_2 - x_1 & y_2 - y_1 \\ x_3 - x_1 & y_3 - y_1 \end{bmatrix} \quad (\text{A.13})$$

$$G = \begin{bmatrix} y_2 - y_1 & x_1 - x_2 \\ y_1 - y_3 & x_3 - x_1 \end{bmatrix} \quad (\text{A.14})$$

Assuming that two of the nodes of the element have a virtual movement, then it would be convenient to analyze the movement of each node separately. This is done by taking partial differentials of

$$\frac{\partial|D|}{\partial\theta} = \frac{\partial|D|}{\partial\theta_1} \frac{\partial\theta_1}{\partial\theta} + \frac{\partial|D|}{\partial\theta_2} \frac{\partial\theta_2}{\partial\theta} \quad (\text{A.15})$$

where the two components of the above equation can be written as:

$$\frac{\partial|D|}{\partial\theta_1} = x_1(x_1 - x_3) + y_1(y_3 - y_2) \quad (\text{A.16})$$

$$\frac{\partial|D|}{\partial\theta_2} = x_2(x_1 - x_3) + y_2(y_1 - y_3) \quad (\text{A.17})$$

where $x = r \cos \theta$ and $y = r \sin \theta$, and $\partial\theta_1 = \partial\theta$ and $\partial\theta_2 = \partial\theta$, which leads to

$$\frac{\partial|D|}{\partial\theta} = x_1(x_3 - x_2) + y_1(y_3 - y_2) + x_2(x_1 - x_3) + y_2(y_1 - y_3) \quad (\text{A.18})$$

which can be seen as the sum of the movement of the two nodes separately. Eqn (A.15) can thus be written to represent the movement of only one node or by changing the subscribes a other node. It should be noted that the order or rotation of node numbers is important in eqn (A.15).

The first part of eqn (A.12) has to be analyzed of individual nodes moving and thus the chain rule is applied to

$$\frac{\partial G}{\partial\theta} = \frac{\partial G}{\partial\theta_1} \frac{\partial\theta_1}{\partial\theta} + \frac{\partial G}{\partial\theta_2} \frac{\partial\theta_2}{\partial\theta} \quad (\text{A.19})$$

where the two components are

$$\frac{\partial G}{\partial\theta_1} = \begin{bmatrix} -x_1 & -y_1 \\ x_1 & y_1 \end{bmatrix} \quad (\text{A.20})$$

$$\frac{\partial G}{\partial\theta_2} = \begin{bmatrix} x_2 & y_2 \\ 0 & 0 \end{bmatrix} \quad (\text{A.21})$$

which means that a single form of this equation for both movable nodes is not possible.

The simplification of the first part of eqn (A.12) for a movement in two nodes is

$$\begin{aligned} & -\frac{1}{\mu_0} \vec{B}^T G^{-1} \frac{\partial G}{\partial\theta} \vec{B} |D| \\ & = \frac{1}{\mu_0} [B_x^2 x_1(x_2 - x_3) + B_y^2 y_1(y_2 - y_3) + B_x B_y (y_1(x_2 - x_3) + x_1(y_2 - y_3))] \end{aligned}$$

$$+ \frac{1}{\mu_0} [B_x^2 x_2 (x_3 - x_1) + B_y^2 y_2 (y_3 - y_1) + B_x B_y (y_2 (x_3 - x_1) + x_2 (y_3 - y_1))] \quad (\text{A.22})$$

which shows that eqn (A.12) can be written for a movement in one node, ignoring any other movement in that element which can be calculated separately. This makes a computer simulation easier to write and the labelling of the elements has to be set in one direction, i.e. clockwise, to avoid the cancelation of the different torque components.

The final equation for triangular elements is then

$$T = \frac{1}{2} \sum_e \sum_i \left[\frac{1}{\mu_0} [B_x^2 x_1 (x_2 - x_3) + B_y^2 y_1 (y_2 - y_3) + B_x B_y (y_1 (x_2 - x_3) + x_1 (y_2 - y_3))] \right. \\ \left. + \frac{|\vec{B}|^2}{2\mu_0} [x_1 (x_3 - x_2) + y_1 (y_3 - y_2)] \right] \quad (\text{A.23})$$

where e is the number of virtually distorted elements and i the number of virtually moved nodes within an element. The movable node is always labelled as node 1 and the other nodes label in a clockwise direction.

A.2 Bilinear Quadratic Elements

A similar derivation can be done for four noded bilinear elements as was just done for triangular elements.

The shape functions shown in Table A.1 are used to simplify the matrix D and G to

$$D = \frac{1}{4} \begin{bmatrix} x_1 - x_2 - x_3 + x_4 & y_1 - y_2 - y_3 + y_4 \\ x_1 + x_2 - x_3 - x_4 & y_1 + y_2 - y_3 - y_4 \end{bmatrix} \quad (\text{A.24})$$

$$G = \frac{1}{4} \begin{bmatrix} y_1 - y_2 - y_3 + y_4 & -(x_1 - x_2 - x_3 + x_4) \\ y_1 + y_2 - y_3 - y_4 & -(x_1 + x_2 - x_3 - x_4) \end{bmatrix} \quad (\text{A.25})$$

Following the same method as in the triangular element analysis, the final result is

$$T = \frac{1}{2} \sum_e \sum_i \left[\frac{1}{\mu_0} [B_x^2 x_1 (x_2 - x_4) + B_y^2 y_1 (y_2 - y_4) + B_x B_y (y_1 (x_2 - x_4) + x_1 (y_2 - y_4))] \right. \\ \left. + \frac{|\vec{B}|^2}{2\mu_0} [x_1 (x_4 - x_2) + y_1 (y_4 - y_2)] \right] \quad (\text{A.26})$$

It should be noted that in eqn (A.26) the movable node is always node 1 and if more than 1 node in a particular element moves there has to be a rotation in the labelling of the nodes.

It should be noted that eqns (A.23, A.26) for the different element types are similar and the same equation can be used for both element types, but with different element labels.

University of Cape Town

Appendix B

Magnetization curves used in simulations

The curves used in the simulations are the same for both of the motors tested. The magnetic flux density versus magnetic field intensity curves for the rotor and stator yoke were taken from standard B-H curves for 0.6 mm laminated steel and solid mild steel respectively. The demagnetization curve is for Barium Ferrite FXD 280.

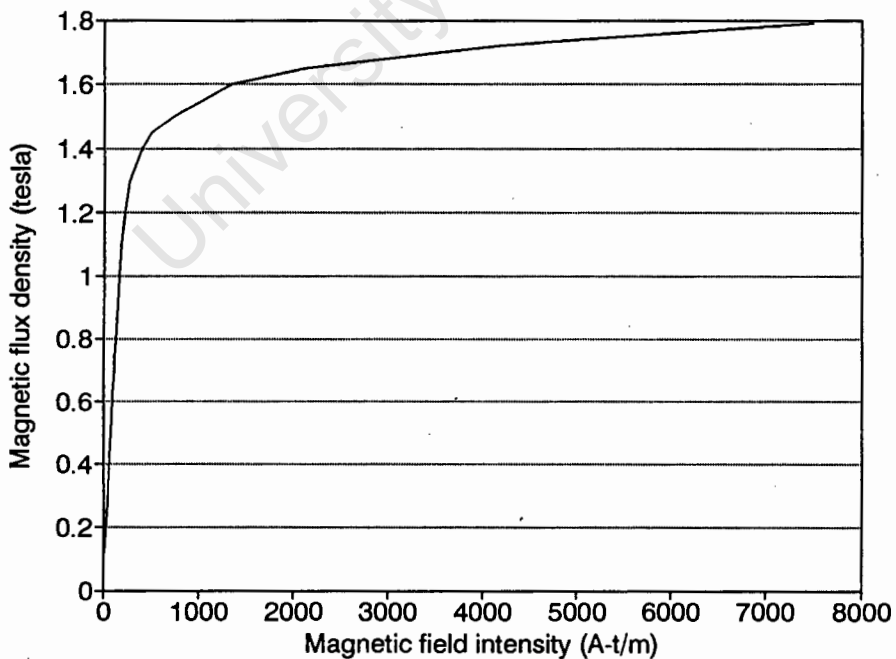


Figure B.1: Flux density versus field intensity curve for the rotor core

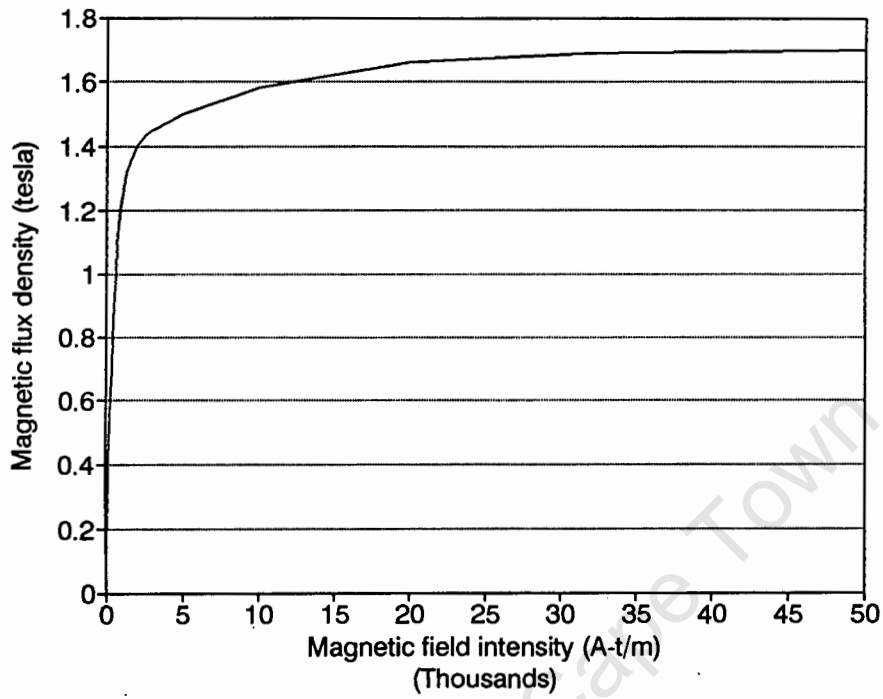


Figure B.2: Flux density versus field intensity curve for the stator yoke

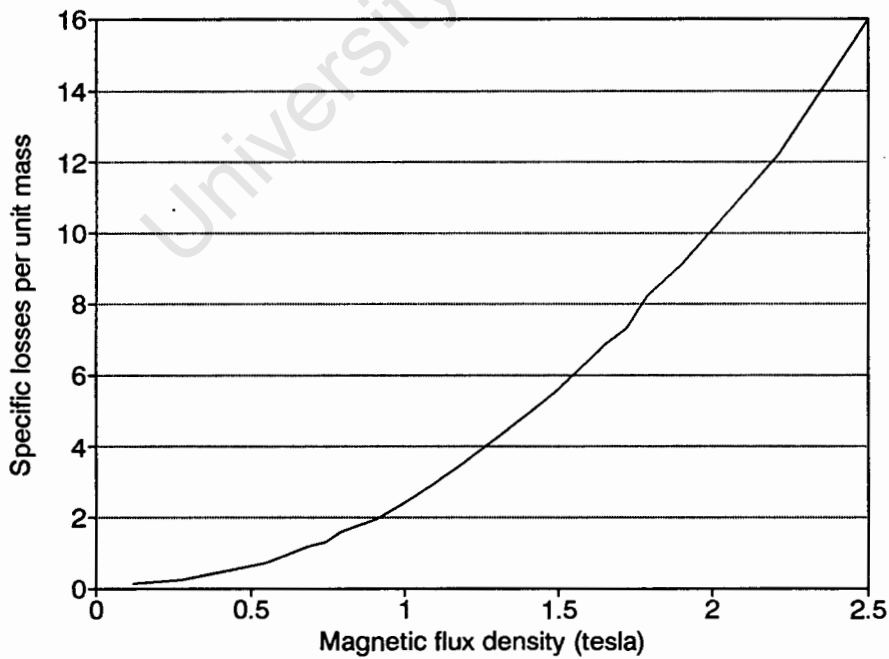


Figure B.3: Specific rotational losses per unit mass W/kg at 50 Hz versus flux density

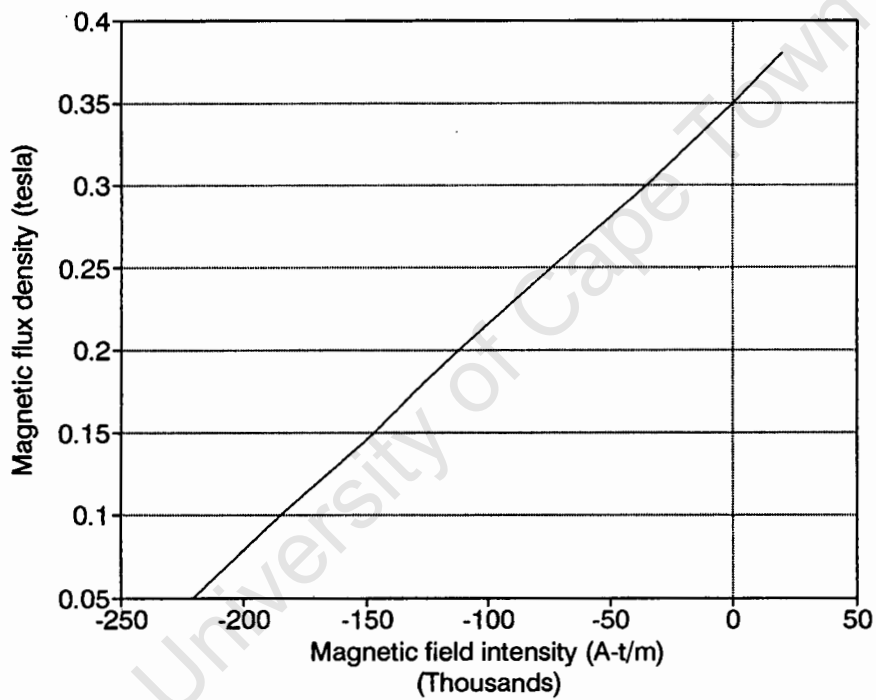


Figure B.4: Demagnetization curve of Barium ferrite used in calculating magnets operating point

Appendix C

Schematic circuit diagram

The current and voltage sensing circuits were built using isolation chips to protect the computer from voltage spikes. The isolation was done using voltage to frequency and frequency to voltage conversion. This was used since the optical isolation chip used only had a linear frequency response and not a voltage response. The isolation was thus done using a frequency signal which was then converted back to a voltage signal before being fed into the computer.

The printed circuit board of the current circuit is shown in Fig C.1 and the schematic diagram of the current circuit is shown in Fig C.2

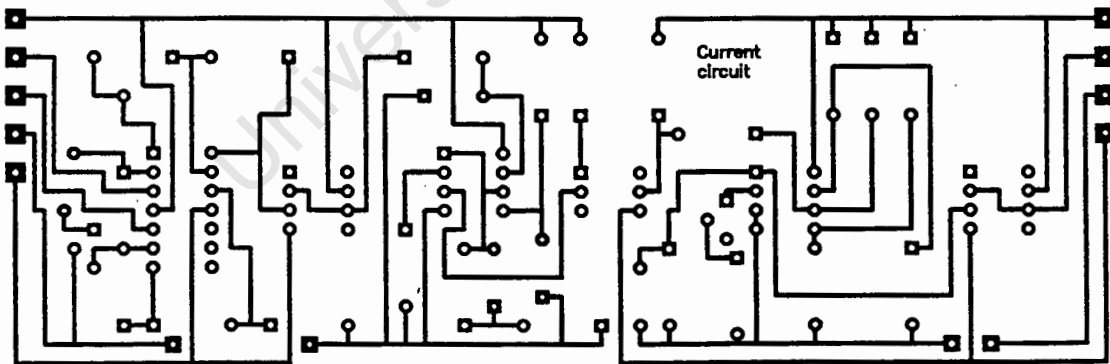


Figure C.1: Printed circuit board of current sensing

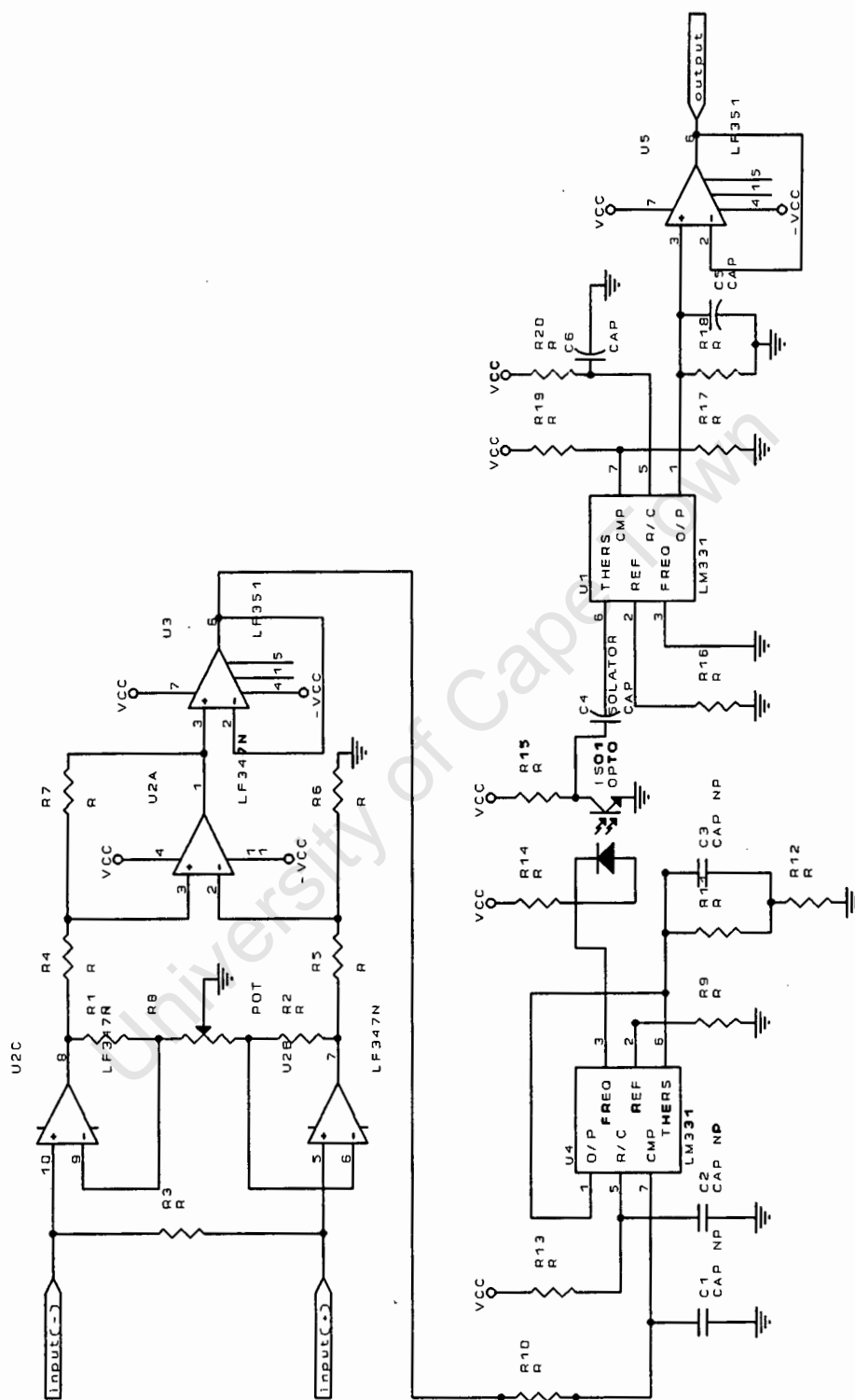


Figure C.2: Schematic circuit diagram of current sensing with protective voltage isolation for the computer

Appendix D

Fast Fourier analysis of torque measurement

The input signal to the computer from the torque transputer is shown in Fig D.1

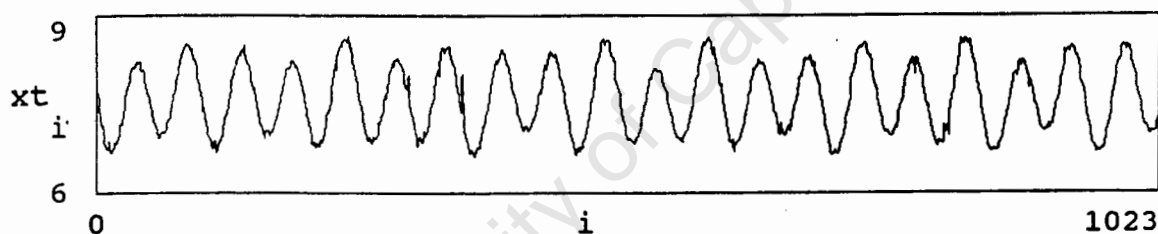


Figure D.1: Unscaled torque signal logged by computer

A fast fourier transform has been done on the torque signal in an attempt to analyze the different frequency spectrums within this signal. Fig D.2 shows the fast fourier transform of the torque signal, excluding the dc component. The main signals seem in Fig D.2 are the first three harmonics, which correspond to imbalances in the mechanical motor system [34]. An imbalanced magnetic attraction may also contribute to these vibrations.

A closer look is needed at the higher frequency vibrations in an attempt to analyze the cogging torque. Fig D.3 shows the fast fourier transform at a frequencies between 244 to 640 Hz which corresponds to the harmonics between the 8th and the 21st. The magnitude of the high frequency vibrations is small and there is no defient vibration harmonic that stands out as being possible from the cogging effect of the motor.

Fig D.4 shows the torque signal after the inverse fourier transformer has been done, but excluding the first three harmonics. The result shows that the mechanical vibrations are dominant in the torque signals.

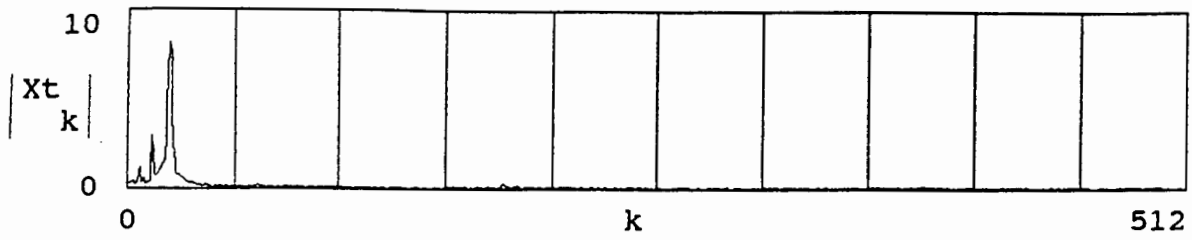


Figure D.2: Fast fourier transform of torque signal

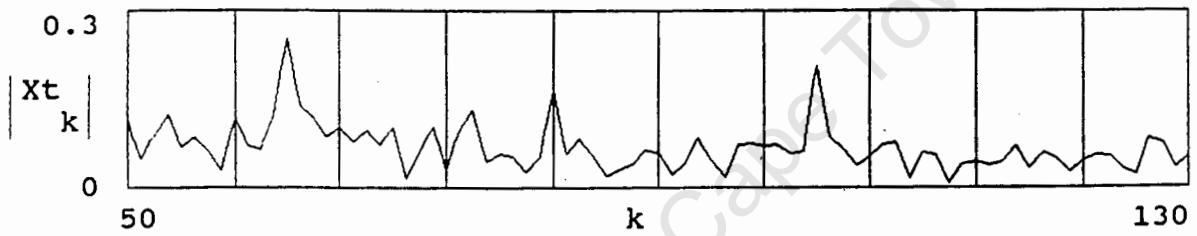


Figure D.3: Fourier analysis of harmonics from the 8th to the 21st

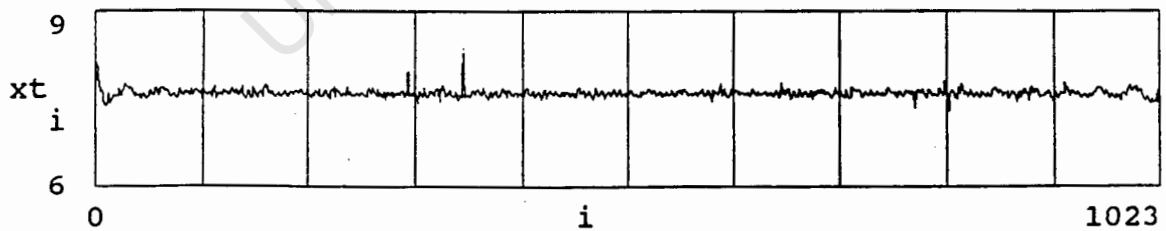


Figure D.4: Smoothed out torque signal with the low frequency vibrations removed

Short Curriculum Vitae

Name Mitchell Wing
Date of birth 15 December 1968
Place of birth Sheffield, England
Education BSc (Hons) Electrical and Electronic Engineering

Experience

Dec. 1987 - Feb. 1988 Kaltron Engineering
Jan. 1989 - Feb. 1989 Lyttelton Engineering Works

Publications

1. "Calculations of Cross MMF of Armature Winding for Permanent Magnet DC motors".
J.F. Gieras, E.E. Moos and M. Wing
SAUPEC-91
Johannesburg, January 1991. pp 273 - 279.
2. "Calculation of the Steady State performance for Small Commutator Permanent Magnet DC motors: Classical and Finite Element approaches"
M. Wing and J.F. Gieras
IEEE Transactions on Magnetics
Being published.
3. "Performance for a Permanent Magnet DC motor using Classical and Finite Element approaches"
M. Wing and J.F. Gieras

Symposium on Power Electronics, Electrical Drives, Advanced Electrical Motors
Positano Italy, 1992. pp 47 - 52.

4. "Influence of Magnetic Circuit Dimensions on the Performance of a DC Commutator motor with Segmental Barium Ferrite Permanent Magnets"
J.F. Gieras, R. Kgoroadira and M. Wing
International Aegean Conference on Electrical Machines and Power Electronics
Kusadasi Turkey, 1992. pp 227 - 230.
5. "Influence of Angular Displacement of a Permanent Magnet on the Performance of a DC Commutator Motor"
M. Wing and J.F. Gieras
XXIX Symposium of Electrical Machines (Asymmetry in Electrical Machines and Transformers)
Wrocław - Szklarska Poręba, 1993, accepted.

University of Cape Town